UNIVERSITÉ DE MONTRÉAL

ALL PHOTONIC BANDGAP

BRAGG FIBER REFRACTOMETERS

HANG QU

DÉPARTEMENT DE GÉNIE PHYSIQUE

ÉCOLE POLYTECHNIQUE DE MONTRÉAL

THÈSE PRÉSENTÉE EN VUE DE L'OBTENTION

DU DIPLÔME DE PHILOSOPHIAE DOCTOR

(GÉNIE PHYSIQUE)

DÉCEMBRE 2013

UNIVERSITÉ DE MONTRÉAL

ÉCOLE POLYTECHNIQUE DE MONTRÉAL

Cette thèse intitulée:

ALL PHOTONIC BANDGAP

BRAGG FIBER REFRACTOMETERS

présentée par : QU Hang

en vue de l'obtention du diplôme de : Philosophiae Doctor

a été dûment acceptée par le jury d'examen constitué de :

M. GODBOUT Nicolas, Ph.D, président

M. SKOROBOGATIY Maksim A., Ph.D, membre et directeur de recherche

M. LEBLOND Frédéric, Ph.D, membre

M. KIRK Andrew G., Ph.D, membre

DEDICATION

I would like to dedicate this thesis to my family and friends,

especially to my mother and father for your unconditional love and support.

ACKNOWLEDGEMENT

I would like to express my heartfelt gratitude to my research supervisor, Prof. Maksim Skorobogatiy, for offering me the opportunity to pursue my scientific dream, for guiding me during my Ph.D study, for encouraging and supporting me when I struggled in the predicaments, and for spurring me when I needed it.

I would like to thank all my friends and colleagues in Engineering Physics, Ecole Polytechnique de Montreal. Especially, I want to thank Bora Ung, Alexandra Dupuis for your assistance of the theoretical simulations involved in my projects. I also thank Anna Mazhorova, Stephan Gorgutsa, Mathieu Roze, Andrey Markov, Frederic Desevedavy, Ning Guo, Niyaz Madhar, Yang Liu and Imran Syed for the valuable discussions, constructive interactions and mutual support during the last four years.

I want to thank the technicians in our group, Francis Boismenu and Yves Leblanc. You two are wonderful colleagues who not only provide plenty of technical assistance, but also offer many useful advices for my daily life.

Finally, I wish to thank my family and friends for their support during my doctoral study.

RÉSUMÉ

Un réfractomètre est un senseur optique permettant de mesurer l'indice de réfraction d'une substance. Depuis que Ernst Abbe a inventé le premier réfractomètre de laboratoire dans les années soixante du dix-neuvième siècle, d'importants efforts ont été faits pour développer de nouveaux types de spectromètres avec une meilleure résolution et une empreinte plus petite. De nos jours, la réfractométrie est une technique fiable largement utilisée dans de nombreux domaines scientifiques et industriels, soit en ce qui a trait aux senseurs biologiques et chimiques, aux tests médicaux, à la gradation des bijoux, à l'industrie pharmaceutique, etc. Récemment, les réfractomètres à base de fibre ont attiré beaucoup l'attention grâce à leurs avantages uniques : leurs faibles pertes, leur légèreté, leur immunité à l'interférence électromagnétique, leur résistance aux environnements hostiles, leur passivité électrique et la possibilité de multiplexage. Aujourd'hui encore, la recherche et le développement de nouveaux réfractomètres à base de fibre ayant de plus hautes résolutions, de plus petites empreintes et un faible coût constituent encore le principal sujet de recherche en réfractométrie.

Dans cette thèse, nous proposerons et fabriquerons expérimentalement un réfractomètre à base de fibre servant à la détection de faibles changements d'indice de réfraction dans des échantillons liquides. La composante principale de ce réfractomètre est une fibre de Bragg creuse, possédant un cœur creux entouré par une alternance de couches de polyméthacrylate de méthyl (PMMA) et de polystyrène (PS) servant de réflecteur de Bragg. Le mécanisme de base de cette fibre est la détection de résonance; les variations d'indice de réfraction de l'échantillon liquide induisent un changement de guidage résonant de la fibre, changeant ainsi l'intensité et la fréquence de résonance de la transmission. Les simulations théoriques et la caractérisation expérimentale sont faites pour confirmer les propriétés de ce mécanisme. De plus, nous étudierons en détail les performances de ce réfractomètre à base de fibre de Bragg en s'attardant à la sensibilité, à la plage dynamique, aux pertes d'insertion/couplage, au temps de réponse et à la dépendance de la sensibilité en fonction de la longueur de la fibre. Nous démontrerons expérimentalement que la sensibilité atteint 1400 nm par unité d'indice de réfraction (RIU), ce qui est comparable à la sensibilité propre aux autres réfractomètres à base de fibre microstructurée, et même aux réfractomètres basés sur la résonance de plasmon de surface. Nous noterons aussi que le temps de réponse du réfractomètre développé dans notre laboratoire est beaucoup plus petit que celui des

réfractomètres à fibres conventionnelles, puisque la taille du cœur creux de la fibre est environ 100 fois plus large que la taille des trous de la fibre. Cette sensibilité est indépendante de la longueur de la fibre, ce qui nous permet de bâtir un système très sensible et compact en utilisant plusieurs centimètres de fibre, ou en employant une bobine de fibre. De plus, ce réfractomètre est avantageux du point de vue de la facilité de fabrication et de la possibilité de production de masse puisqu'il peut être obtenu en utilisant un seul étirage de fibres, sans post-traitement additionnel, comme la gravure chimique ou le polissage mécanique. Les autres avantages de ce réfractomètre consistent en son faible volume d'échantillons liquides, son temps de réponse court (1 seconde pour 40 centimètres de fibre) et la simplicité du mécanisme de détection.

Une autre partie de la thèse portera sur la conception de systèmes tout-fibre où les sous-composantes du réfractomètre seront également basées sur des fibres. Les instruments spectroscopiques jouent un rôle important dans plusieurs des réfractomètres utilisant des méthodes de détection spectrale. Les spectromètres conventionnels emploient des éléments dispersifs délicats tels que des prismes ou des réseaux mobiles, ce qui augmente le coût des dispositifs et demande un temps d'acquisition relativement long. De plus, la résolution de ces spectromètres est proportionnelle à la longueur du chemin optique dans le spectromètre, ce qui les rend difficiles à miniaturiser et à intégrer dans un système compact. Le développement de spectromètres compacts, à faible coût et pouvant être intégrés dans des dispositifs à base de fibres en est donc venu à constituer une direction importante pour le développement d'instruments de spectroscopie de nouvelle génération.

Dans cette thèse, nous démontrerons par surcroit qu'un spectromètre basé sur un ensemble de fibre de Bragg peut être utilisé dans le réfractomètre décrit ci-haut pour remplacer le spectromètre traditionnel à base de réseaux. En tout, 100 fibres de Bragg à cœur plein possédant des bandes interdites complémentaires se chevauchant partiellement ont été choisies comme base du spectromètre. Le système est calibré en utilisant une source monochromatique ajustable. Cette lumière incidente est filtrée par l'ensemble des fibres et est convertie en une image mesurée par une caméra CCD monochrome. Nous développerons ainsi un algorithme de « matrice de transmission » pour associer les images de la caméra au spectre d'essai, avec une calibration préalable. Le spectre est reconstruit à l'aide d'une pseudo-inversion de la matrice de transmission de l'ensemble de fibres à l'aide de la décomposition en valeur singulières (SVD). Lorsque nous utilisons ce système pour mesurer des filtres commerciaux, le centre du spectre d'essai peut

toujours être reconstruit à quelques pourcents de sa vraie valeur, peu importe sa position et sa largeur; même si les bandes interdites des fibres individuelles sont larges (60 nm – 180 nm), le spectromètre a une résolution de 20 – 30 nm, puisqu'une importante quantité de ces fibres sont utilisées pour la détection. Nous analyserons ensuite en quoi le bruit expérimental affecte la qualité de la reconstruction spectrale et proposerons plusieurs méthodes pour minimiser cette influence. Somme toute, ce spectromètre est une implémentation abordable tout-fibre pouvant être naturellement intégré aux transducteurs à fibres. Il est peu dispendieux du fait qu'il est basé sur des fibres de polymère, permet l'opération rapide du système, puisqu'il ne possède pas de parties mobiles, et offre un couplage efficace avec les autres dispositifs à fibres.

Finalement, nous intégrerons les deux dispositifs étudiés, soit le transducteur à base de fibres cœur-plein et le spectromètre à base de fibres à cœurs creux pour obtenir un réfractomètre tout-fibre complet, ayant une haute sensibilité et qui permettra la mesure d'échantillons liquides. Le plus grand impact technologique de ce travail se traduirait par l'implémentation de détecteurs optiques hautement intégrés. Nos recherches sur le sujet semblent nous permettre d'affirmer qu'il s'agirait de la première réalisation concrète d'un senseur tout-fibre modulaire où l'intégralité des éléments est à base de fibres. Nous croyons qu'il pourrait être possible d'assembler un système complet en faisant une épissure des modules fibrés individuels, comme la fibre d'illumination, le réfractomètre à fibres et le spectromètre tout-fibre, et ce, dans un futur proche; l'idée est indubitablement des plus intéressantes pour les entreprises.

ABSTRACT

A refractometer is an optical sensor that can be used to measure the refractive index of a substance. Ever since Ernst Abbe invented the first laboratory refractometer in the late sixties of the nineteenth century, tremendous efforts have been undertaken to develop various types of refractometers with better resolution and smaller footprint. Nowadays, refractometry becomes a reliable technique that is widely used in a variety of scientific and industrial fields such as bio/chemical sensing, food industry, medical/clinical examination, jewelry gradation, pharmaceutical and cosmetic industry, to name a few. In recent years, fiber-based refractometers have drawn considerable attention due to their unique advantages such as low signal loss (attenuation), light weight, immunity to electromagnetic interference, resistance to harsh environments, electrical passivity, and possibility of multiplexing. To date, the R&D (research and development) of novel fiber-based refractometers with advantages of high sensitivity, small footprint and low cost still constitutes the main research topic in refractometric studies.

In this thesis, we firstly propose and experimentally demonstrate a fiber-based refractometer for sensing small changes in the refractive index of liquid analytes. The key component of the refractometer is a hollow-core polymer Bragg fiber, which features a large hollow core surrounded by an alternating polymethyl methacrylate (PMMA)/polystyrene (PS) multilayer as a Bragg reflector. This Bragg fiber refractometer operates on a resonant sensing mechanism, namely, variations in the refractive index of a liquid analyte filling the fiber core modify the resonant guidance of the fiber, thus leading to both intensity changes and spectral shifts in the fiber transmission. Both theoretical simulations and experimental characterizations are carried out to verify this resonant sensing mechanism of the proposed Bragg fiber refractometer. Moreover, we present a comprehensive study of the factors that affect the performance of Bragg fiber refractometers. These factors include sensitivity, dynamic range, insertion/coupling loss, response time and dependence of the refractometer sensitivity on the fiber length. We experimentally demonstrate that sensitivity of the Bragg fiber refractometers is very high, and is ~1400 nm/refractive index unit (RIU) which is comparable to that of the microstructured-fiber-based refractometers and surface-plasmon-resonance-based refractometers. We also note that such a sensitivity is equivalent to a refractometer resolution of $\sim 7 \times 10^{-5}$ RIU, assuming that 0.1 nm spectral shift can be accurately measured (0.1 nm is the typical resolution

of a high-end grating spectrometer). At the same time, filling time (response time) of the refractometers developed in our labs is much shorter than that of the microstructured-fiber-based refractometers, as the size of the Bragg fiber hollow core is ~100 times larger than the size of holes in the microstructured fiber. We also note that the sensitivity of a Bragg fiber refractometer is virtually independent on the length of the Bragg fiber; therefore, a sensitive and highly compact system can be realized using a several-centimeter-long fiber section or a fiber coil. Moreover, this Bragg fiber refractometer is also advantageous due to the ease of fabrication and the possibility of mass production, since the Bragg fibers used in refractometers can be obtained using a single-step fiber-drawing process, where additional post-processing modifications, such as chemical etching or mechanical polishing, are not required. Other advantages of the Bragg fiber refractometers include small volume of liquid analyte, low cost, short response time (~1 s for the 40 cm long Bragg fiber), and simplicity of the sensing mechanism.

Another aspect of this thesis deals with design of the all-fiber systems where all the subcomponents of the refractometer system are fiber-based. In particular, spectroscopic instruments play a key role in many fiber-based refractometer systems operating using a spectral-based detection modality. Conventional spectrometers employ delicate dispersive elements such as movable gratings or prisms, which increase the cost of the devices and require relatively long time for spectral acquisition. Besides, resolution of these spectrometers is normally proportional to the optical path length inside a spectrometer, which makes such devices difficult to miniaturize or to integrate into a portable system. Thus, development of the compact, low-cost spectrometer modules that can be easily integrated with fiber-based transduction modules constitutes an active area of optical sensor research.

In this thesis we demonstrate a Bragg fiber bundle spectrometer that can be naturally integrated with the hollow-core Bragg fiber refractometer, thus resulting in an all-fiber sensor system that does not use a traditional grating-based spectrometer. Particularly, we use ~100 of solid-core Bragg fibers with complementary and partially overlapping bandgaps to fabricate a spectrometric fiber bundle. We then train the system using a tunable narrowband reference source (monochromator-based source). In this calibration measurement, the incident light from the reference source is filtered by the individual fibers in the bundle, and the image of the output facet of a fiber bundle is recorded using a monochrome CCD camera. As a result, a transmission matrix of the spectrometer system is constructed. This transmission matrix is then used together

with a Singular Value Decomposition algorithm in order to reconstruct the spectra of the unknown sources by interpreting the CCD images of the fiber bundle output facet. When applying this methodology to the relatively narrow test spectra (produced by various commercial filters), we find that the center peak of a test spectrum can always be reconstructed within several percents of its true value regardless of its position and width. We also find that although the widths of the individual Bragg fiber bandgaps are quite large (60-180 nm), the Bragg fiber bundle spectrometer has a resolution of 20-30 nm, as a large number of such fibers with partially overlapping bandgaps are used in a spectrometric bundle. Also, effect of the experimental noise on the quality of spectral reconstruction is analyzed, and several approaches are proposed in order to minimize the influence of noise. Overall, we conclude that the demonstrated Bragg fiber bundle spectrometer represents an economic all-fiber implementation of the spectrometer device that can be naturally integrated with other fiber-based transducers. The all-fiber spectrometer is cheap as it is based on plastic fiber technology, allows fast operation because of the lack of moving parts, and it can allow efficient and simple butt-coupling with other fiber-based devices.

Finally, we integrate the hollow-core Bragg fiber transducer with the solid-core Bragg fiber based spectroscopic fiber bundle, and demonstrate a complete and highly sensitive all-fiber refractometer for operation of liquid analytes. We believe that the main impact of our work is in the area of instrumentation of highly integrated optical fiber-based sensors. Thus, for the first time, to our knowledge, we have demonstrated a modular, all-fiber sensor architecture where all the elements of a complete sensor system are based on optical fibers. We envision that in the near future, one would be able to assemble a complete all-fiber sensor system by simply splicing various off-the-shelf on-demand fiber modules such as the light delivery fiber, the fiber refractometer, and the fiber-based spectrometer, which is a very intriguing proposition.

TABLE OF CONTENTS

LIST OF TABLES

LIST OF FIGURES

LIST OF APPENDICES

LIST OF SYMBOLS AND ABBREVIATIONS

α	Absorption loss coefficient
β	Mode propagation constant
c	Speed of light in vacuum
d_h	Thickness of the high-index layer in a Bragg reflector
d_l	Thickness of the low-index layer in a Bragg reflector
ε	Dielectric constant
λ	Wavelength of light
L	Fiber length
n	Refractive index of a material
$n_{analyte}$	Refractive index of an analyte
n_c	Refractive index of the core of the Bragg fiber
n_l	Refractive index of the high-index layer in the Bragg reflector
n_h	Refractive index of the low-index layer in the Bragg reflector
n_{eff}	effective refractive index of a guided mode
P	Power of light
P_{in}	Power coupled into a fiber
P_{out}	Fiber output power
S	Sensitivity of sensor
v	Frequency of light
ω	Angular frequency of light
CCD	Charge coupled device
C-T	Czerny-Turner
FFT	Fast Fourier transform

FWHM	Full width at half maximum
F-P	Fabry-Perot
FBG	Fiber Bragg grating
LCORRS	Liquid-core optical ring resonator sensor
LPG	Long period grating
MOF	Microstructured optical fiber
PCF	Photonic crystal fiber
PBG	Photonic bandgap
PMMA	Polymethyl methacrylate
PS	Polystyrene
RIU	Refractive index unit
R&D	Research and development
SEM	Scanning electron microscope
SPR	Surface plasmon resonance
SPW	Surface plasmonic wave
SVD	Singular value decomposition
TIR	Total internal reflection
TMM	Transfer matrix method
WGM	Whispering gallery mode

INTRODUCTION

A refractometer is an optical sensor used for measuring changes in the refractive index of an analyte. As illustrated in Fig.1.1, after an analyte is added to a refractometer, the optical signal coming out of the refractometer is monitored over time. Changes in the analyte refractive index are typically inferred from changes in the refractometer optical transmission, which is interrogated by various optical detectors such as photodiodes or spectral analyzers.
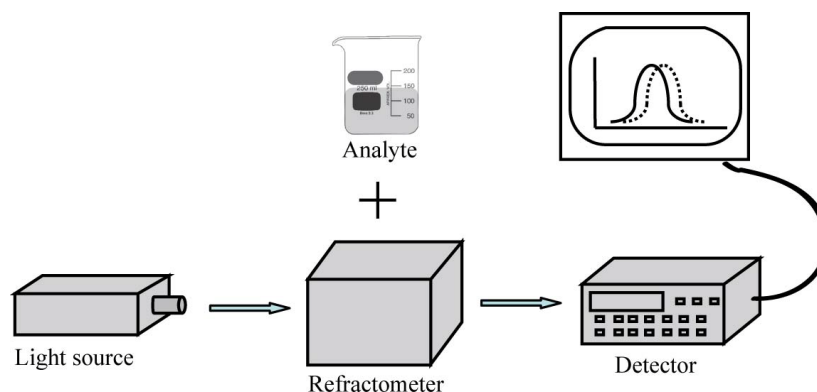
Figure 1.1   Schematic of the operating principle of a refractometer.

The history of refractometers can be traced back to the nineteenth century, when Ernst Abbe developed the first laboratory refractometer that was commercialized by Carl Zeiss AG several years later [1]. Ever since then, refractometry has gradually become the main technique used in the chemical analysis to determine concentrations of solutions, and as a valuable tool in the identification of unknown substances. During the last 100 years, a tremendous effort has been made to develop various types of refractometers with better resolutions and smaller footprints. The techniques and materials involved in the prior research include critical angle method, deflection method, Surface plasmon resonance (SPR) method, optical interferometry (e.g. Michelson interferometric refractometers), fiber optics, and photonic crystals. These techniques along with their advantages and limitations are briefly reviewed in Chapter 1. Nowadays, refractometry is a well-accepted technique that is widely used in many scientific and industrial applications such as bio- and chemical sensing, food production, medical examination, jewelry gradation, pharmaceutical and cosmetic analysis [2], to name a few.

Among all the refractometric devices, fiber-optic refractometers have received a considerable attention due to their unique advantages such as low signal attenuation, light weight,

immunity to electromagnetic interference, resistance to harsh environments (e.g. for the mining and aerospace industries), electrical passivity, and possibility of multiplexing [2, 3]. In general, fiber-based refractometers can be categorized into two classes according to the different detection strategies, namely, amplitude-based detection strategy and spectral-based detection strategy [4]. Each class has its own advantages and limitations. In the amplitude-based detection strategy, one operates at a fixed wavelength and records changes in the amplitude of a signal, which are then re-interpreted in terms of changes in the analyte refractive index. Among the principal advantages of the refractometers operating on this strategy are low cost, ease of fabrication, and simple signal acquisition and processing, since no spectral manipulations are required. The commercial Fiber-optic Endface Refractometer from FORC-PHOTONICS [5] is a typical example of the fiber refractometer using the amplitude-based detection strategy. Unfortunately, the resolution of such refractometers is typically limited to a modest $10^{-3} - 10^{-4}$ refractive index unit (RIU). Generally speaking, such a resolution could meet the requirements for regular scientific and industrial applications such as detection of sugar concentrations in food or beverage. However, a higher resolution of $10^{-5} - 10^{-7}$ RIU may be required for some demanding bio-sensing applications, e.g., detection of the quantity of bacteria in bio-solutions or detection of bio-binding events. Besides, we note that most of the amplitude-based fiber refractometers operate using interaction of the analyte with the evanescent field of the fiber core modes. Thus, in order to increase the sensitivity, certain fiber modifications have to be carried out to ensure an efficient overlap between the analyte and the evanescent field of the fiber core modes. These modifications may include stripping off the fiber cladding by chemical etching or mechanical polishing [6-8], tapering fibers into microfibers [9-11], or functionalizing fibers with high-index films [12]. In practice, these laborious modifications of the fiber structure not only weaken the mechanical strength of the fiber sensor, but also limit its effective sensing length.

An alternative detection strategy is spectral-based. This sensing modality is particularly effective in the resonant sensing configuration that features sharp transmission or absorption peaks in the fiber transmission or reflection spectra. Perturbations of the refractive index of an analyte placed in the spatial proximity of a certain resonant structure (e.g. fiber Bragg gratings [13-15], or fiber in-line interferometers [16-21], etc.) would modify the structure resonant properties, thus leading to spectral shifts of the resonant peaks in the fiber spectra. There are several advantages offered by the spectral-detection based fiber refractometers. Firstly, resonant

lines that are used to monitor changes in the analyte refractive index can be made very narrow via proper design of the sensor resonator structure, thus resulting in a very high sensor resolution. Secondly, resonant sensors can be analyte specific when operating in the vicinity of the characteristic absorption lines of the analyte. Lastly, such sensors are, generally, less influenced by fluctuations in the intensity of the light sources used for optical interrogation, thus improving the accuracy of refractive index measurements. The resolution of spectral-detection based refractometers can be as small as 10^{-4}-10^{-7} RIU. On the negative side, the fabrication of the in-fiber resonant structures is typically a demanding and time-consuming task that can require significant investments in fiber-processing equipments. The cost of fabrication and complexity of the fabrication process are the two major barriers for mass-production of resonant fiber sensors. In this respect, the Microstructured Optical Fibers (MOFs) and photonic bandgap fibers (a subset of MOFs) may constitute a feasible solution for the development of the spectral detection-based fiber refractometers.

Compared to regular step-index fibers, MOFs offer several major advantages [4]: (1) a MOF always comprises some kind of a micro-sized resonant structure that runs along the entire length of the fiber, so that additional fiber processing (e.g. inscription of fiber gratings) is generally not required; (2) MOFs by their nature can accommodate liquid or gaseous analytes within their hollow microstructure; (3) hollow-core MOFs could achieve an almost-complete modal overlap with test analytes, thus leading to a high sensitivity for refractive index measurements. These attractive advantages potentially make MOFs promising for the development of the new generation of fiber refractometers. The main disadvantage of the MOF-based refractometers is that the infiltration of test analytes into the MOF microstructure takes a relatively long time (e.g., ~10 mins for a 20 cm long fiber as reported in [22, 23]) due to the small diameter of the micro-sized channels. Therefore, shortening of the MOF-based refractometer response time constitutes one of the major research directions for this type of sensor.

Finally, we note that spectroscopic devices play a key role in spectral-detection based refractometers. Traditional spectrometers normally employ moving dispersive elements such as high quality Bragg gratings, which leads to high system costs and slow acquisition speeds. Moreover, the resolution of such spectrometers is limited by the length of the spectrometer optical path, which, in turn, makes traditional spectrometers difficult to miniaturize without the loss of resolution. The Majority of fiber-optical sensors that use spectroscopic devices for

detection are limited to laboratory applications due to high costs and the relatively large size of such systems. Therefore, one of the essential driving forces behind the R&D of spectroscopic instruments is the development of the compact, rapid and cost-effective spectrometers that can be conveniently integrated into fiber-optic sensing devices. In this respect, we believe that the fiber-based spectrometers detailed in this thesis may constitute a feasible solution. Existing spectrometers mainly use optical fibers to transfer optical signals from the optical probe to the dispersive element (e.g. gratings) [24, 25]. However, some special fibers (for instance, photonic bandgap fibers or fibers with gratings) can provide the dispersive function, which potentially makes such fibers capable of realizing the function of a spectrometer [26-28]. It was demonstrated recently that the function of a spectrometer can even be implemented within a regular multimode fiber by interrogating the speckle patterns in the fiber output image [29]. These realizations have inspired us to look for an all-fiber spectrometer that can be easily integrated with fiber-based transducers and that can offer fast acquisition speeds, small footprint and high resolution.

The objective of this thesis is to propose and experimentally demonstrate a compact, rapid, highly sensitive, all-fiber refractometric system operating on the spectral-based detection strategy. Particularly, the work in this thesis can be sub-divided into three parts:

1). We propose and experimentally demonstrate a novel, highly sensitive liquid-core Bragg fiber refractometer for the detection of small changes in the refractive index of liquid analytes. This refractometer uses a single piece of the hollow-core photonic bandgap Bragg fiber to host and probe liquid analytes. The fiber is drawn using a simple single-step fiber drawing process, which is beneficial for mass production of the cost-effective fiber transducers. Spectral shifts in the fiber transmission spectrum induced by the variations in the refractive index of a liquid analyte filling the fiber core are detected and interpreted using a combination of experimental and simulation techniques. Compared to other MOF-based refractometers, the response time of the hollow-core Bragg fiber refractometer is significantly reduced due to the large fiber core size.

2). We propose and experimentally demonstrate a fiber-based spectrometer that consists of a solid-core Bragg fiber bundle and a monochromatic CCD camera. This fiber spectrometer potentially can be used to replace traditional spectrometers based on moving gratings,

thus leading to a significant cost saving, increased sensing speed, and a simple all-fiber design.

3).   Finally, we integrate the hollow-core Bragg fiber transducer together with the fiber bundle-based spectrometer and demonstrate a complete all-fiber refractometric system for operation with liquid analytes.

The rest of this thesis is organized as follows: in Chapter 1.1 we provide an up-to-date review of the scientific literature that describes various types of refractometers. The advantages and limitations of each technique are briefly introduced. In Chapter 1.2 we review the common spectrometer types which are routinely used in optical sensing. In particular, we focus on the fiber-based spectrometers that are very promising in the design of miniaturized and highly integrated all-fiber sensor systems. Chapter 2 introduces two popular sensing modalities used by fiber optic refractometers, which are the amplitude-based detection modality and the spectral-based detection modality. We note that due to the resonant guiding properties of the Bragg fiber, the spectral-based detection modality is more suitable for fiber refractometers based on photonic bandgap Bragg fibers. In Chapter 3, we propose and experimentally demonstrate a hollow-core Bragg fiber-based refractometer for sensing small changes in the refractive index of a liquid analyte filling the fiber core. We detail the resonant sensing modality of the refractometer, and then carry out both theoretical simulations and experiments to explain the sensor performance. Furthermore, we conduct a thorough analysis of the factors that affect the performance of the Bragg fiber refractometer (e.g. sensitivity, detection limit, response time, etc). In Chapter 4, we propose and experimentally demonstrate a photonic bandgap fiber bundle spectrometer that consists of ~100 solid-core Bragg fibers and a monochrome CCD camera. The operating principle of the proposed Bragg fiber bundle spectrometer is based on the "transmission matrix algorithm" which allows reconstruction of the unknown spectrum from the image of the transmitted intensities of the individual Bragg fibers in the fiber bundle. Here, we also present a detailed study of the resolution of the fiber bundle spectrometer and propose several methods to improve its resolution. Chapter 5 demonstrates a complete all-fiber spectroscopic system that integrates the hollow-core Bragg fiber refractometer and the Bragg fiber bundle spectrometer. We conduct an extensive optical characterization of the system, and demonstrate that the sensitivity of the all-fiber system is identical to the sensitivity of a system that uses a traditional grating-based spectrometer. Finally, in Chapter 6, we summarize the distinctive features of the fiber

sensors and all-fiber sensing systems demonstrated in this thesis, discuss their potential applications, and suggest future research directions that would improve the performance of these sensing devices.

CHAPTER 1   LITERATURE REVIEW

In Chapter 1, we first review previous work related to the development of the various refractometer types. Both non-fiber-based (Section 1.1) and fiber-based (Section 1.2) refractometers are reviewed with their advantages and limitations briefly summarized. We then focus in particular on the Microstructured Optical Fiber (MOF) -based refractometers (Section 1.3). We conclude that when compared to the conventional step-index fibers, MOFs offer many advantages for sensing of the refractive index of liquid or gaseous analytes. In Section 1.4, we review several types of spectrometers currently used in the optical sensor systems. These spectrometers include grating spectrometers, prism spectrometers, Fourier transform spectrometers as well as fiber-based spectrometers. We note that fiber-based spectrometers potentially can be fabricated into the simple, compact spectroscopic modules that could be conveniently integrated with fiber optic transducers to realize all-fiber sensor devices.

1.1   Review of non-fiber-based refractometers

1.1.1 Refractometers based on critical angle method

In 1869, Ernst Abbe proposed the first refractometer based on the critical angle effect [1]. His original design was so successful that even today it is still used in many devices [30-32]. In the Abbe refractometer shown in Fig.1.2, an analyte is sandwiched between two prisms – a measuring prism and an illuminating prism. Light enters the analyte from the illuminating prism. The top surface of the illuminating prism is ground, so that the light enters the analyte at all possible angles including those almost parallel to the measuring prism surface. The refractive index of the measuring prism is generally higher than those of test analytes. Thus, the incident light with a grazing angle to the measuring prism would be diffracted at the critical angle at the bottom surface of the measuring prism. Then a telescope is used to measure the position of the bright/dark boundary defined by the critical angle effect. According to Snell's law, if the refractive index of the measuring prism is known, the critical angle and thus the bright/dark boundary position is simply determined by the refractive index of the liquid analyte. Therefore, knowing the boundary position and the refractive index of the measuring prism, one is able to calculate the refractive index of the sample. To prevent chromatic dispersion, two compensating Amici prisms are added inside the telescopic system; otherwise one would see in the eyepiece the

blurred red and blue boundaries rather than the well-defined sharp edges. In the later versions of Abbe refractometers, a temperature-stabilizing system is included in order to minimize errors caused by surrounding thermal fluctuations. In 1997, J. Rheims *et al.* proposed a method to expand the application of Abbe refractometers into the ultraviolet (UV) and infrared (IR) spectral ranges [30]. Note that the accuracy of an Abbe refractometer is affected by the optical absorption of the samples as well as the contact quality between the sample and the prisms. The resolution of the modern Abbe refractometers can achieve 1×10^{-4} RIU [32]. Various handheld refractometers and immersion refractometers [33, 34] can be considered as variants of the original Abbe refractometer design.
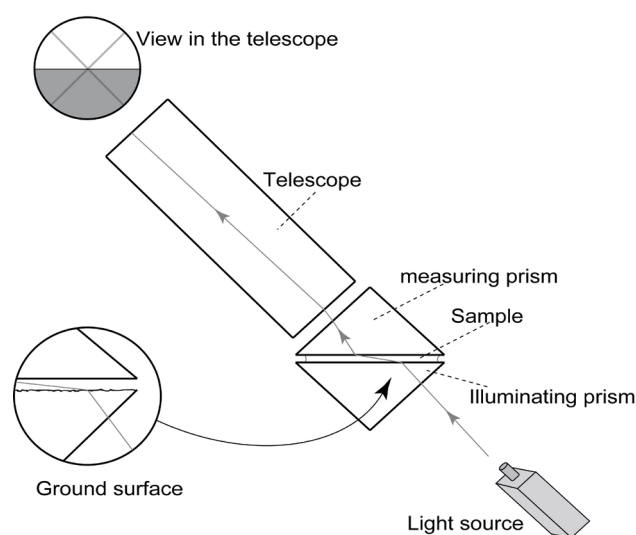
Figure 1.2   Schematic of an Abbe refractometer [34]

Another notable refractometer design based on the critical angle method is the Pulfrich refractometer proposed by Carl Pulfrich in 1888 [35]. As shown in Fig.1.3, a glass prism of high refractive index has two polished plane facets, which are perpendicular to one another. The sample is placed on the horizontal surface of the prism, and in the case of liquid analytes, the sample is contained in a glass cell glued to the prism. A beam of monochromatic light is directed almost horizontally through the substance so that it is incident onto the prism face at the grazing incidence angles. Due to the critical angle effect, the emergent beam will define, on the vertical surface of the prism, a sharp boundary that is observed with a telescope. Refractive index of an analyte can be calculated, if one knows the refractive index of the prism and the position of the boundary. Compared to the Abbe refractometers, Pulfrich refractometers can provide a superior

view of the boundary due to the grazing illumination, thus allowing a more precise reading of the refractive index. A resolution of 4×10^{-4} RIU was reported from the original design [35, 36]. E. Moreels *et al.* [37] used monochromatic laser to replace traditional light sources for illumination, which improved the resolution to 3×10^{-4} RIU. Currently, commercial Pulfrich refractometers with a resolution of 1×10^{-4} RIU are used in many applications [38]. Note that both the Abbe refractometers and Pulfrich refractometers are bulky due to the use of telescopic and temperature-stabilizing systems. Moreover, the resolution of these traditional refractometers is relatively low when compared to that of the more advanced devices introduced in the following sections.
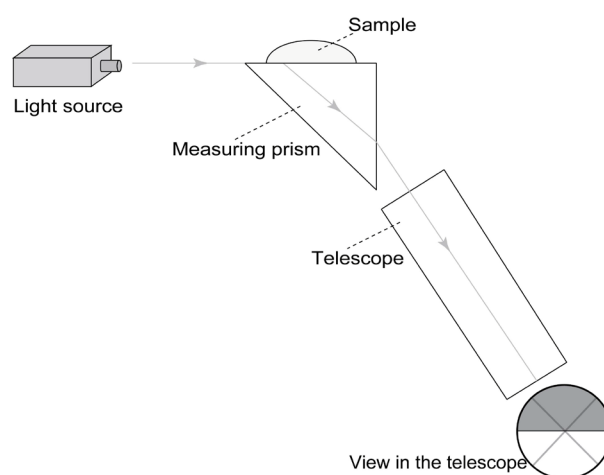
Figure 1.3   Schematic of a Pulfrich refractometer [34]

1.1.2 Refractometers based on deflection method

The deflection effect of light can also be used to implement a refractometer. The most famous design based on this method is the V-block refractometer (also called Hilger-Chance refractometer) that was proposed by J. V. Hughes in 1941 [39]. Fig.1.4 demonstrates the operating principle of a V-block refractometer. The light from an illuminant passes through a collimating slit, enters the liquid analyte in the V-block and gets refracted twice at the perpendicular cell walls. Finally, the position of the emergent light is interrogated by a telescopic system. The deflection angle of the light exiting the block is a function of the refractive index of the liquid analyte and the refractive index of the glass cell. In 1984, E. Moreels *et al.* [37] used a He-Ne laser in the V-block refractometer in order to reduce divergence of the beam passing through the system, and the experimental results suggested a detection error of ± 0.3% to the true

values. Besides, P. R. Cooper [40, 41] extended the application of a V-block refractometer to the near-infrared spectral range using a goniometer that adopted an infrared vidicon camera as the detector, and a resolution of ~2×10^{-4} RIU was obtained from the measurements of paraffin (liquid) and a silicon elastomer (solid). Nikolov *et al.* [42] used an experimental setup similar to that in Ref. [40] to measure refractive indices of the optical plastics (such as polymethyl methacrylate, polystyrene, etc), and obtained a resolution of 1×10^{-4} RIU. Deflection-method-based refractometers can also be implemented by simply using a hollow prism or a hollow cube cell as the sample holder [43, 44]. The principal advantage of the deflection-method-based refractometers is the simplicity of their sensor structure and sensing mechanism; however, the resolution of such refractometers is always limited by the length of the optical path inside of the sample holder. Moreover, due to the geometry of the V-shaped sample holder, this refractometer is most suitable for operation with liquid analytes [43].
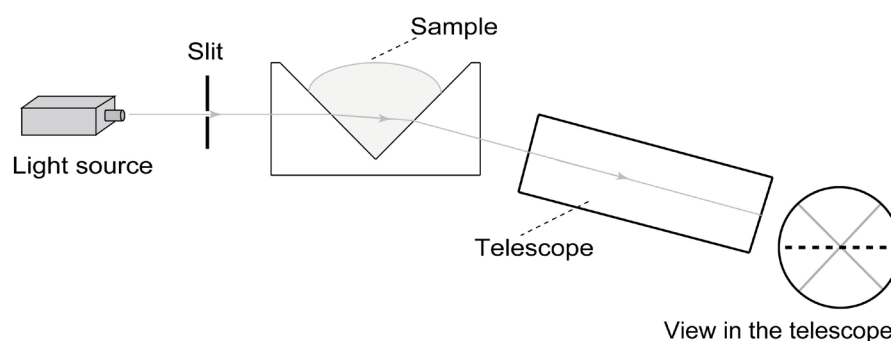
Figure 1.4   Schematic of a V-block refractometer [34]

1.1.3 Interferometric refractometers

Compared to the refractometers based on the critical angle method or deflection method, interferometric refractometers feature much higher sensitivities to changes in the analyte refractive index. In the past, many types of interferometers have been applied to the problem of measuring refractive index, including Michelson interferometers [45-54], Fabry-Perot (F-P) etalons [55-59], Mach-Zehnder (M-Z) interferometers [60, 61], etc. In this thesis, the Michelson interferometer, due to its popularity, is chosen as a typical example in order to demonstrate the general operating principles behind the interferometric refractometers.

The sensing mechanism of a Michelson interferometric refractometer is that the introduction of a test analyte into one arm of a Michelson interferometer would bring an additional phase difference between the two arms of the interferometer, thus leading to variations in the interference fringes. For instance, Kachiraju *et al.* [47] have demonstrated a modified Michelson interferometric refractometer, in which a liquid cell with variable length is inserted into one arm of the interferometric setup. When the optical path length of the liquid cell changes, the phase difference between the two arms is modified, thus leading to shifts of the interference fringes in the output of this Michelson interferometer. As the mechanical length of the liquid cell can be precisely controlled by a micro-positioning stage, the number of the shifted interference fringes is simply determined by the refractive index of a liquid analyte filling the liquid cell. Correspondingly, the refractive index of the test analyte can be calculated by counting the number of shifted fringes during a scan of the length of the liquid cell over a constant distance. An experimental resolution of 2×10^{-4} RIU was measured. Note that in this configuration the detection limit of the refractometer depends on the accuracy that one can achieve to control the length of the liquid cell. This creates a technical barrier to high-resolution sensing of refractive indices.
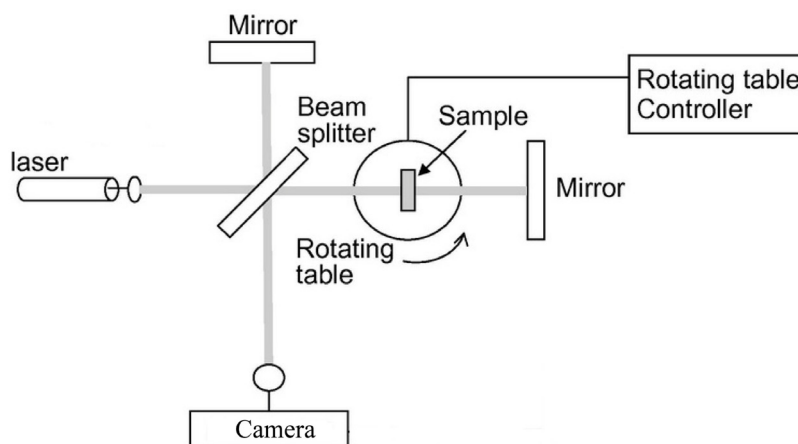
Figure 1. 5   Schematic of the Michelson interferometer-based refractometer (Fig.1 from Ref. [54]).

A method to circumvent this problem was theoretically proposed by C. A. Proctor [53]. As shown in Fig.1.5, a transparent solid sample in the form of a plate with parallel facets is rotated in one arm of the Michelson interferometer, which creates continuous changes in the

optical-path-length difference of the two arms and thus changes in the interference-fringe patterns. Variations in the fringe pattern are recorded by a CCD camera during a 2π rotation of the analyte. The thickness and the refractive index of the analyte can then be calculated independently using a numerical polynomial-fitting method [49, 52, 54]. In the 1960s, this method was experimentally implemented by M. S. Shumate [49] who demonstrated an experimental accuracy of 2×10^{-4} RIU for the measurement of a 0.5 mm thick barium-titanate sample. More recently, this method has been used to measure refractive indices of various solid and liquid analytes [52, 54], and the resolution was improved to $\sim10^{-5}$ RIU [52]. Based on this method, detection accuracy of Michelson interferometers is no longer limited by the accuracy of measurements of the sample thickness; however, we note the resolution of Michelson interferometric refractometers are still susceptible to the air flow in the experimental environment and mechanical vibrations of the components in the experimental setup. Note that this sample-rotation method is also applicable to refractometers based on F-P interferometers and M-Z interferometers as shown in Ref. [55, 57].

1.1.4 Surface plasmon resonance-based refractometers

In the last twenty years, refractometers based on surface plasmon resonance (SPR) have been widely studied due to their dramatically high sensitivities [62]. It is well known that the collective oscillation of the free-charge carriers at a metal/dielectric interface yields a surface plasmon wave (SPW) propagating along the interface. The excitation of the SPW is extremely sensitive to changes in the refractive index of the dielectric adjacent to the metallic layer, which is the sensing mechanism for the operation of SPR refractometers. A typical example of a SPR refractometer using the Kretschmann-Reather (K-R) configuration is presented in Fig.1.6.
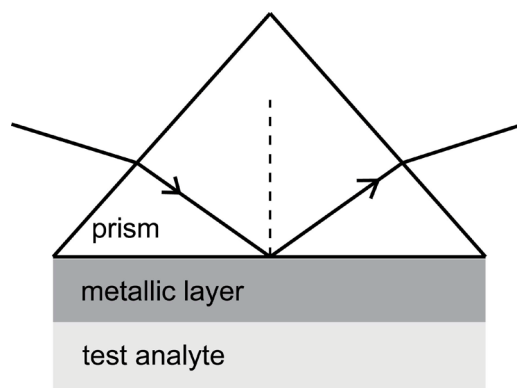
Figure 1.6   Schematic of a SPR refractometer using the Kretschmann-Reather configuration

In the K-R configuration, a p-polarized beam passes through a glass prism and then gets reflected on the bottom facet of the prism coated with a thin metallic layer (e.g. Au or Ag layer). The presence of a prism allows phase matching of an incident light wave with a plasmonic wave at the metal/dielectric interface by properly choosing the light wavelength and the incident angle. Mathematically, the phase matching condition can be expressed as the equality between the plasmon wave-vector and the projection of the wave-vector of the incident light along the prism interface. Changes in the refractive index of an analyte adjacent to the metallic layer would modify the phase-matching condition, thus leading to variations in the amplitude and spectrum of the reflected beam, which constitutes the sensing principle of a SPR refractometer. The SPR setup can also be used as a bio-sensor to interrogate bio-layer binding events, since the resonant condition is highly sensitive to changes in the refractive index of the medium within 100-300 nm range of the interface [63]. Typical resolution of a SPR sensor is on the order of 10^{-5}-10^{-7} RIU [64, 65]. Despite the outstanding sensitivity, SPR sensors are mostly used in laboratory environments due to the complexity of the interrogation system and relatively high cost of the SPR components required.

1.1.5 Photonic crystal refractometers

In the last decade, the study of photonic crystal sensors for bio- and chemical sensing has received considerable attention due to the development of many advanced micro- and nano-photonic fabrication techniques. Photonic crystals generally refer to structures in which the dielectric constant has a periodic variation in one, two or in all three orthogonal directions [66]. In such structures one observes formation of the so-called spectral photonic bandgaps (PBGs), which are the spectral regions where photons are unable to propagate in the bulk of the periodic structure. Many photonic crystals contain porous networks of voids permeable to gaseous or liquid analytes. Infiltration of photonic crystal voids with analytes would change the refractive index of these voids, thus modifying the PBG spectral signatures (e. g. resonant dips) in the photonic crystal transmission (or reflection) spectra. This is the principal transduction mechanism for photonic crystal sensors. The sensitivity of photonic crystal refractometers is generally defined as resonant-wavelength shift per refractive index unit. In order to increase the sensitivity, resonant structures such as microcavities [67-70], air slots [71-73], etc., can be introduced into a photonic crystal. In Ref. [67], a 2-D photonic crystal with a microcavity was demonstrated for

sensing of changes in the refractive index of liquid analytes, and the experimental results showed a sensitivity of 63 nm/RIU. C. Kang *et al*. [68] improved the sensitivity to ~100 nm/RIU by adding, to the microcavity, multiple holes with diameter much smaller than the lattice constant of the photonic crystal. Y. Liu *et al.* [69] further optimized the structure of the photonic crystal cavity (along with positions and diameters of the multiple holes inside the cavity), and they achieved a sensitivity of ~460 nm/RIU. Another type of the photonic crystal [71] widely used for refractive-index sensing is the one with an air slot engraved along the photonic crystal structures. The air slot is used as both optical waveguide and microfluidic channel, so that the light-matter overlap is greatly enhanced. A sensitivity of ~1500 nm/RIU was experimentally achieved with the air-slot photonic crystal refractometer demonstrated in [71], which is the highest sensitivity to date achieved with the photonic crystal refractometers. Assuming the detection limit of a spectral shift to be 0.1 nm, which is a typical resolution of the high-end optical spectrum analyzers, the sensitivity of ~1500 nm/RIU represents a sensor resolution of ~6×10^{-5} RIU. Among the advantages of photonic crystal sensors are small footprint, capability of integration into lab-on-chip devices, high quality factor of the microcavities, high sensitivity for surface sensing applications, and small volume of analytes required for sensing. Therefore, photonic crystal-based refractometry is very promising technique towards the development of compact and sensitive lab-on-chip refractometers. However, the fabrication of photonic crystals normally requires high resolution photo-lithography (or electron-beam-lithography) which is an expensive process [66-76]. Moreover, mass production of the photonic crystal sensors (especially the ones with artificial defects) with high repeatability remains a great challenge [76].

1.1.6 Optical ring resontor-based refractometers

Refractometers based on optical ring resonators have been under intensive investigation in the last decade due to their advantages such as high resolution, capability of integration into lab-on-chip devices, high quality factor, and small volume of test analytes required for sensing [77, 78]. In an optical ring resonator-based refractometer, the light from a lead-in waveguide (also called bus waveguide) is coupled into the ring resonator. At the resonant wavelengths of the ring resonator, the so-called whispering gallery modes (WGMs) would be excited around the surface of the ring resonator. These WGMs will manifest themselves as spectral dips in the resonator transmission spectrum with the dip positions corresponding to the resonant wavelengths. The

resonant wavelength of a WGM can be calculated as $\lambda_{WGM} = 2\pi r n_{eff}/m$, where r is the ring outer radius, n_{eff} is the effective refractive index of the WGM, and m is an integer denoting the WGM order. Variations in the refractive index of test analytes surrounding the resonator would modify the effective refractive index of a WMG, thus leading to displacements of the corresponding spectral dip. Consequently, the changes in analyte index can be then inferred from spectral shifts of the resonant wavelength, which constitutes the sensing mechanism of such refractometers. We note that an important factor that affects the sensing properties of a ring resonator refractometer is its quality factor (Q factor), which is defined as the ratio of the wavelength of a resonant dip to its FWHM. In principle, the Q factor is inversely proportional to the detection limit of such a refractometer, since a higher Q factor would result in a narrower resonant dip and thus a more precise reading of spectral shifts. To date, optical ring resonator-based refractometers have been implemented in three major configurations [77, 78] which are (1) chip-based ring resonators including ring- and disk- shaped resonators [79-82], (2) stand-alone dielectric microspheres [84-87], and (3) capillary fiber opto-fluidic ring resonators. In this section, we focus on the first two types, while the third type will be reviewed in Section 1.2.6 regarding to fiber-based refractometers.

Chip-based resonators generally have the advantages such as possibility of mass production and ease of optoelectronic integration. However, they normally have a relatively low Q factor (typically 10^3-10^5 in water) due mainly to the resonator surface roughness [78]. C-Y Chao *et al.* [79] used a polymer microring resonator of 45 μm in radius to measure refractive index changes of glucose solutions. The sensitivity was measured to be ~70 nm/RIU, and a detection limit of 5×10^{-5} RIU was achieved. Another glass-based ring resonator of 60 μm in radius was demonstrated in Ref. [80]. A sensitivity of 140 nm/RIU was achieved, and the detection limit was estimated to be 1.8×10^{-5} RIU. Besides, E. Krioukov *et al.* [81] developed a microdisk resonator on a SiO_2-Si_3N_4 platform. The experimental sensitivity was found to be ~23 nm/RIU, and the detection limit was 1×10^{-4} RIU. Recently, G-D Kim *et al.* [82] proposed that the sensitivity of a microdisk resonator can be enhanced by coating a thin high-index overlay on top of the resonator. Experimentally, they showed that the sensitivity was improved from 117 nm/RIU to 294 nm/RIU by coating a 40 nm thick TiO_2 (n~2.61) overlay on a ZPU13-430 polymer (n~1.43) microdisk. Note that the fabrication of chip-based resonators is normally a complicated and time-consuming

process, which may involve photo-lithographic processes and multiple chemical etching treatments [79-82].

Microsphere resonators, in general, feature very high Q factors ($>10^6$) due to their geometry and the extremely low surface roughness [78, 83]. A microsphere with a diameter of tens to a few hundred micrometers can be fabricated by simply melting the end of an optical fiber by a CO_2 laser or an acetylene/hydrogen-oxygen torch [78, 84, 85]. Using this method, N. M. Hanumegowda *et al.* [84, 85] developed a microsphere resonator-based refractometer. Although only a moderate sensitivity of ~30 nm/RIU was obtained, the detection limit of the sensor was as small as 10^{-7} RIU owing to its high Q factor (~5×10^6). The sensitivity of a microsphere resonator-based sensor may also be improved by coating a high-index layer on the microsphere [86, 87]. For example, O. Gaathon *et al.* [87] experimentally showed that by coating a 340 nm thick polystyrene film on a fluorine-doped silica microsphere, the sensitivity was increased by more than 700%. Note that the integration of a microsphere resonator with other opto-fluidic devices could be challenging, and it may require a tricky design of the opto-fluidic system and accurate positioning of each sensor component.

1.2 Review of fiber-based refractometers

1.2.1 Fiber refractometers based on the reflectivity measurements at the fiber/analyte interface
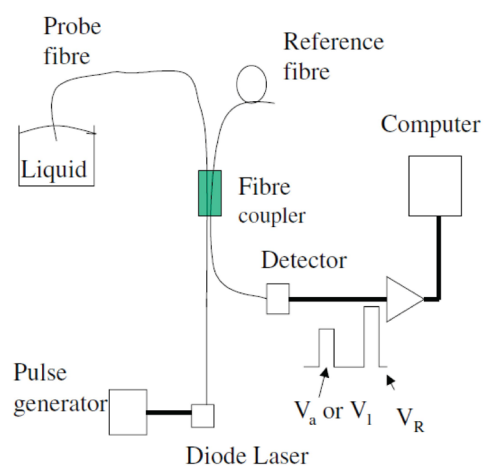
Figure 1.7   Schematic of the fiber refractometer based on the measurement of the Fresnel reflectivity at the fiber/analyte interface (Fig.1 from Ref. [88]).

Fiber refractometers based on the measurement of the Fresnel reflectivity at the fiber/analyte interface constitute the simplest type of the fiber-based refractometers. Such fiber refractometers are advantageous due to the ease of fabrication and the simplicity of the underlying sensing mechanism. Fig.1.7 shows a setup of the fiber refractometer based on the interrogation of the reflectivity at the fiber/analyte interface [88]. The fractional reflectivity, R, at the fiber/analyte interface can be calculated using the Fresnel formula: $R = (n_c - n_a)^2 / (n_c + n_a)^2$, where n_c and n_a represent the refractive indices of the fiber core and the test analyte, respectively. One can infer the changes in refractive index of the analyte by measuring the changes in the reflectivity at the fiber/analyte interface. Using this sensing principle, M. S. Meyer *et al.* [89] demonstrated that refractive index can be measured with an average accuracy within 0.2% of the true value, which corresponds to a refractive-index resolution of 0.003 RIU. This resolution was later improved to be on the order of $\sim 1 \times 10^{-4}$ RIU by using a parabolic-shaped fiber tip or a tapered fiber tip as the fiber probe [90]. P. Nath *et al.* modified this technique into a "non-intrusive" sensing regime by adding an objective lens between the fiber tip and the analyte, so that the fiber refractometer can be used with chemically aggressive analytes such as hydrofluoric acid [91]. Currently, fiber refractometers based on detection of the fiber/analyte reflectivity are used commercially and are known as Fiber-optic Endface Refractometers (for example, see a system from FORC-PHOTONICS [5]). Some disadvantages of these fiber refractometers include signal sensitivity to bending of the probe fiber, as well as signal sensitivity to the intensity fluctuations of the light source. Moreover, the resolution of these simple sensors is also relatively poor compared to more advanced fiber refractometers demonstrated in the following sections.

1.2.2 Fiber refractometers based on evanescent-field detection

Fiber refractometers based on evanescent-field detection are another type of fiber refractometers that use the amplitude-based detection modality. As shown in Fig.1.8, in such sensors the cladding of the fiber is partially or completely removed by either mechanical polishing or chemical etching, so that the evanescent field of fiber core-guided modes would efficiently overlap with the analytes under test [6-8].
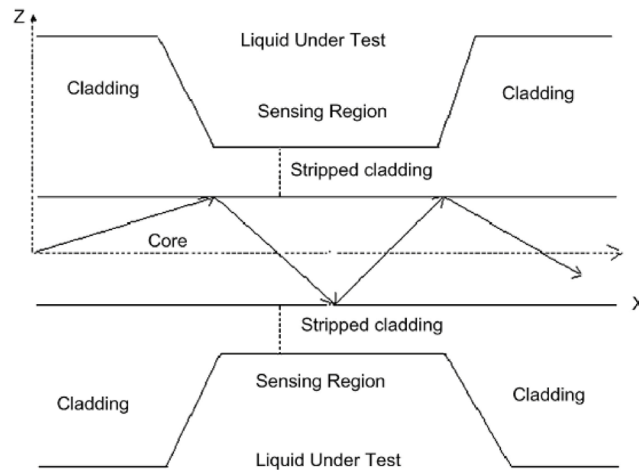
Figure 1.8   Schematic of the fiber refractometer based on evanescent-field detection (Fig.2 from Ref. [8]).

The presence of liquid analytes with different refractive indices in the unclad region of the fiber modifies the modal confinement condition, thus leading to changes in the transmitted intensity of a fiber. From the basic theory of fiber optics, the V parameter (normalized frequency) of a step-index fiber is given by $V = \frac{2\pi r}{\lambda} \sqrt{n_c^2 - n_l^2}$, where r is the radius of the fiber core, λ is the wavelength of guided light, and n_c and n_l are the refractive indices of the fiber core and cladding, respectively. Since the number of guided modes of a fiber is proportional to V^2, then, increasing the cladding refractive index would reduce the number of guided modes, and at the same time reduce the confinement of the guided modes, thus changing the transmittance of the fiber. Another critical parameter related to evanescent-field sensing is the core mode penetration depth into the cladding region d_p, which is defined as $d_p = \lambda / 2\pi n_1 (\sin^2 \theta - (\frac{n_2}{n_1})^2)^{1/2}$, with θ being the incident angle of the core-guided light onto the core/cladding interface. Generally, the greater the penetration depth is, the higher the sensor sensitivity is, due to increased modal overlap with analyte. In this respect, the evanescent-field fiber refractometers become more sensitive for analytes with refractive indices close to that of the fiber core [7, 92]. Other methods that enhance the light-matter overlap in the evanescent-field fiber refractometer include tapering fibers into microfibers [9-11, 93], and U shaping of the unclad fibers [94, 95]. As far as sensitivity is concerned, evanescent-field refractometers can show moderate-to-high sensitivities. M. Sheeba *et al.* [6] demonstrated a side-polished evanescent-field fiber refractometer for the detection of adulterant traces in coconut oil with a refractive index resolution of 10^{-3} RIU. In [9], a

refractometer based on a tapered fiber was demonstrated, and the resolution was found to be below 10^{-4} RIU. Besides, C. Sui *et al.* [93] also proposed an evanescent-field microfiber refractometer operating on an optical heterodyne frequency modulation technique. Experimental results showed that the device was capable of measuring an index variation on the order of $\sim 10^{-5}$ RIU. Among the merits of fiber refractometers based on evanescent-field detection are the simplicity of sensor structure, low cost, small footprint and a simple sensing mechanism, while the main disadvantage of such sensors is their poor mechanical robustness due to the fiber tapering or cladding-stripping process.

1.2.3 Fiber refractometers based on surface plasmon resonance

Fiber refractometers based on surface plasmon resonance operate near the frequency of phase matching between a core-guided fiber mode and a very lossy plasmon mode propagating at the metallized core/cladding interface. This phase matching between the two modes is possible as the effective refractive indices of the core-guided fiber mode and the plasmon are both higher than the refractive index of the cladding material. Practically, the excitation of a surface plasmon manifests itself as a dip in the fiber transmission spectrum with its spectral location corresponding to the frequency of phase matching between a particular core-guided fiber mode and a surface plasmon. Similarly to the case of the evanescent-field fiber sensors, experimental implementation of the fiber-based SPR sensors requires etching or polishing of the fiber cladding with a subsequent deposition of several 10s of nanometer thick metallic layer (silver or gold layer) onto the core surface (see Fig.1.9). In this design, the evanescent field of the core-guided fiber mode would penetrate into the metallic layer and the dielectric medium, thus exciting the SPW along the metal/dielectric interface.
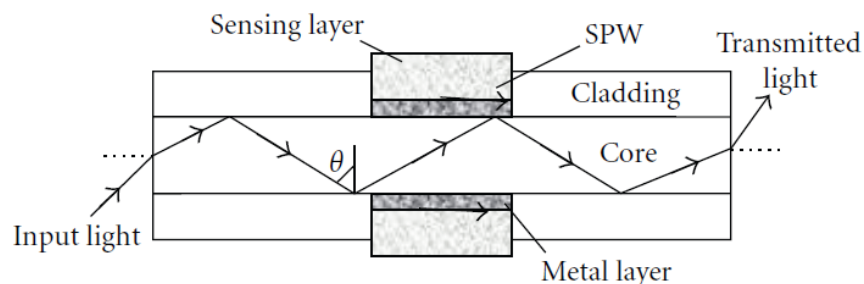
Figure 1.6   Schematic of the fiber-based SPR sensor (Fig.9 from Ref. [96]).

As shown in Fig.1.9, the light from a broadband source is launched into the fiber core and is guided by the total internal reflection occurring at the core/cladding interface. Consequently, the evanescent field of the core-guided mode would excite a lossy surface plasmon wave along the metallized section of the core. The SPR excitation is only efficient at the phase-matching frequency between a particular core guided mode and a plasmonic mode [64, 97]. At such a resonant frequency, the transmission spectrum of the fiber-based SPR sensor features a spectral dip due to efficient excitation of a lossy surface plasmon. Variations in the refractive index of an analyte adjacent to the metal layer would result in the spectral shifts of the resonant wavelength. This will manifest itself as the spectral shifts of the corresponding absorption dip in the fiber transmission spectrum, which can be then used to extract the changes in the analyte refractive index. This constitutes the operating principle of the fiber-based SPR sensors. Y. Lin [98] demonstrated a fiber-based SPR sensor using a side-polished multimode fiber coated with a gold film, and the sensitivity was reported to be ~1570 nm/RIU. N. Cennamo $et\ al.$ [99] used a fairly similar fiber-based SPR setup with an improved sensitivity of ~2500 nm/RIU by optimizing the thickness of the metallic layer. Some researchers coated an additional high-index dielectric overlayer on the metal film in order to protect the metal coating and to increase the sensitivity. For example, P. Bhatia $et\ al.$ [100] demonstrated that the sensitivity of the fiber-based SPR sensor can be improved by optimizing thickness and refractive index of the overlayer. They showed that a 10 nm thick silicon overlayer would improve the sensitivity from ~2800 nm/RIU to ~5200 nm/RIU. Moreover, J. H. Ahn $et\ al.$ [101] demonstrated a fiber-based SPR configuration in which a metal-dielectric-metal multilayer was deposited on top of a side-polished fiber, such that multiple SPR modes could be excited. This technique enables multiplex wavelength applications and provides self-reference signals for sensing measurements. Tapered fibers can also be used in SPR sensing applications. In Ref. [102], the authors demonstrated a single mode fiber with a tapered sensing region coated with a gold layer. The coated layer featured a semi-cylindrical shape rather than a planar shape, which leads to the excitation of several hybrid SPR modes and the appearance of several resonance dips in the fiber transmission spectrum. The sensitivity of this fiber SPR sensor was found to be 1.2×10^5 nm/RIU. Such a dramatic sensitivity is equivalent to a resolution of 7×10^{-7} RIU, assuming that a spectral shift of 0.1 nm can be accurately measured. However, the measurement range of this sensor was limited to 0.02 RIU, since the spectral shift of the SPR mode would lead to considerable deformation or even

disappearance of the resonant dips. Currently, this fiber SPR sensor is one of the most sensitive refractive index sensors and is particularly suitable for bio-medical sensing applications including detection of DNA hybridization, peptide-antibody interactions, immunoreactivity of antibody conjugates and polymerase chain reactions [103, 104], to name a few. Other advantages of the fiber SPR sensors include flexible sensing-structure designs, miniaturized sensor systems, and the capability of remote sensing. The drawback of this technique is that it requires complicated fabrication process such as fiber tapering or polishing, precisely-controlled metal-layer coating as well as design of a complex opto-fluidic system [103].

1.2.4 Fiber grating refractometers

Fiber gratings can be generally categorized into two subclasses, i.e., fiber Bragg gratings (FBGs) and long-period gratings (LPGs). A FBG, that features a grating constant on the sub-micron order, is usually inscribed in the photosensitive core of a single mode fiber. A FBG is able to couple a forward-propagating core mode of the optical fiber into a backward, counter-propagating mode at the resonant wavelength of the Bragg grating. Thus, the reflection spectrum of a FBG has a spectral peak at the resonant wavelength, λ, given by $\lambda = 2n_{eff}\Lambda$, where n_{eff} is the effective refractive index of the fiber core mode, and Λ is the periodicity of the FBG. Changes in the refractive index of a test analyte adjacent to a FBG would modify the effective refractive index of the fiber core mode, thus shifting the resonant wavelength of the FBG. Therefore, FBG refractometers operate on a spectral-based detection modality, in which variations in the refractive index of a test analyte could be extracted from spectral shifts of the grating resonant wavelength [105]. FBG refractometers are usually constructed using one of the three following methods: (1) etching (partially or completely) the fiber cladding, so that the evanescent field of the fiber core modes could penetrate into the test analytes [106-111]; (2) using a microfiber Bragg grating that has an inherently strong evanescent-field overlap with the test analytes [14, 112, 113]; (3) using a tilted fiber Bragg grating to couple core-guided light to backward-propagating cladding modes [114-116]. Note that the sensitivity of a FBG refractometer is normally a nonlinear function of the refractive index of a test analyte. When the refractive index of a test analyte approaches to that of the fiber core, a higher fraction of the evanescent field of the fiber core modes penetrates into the test analyte, thus resulting in a higher sensitivity. A. Asseh *et al.* [107] proposed a FBG refractometer in which the cladding of the FBG is stripped

using a chemical etching method. Theoretically, the sensitivity of this FBG refractometer was calculated to be ~220 nm/RIU at the refractive index value of ~1.45. Schroeder *et al.* [13] demonstrated a FBG refractometer in which the cladding of a FBG is stripped off using a fiber side-polishing technique, and this FBG refractometer achieved an experimental sensitivity of ~300 nm/RIU at the refractive index value of ~1.45. In Ref. [14], a microfiber Bragg grating refractometer with a 2 μm diameter was fabricated using a flame-brushing method, and a sensitivity of 231.4 nm/RIU was obtained at refractive index value of ~1.44. K. Zhou *et al.* [117] demonstrated a FBG refractometer with a micro-slot engraved along the grating. This FBG constitute a liquid-core waveguide by filling the micro-slot with high-index optical oils, and a strong overlap between the test analyte and the fiber core-guided mode was achieved. The sensitivity of this FBG refractometer was measured to be ~945 nm/RIU; however, the measuring range of this refractometer was limited to $n_{analyte}$ >1.45. An advantage of the FBG refractometer is that the width of its reflection peak is relatively narrow (FWHM: 10-70 pm), which allows a precise reading of the wavelength shift in its reflection spectrum. [118]. However, on the negative side, FBG refractometers normally suffer from poor mechanical robustness due to the fiber cladding modification or tapering process [117]. Moreover, the sensitivity of a FBG refractometer is typically a nonlinear function of the refractive index of test analytes, and FBG refractometers only show high sensitivities to refractive-index variations, when the refractive index of test analytes approaches to that of the fiber core [117].

A long period grating typically has a grating constant ranging from tens to several hundred micrometers [119-129]. A long period grating could couple a fiber core mode into multiple forward-propagating cladding modes that are quickly attenuated. Therefore, the transmission spectrum of a LPG normally features multiple spectral loss bands (spectral dips) corresponding to the distinct cladding modes. The m-order resonant wavelength, $\lambda^{(m)}$, of a LPG can be calculated by $\lambda^{(m)} = (n_{eff} - n_{cl,m})\Lambda$, where n_{eff}, $n_{cl,m}$ are the effective refractive indices of the core mode and m-order cladding mode, and Λ is the period of the LPG. The operating principle of a LPG refractometer is that, changes in the refractive index of a test analyte adjacent to the LPG could directly vary the effective refractive index of the fiber cladding modes, thus shifting the resonant wavelengths of the LPG. Therefore, LPG refractometers normally do not require fiber-cladding stripping. In 1997, V. Bhatia *et al.* [120, 121] used a LPG written on a single mode fiber to measure variations in the refractive index of liquid analytes, and their LPG refractometer

achieved a sensitivity of ~400 nm/RIU in the refractive index range of 1.33-1.43. Methods to improve the sensitivity of LPG refractometers may include: (1) fabricating the LPG on a tapered fiber or a D-shape fiber [122-124, 129]; (2) choosing the proper high-order cladding mode for spectral interrogations [125, 126]; or (3) functionalizing the LPG with high-index overlayers [127, 128]. G-R. Lin *et al.* demonstrated a LPG refractometer which was fabricated by writing a LPG on the high-index layer coated on top of a D-shape fiber, and this refractometer achieved a sensitivity of ~1000 nm/RIU. Z. Yin *et al.* [122] experimentally demonstrated a refractometer based on a LPG written on a tapered fiber, and the sensitivity was measured to be 2733.28 nm/RIU in the measuring range of 1.449-1.453. In Ref. [128], a LPG, coated with alternating layers of polyallylamine-hydrochloride (PAH) and SiO_2, was used for sensing of variations in the refractive index of liquid analytes. This LPG refractometer has a sensitivity of 1927 nm/RIU in the measuring range of 1.323-1.491. We note that LPGs potentially could be developed into compact, highly sensitive fiber refractometers. However, LPGs usually have broader resonance bands, as compared to those of FBGs, which would generally make it less precise to determine the peak (or dip) positions in their transmission spectrum [118]. Moreover, we note that for both FBG refractometers and LPG refractometers, cross sensitivity to fiber strain, bending, and temperature should be minimized in order to maintain the accuracy of refractive index measurements.

1.2.5 Fiber refractometers based on interferometric techniques

In the last two decades, the research of combining traditional interferometric techniques with optical fibers has been carried out extensively. The principal advantage of fiber-optic interferometers, compared to their traditional counterparts, is that they can be miniaturized for micro-scale applications, because traditional bulk optical components such as beam splitters, combiners, and objective lenses have been replaced by small-sized fiber devices. In a fiber-optic interferometric refractometer, the guided light is split into different components propagating along different (in-fiber) paths, or the guided light is coupled into different modes. Then the recombination of these components (or modes) would generate interference. Changes in the refractive index of an analyte would introduce a phase difference to the light guided in one of the paths, thus resulting in intensity variations or spectral shifts in the fiber interference spectrum. Consequently, changes in the refractive index of test analytes can be then inferred from the

intensity variations or spectral shifts. This constitutes the general operating principle of fiber-optic interferometric refractometers based on M-Z interferometers, Fabry-Perot (F-P) interferometers and Sagnac loop interferometers [16-21, 130-139], to name a few. In this thesis, we take the fiber-optic F-P refractometer as an example to demonstrate fiber refractometers based on interferometric techniques. A fiber-based F-P interferometer can be simply created by building up reflectors outside (extrinsic F-P configuration) or inside (intrinsic F-P configuration) fibers.
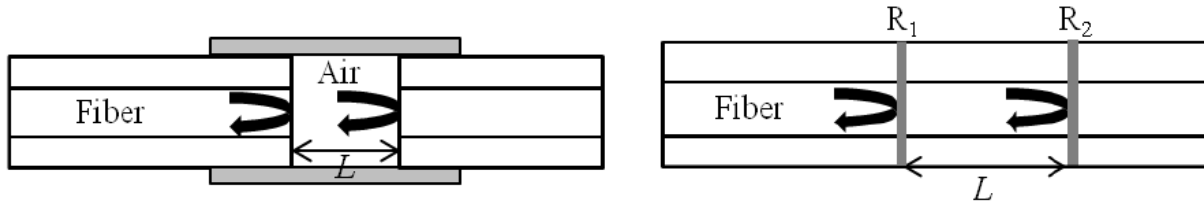
Figure 1.10   Schematic of fiber refractometers using (a) the extrinsic F-P configuration and (b) the intrinsic F-P configuration (Fig. 1 from Ref. [130])

Fiber refractometers using the extrinsic F-P configuration typically employ an external cavity formed outside the fibers [130], as shown in Fig.1.10 (a). A F-P cavity can be formed by fixing the tips of two fibers in a supporting structure. For example, J. L. Elster *et al.* [131] demonstrated a fiber refractometer using the extrinsic F-P configuration. In their design, two SMFs were glued on a silicon substrate, and there was a small gap (F-P cavity) between the fiber tips. Changes in the refractive index of a liquid analyte filling the F-P cavity would change the optical length of the F-P cavity, thus modifying the free spectral range (FSR) in the reflection spectrum of the F-P refractometer. Thus, this refractometer was characterized by interrogating the change in the FSR in response to the refractive index variation of liquid analytes. The resolution of this refractometer was found to be ~1×10^{-6} RIU. Y. Tian *et al.* [132] demonstrated another fiber-based F-P refractometer using an experimental setup similar with that in Ref. [131]. This refractometer, however, operates using a different sensing mechanism, in which changes in the refractive index of test analytes were characterized in response to spectral shifts of the peak positions in the interference spectrum. The sensitivity of this refractometer was 665.9 nm/RIU, and the resolution was 6×10^{-6} RIU. The advantages of fiber-based extrinsic F-P refractometers include ease of fabrication, and low cost. Besides, it is possible to obtain high-finesse interference signals, since reflective films can be easily coated on the reflection surfaces (fiber tips) [130].

However, fiber-based extrinsic F-P refractometers have disadvantages such as susceptibility to environmental fluctuations, low coupling efficiency, and packaging problems [130-132].

Fiber refractometers using the intrinsic F-P configuration have the reflectors within the fibers as plotted in Fig.1.10 (b). The in-fiber F-P cavity can be created by fs-laser micro-machining methods [133-135], chemical etching methods [138, 139], or using multiple fiber Bragg gratings [136, 137]. In the last decade, many fiber refractometers based on the intrinsic F-P configuration have been proposed. These fiber-based intrinsic F-P refractometers generally operate on a spectral-detection based modality, in which changes in the refractive index of a liquid analyte filling the F-P cavity are characterized in response to shifts of the spectral signatures (spectral peaks or dips) in the interference spectrum. K. Zhou *et al.* [134] fabricated a fiber-optic intrinsic F-P refractometer by using an fs-laser to mill a microfluidic channel in the core of a SMF, and by writing two FBGs at the two sides of the microfluidic channel. The sensitivity of this refractometer strongly depends on the width of the microfluidic channel. With a 35 μm wide microfluidic channel, this refractometer showed a sensitivity of 9 nm/RIU. T. Wei *et al.* [135] demonstrated a miniaturized fiber-optic intrinsic F-P refractometer fabricated by milling a micro-notch cavity in a single mode fiber. The sensitivity was characterized by measuring the temperature-dependent refractive index of de-ionized water, and the sensitivity was found to be 1163 nm/RIU. L. Mosquera *et al.* [136] demonstrated a fiber-based intrinsic F-P refractometer fabricated by sandwiching a LPG between two FBGs. The LPG enables the light confined between the two FBGs to interact with the surrounding medium. The sensitivity of this refractometer was measured to be ~4.72 nm/RIU. Another method for fabricating fiber-optic intrinsic F-P refractometer is based on chemical etching. For instance, E. Cibula *et al.* used HF to chemically etch the cladding of a short SMF, and this unclad SMF was then spliced with two leading fibers containing in-fiber mirrors [139]. The sensitivity of this refractometer is a nonlinear function of the refractive index of test analytes, and is dependent on the diameter of the unclad fiber. The highest sensitivity of this refractometer was found to be 830 nm/RIU at refractive index value of 1.44, when a 4 μm diameter unclad fiber was used. The fiber refractometer using the intrinsic F-P configuration normally has an in-line fiber structure that offers several advantages such as ease of alignment, high coupling efficiency, and high stability. On the negative side, the fabrication of such an in-line structure usually requires significant fiber processing such as fiber splicing, polishing, etching and microstructure machining.

1.2.6 Capillary fiber refractometers

Capillary fibers are seldom used independently as fiber refractometers. As a matter of fact, refractive indices of most dielectric materials are greater than those of aqueous analytes (n~1.33), such that a capillary waveguide filled with aqueous analytes does not guide by total internal reflection, but by a leaky-mode guiding principle, thus limiting considerably the sensing length of a capillary fiber sensor [153]. Currently, only a few polymers, such as Teflon AF (n~1.29), have refractive indices lower than those of aqueous analytes.
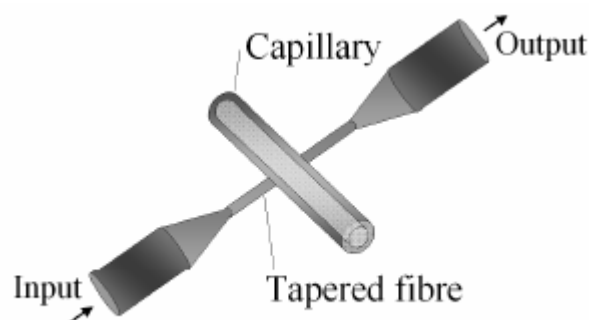
Figure 1.11   Schematic of the liquid-core optical-ring-resonator sensor (Fig. 1 from Ref. [140])

However, a capillary fiber can be used in combination with a tapered fiber to constitute a liquid-core optical ring-resonator sensor (LCORRS) as shown in Fig. 1.11. In a LCORRS, the light propagating in the tapered fiber is coupled into the liquid-filled capillary, and excites whispering gallery modes (WGMs) localized on the capillary surface. The resonant wavelength of a WGM shifts when the refractive index of a liquid analyte filling the capillary changes. The sensitivity of a LCORRS can be affected by several factors such as thickness and radius of the capillary, and the mode order of the WGM [141]. Generally, reducing thickness of the wall of the capillary fiber could increase the sensitivity of a LCORR, since a higher power fraction of the WGM would overlap with test analytes filling the capillary. I. White *et al.* [142-144] demonstrated that the sensitivity of a LCORRS is between 10 and 50 nm/RIU, when the thickness of a capillary wall is in the range of 3-6 μm. V. Zamora *et al.* [140] showed that the sensitivity could be increased to ~170 nm/RIU, if the thickness of a capillary is further reduced to ~1 μm. However, reduction of the thickness of a capillary always comes at the cost of its mechanical robustness. Therefore, M. Stumetsky *et al.* [145] proposed to host both a capillary fiber and a tapered fiber within a low-index polymer matrix. In this LCORRS, the wall of the

capillary fiber can be etched down to the sub-micron scale. The sensitivity of this LCORRS was measured to be as high as ~800 nm/RIU. Moreover, Ling and Guo [146] used a glass prism, instead of a tapered fiber, to couple light into a liquid-filled capillary fiber in order to increase the modal overlap between the WGMs and test analytes, which resulted in a sensitivity of 600 nm/RIU. We note that although LCORRSs show relatively high sensitivities to variations of the refractive index, the alignment and maintenance of the LCORR setups are normally challenging due to fragileness of the tapered fibers and the hollow-core capillaries

1.3   Microstructured optical fiber refractometers

Microstructured Optical Fibers (MOFs) and photonic bandgap fibers (a sub-set of MOFs), refer to optical fibers that have specially-patterned micro-sized holes running along all their length. Compared to traditional step-index fibers, MOFs show several advantages for refractive index measurements [4]. Firstly, MOFs by their nature could accommodate liquid or gaseous analytes within their hollow microstructure. Secondly, MOFs generally can be used directly for refractive index measurements without any fiber modifications such as fiber-cladding polishing or etching. This would benefit mass production of the MOF refractometers. Lastly, hollow-core MOFs could achieve an almost-complete modal overlap with test analytes, thus leading to an extremely high sensitivity for refractive index measurements. In general, MOFs can be divided into two classes, i.e., solid-core MOFs (Fig.1.12 (a)) and hollow-core MOFs (Fig.1.12 (b and c)). Solid-core MOFs typically guide with a modified total internal reflection principle, which is similar to the guidance of traditional step-index fibers; however, when used for sensing of refractive index variations, solid-core MOFs are usually used to detect liquid analytes with the refractive indices higher than those of the fiber materials (e.g. $n_{analyte} > 1.45$ for silica MOFs) [147-149]. Thus, the guidance of the solid-core MOFs turns into the photonic bandgap guidance. Fiber refractometers based on solid-core MOFs filled with high-index analytes generally use the spectral-detection based modality. Variations in the refractive index of a liquid analyte filling the fiber would modify the bandgap guidance of the solid-core MOF, leading to spectral shifts in the fiber transmission spectrum. Thus, the spectral shifts can be then used to extract the changes in the refractive index of test analytes. In Ref. [147], a solid-core MOF sensor was theoretically proposed for sensing of high-index liquid analytes, and the sensitivity was calculated to be ~1200 nm/RIU at the refractive index value of 1.58. X. Yu *et al.* [149] experimentally demonstrated a

solid-core MOF refractometer and the sensitivity was ~1500 nm/RIU at refractive index value of 1.52. D. K. C. Wu *et al.* [150] reported an ultrasensitive solid-core MOF refractometer that operates by coupling the core mode to a mode localized in the adjacent analyte-filled hole at the frequency near the core-mode cutoff. The experimental sensitivity of this refractometer was as high as 30100 nm/RIU; however, this refractometer used a complicated selective-filling method to fill liquid analytes into the MOF, and the measuring range is limited to be $n_{analyte} > n_{silica}$.
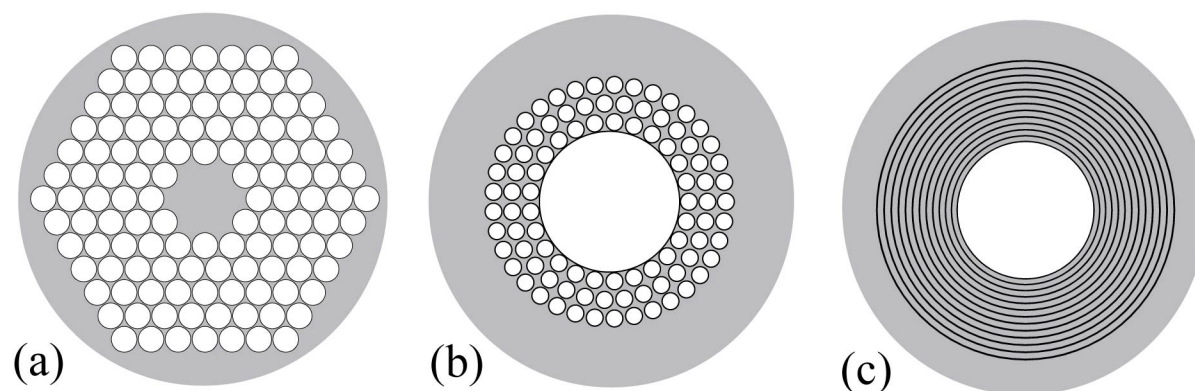
Figure 1.12   Various types of MOFs. (a) Solid-core MOF featuring a solid core surrounded by a periodic array of air holes. (b) Hollow-core MOF featuring a hollow core surrounded by several rings of small air holes. (c) Bragg fiber featuring a large hollow core surrounded by a periodic sequence of high and low refractive index layers. (Fig. 2 from Ref. [4])

The sensing mechanism of hollow-core MOF refractometers [4] is the same with that of their solid-core counterparts, i.e., interrogation of spectral shifts in response to the changes in the refractive index of a liquid analyte filling the fiber; however, there is no lower limit to the measuring range of refractive index. Besides, hollow-core MOF refractometers can achieve almost 100% modal overlap with analytes, thus resulting in a very high sensitivity for refractive index measurements. In [23, 151], two hollow-core MOF refractometers were experimentally used for sensing of aqueous solutions. The sensitivities of both refractometers were measured to be ~5000 nm/RIU. However, infiltration of the liquid analytes into the microstructure of the MOF was time-consuming (~10 minutes for 20 cm long fiber [22, 23]) due to the micro-sized holes in the MOF.

As shown in Fig.1.12 (c), there is a special type of the hollow-core MOF, i.e., hollow-core photonic bandgap Bragg fiber, which features a large hollow core surrounded by an alternating high and low index multilayer as a Bragg reflector. The core diameter of a hollow-core Bragg

fiber typically ranges from 50 microns to 1 mm. Such a large core facilitates filling it with liquid analytes, which significantly shorten response time of the fiber sensor. The sensitivity of a Bragg fiber refractometer is dependent on the thicknesses of the individual layers in the Bragg reflector as well as the refractive-index contrast (refractive index difference between the high and low index layer) of the Bragg reflector [4]. In 2009, our group [4] proposed the possibility of using a hollow-core low-refractive-index-contrast Bragg fiber as a fiber refractometer, and theoretically demonstrated that the sensitivity of such a Bragg fiber refractometer could be on the order of 5000 nm/RIU. In 2012, a hollow-core high-refractive-index-contrast Bragg fiber refractometer [152] was experimentally demonstrated by K. J. Rowland *et al.* with the sensitivity found to be ~330 nm/RIU. In this thesis, we are going to use hollow-core low-index-contrast Bragg fibers for sensing of changes in the refractive index of a liquid analyte filling the fiber core. The sensitivity of this refractometer, compared to that of the refractometer reported in [152], is considerably improved, and is found to be ~1400 nm/RIU [153, 154]. The detection limit of this Bragg fiber refractometer can be as small as ~7×10^{-5} RIU, assuming that a spectral shift of ~0.1 nm can be reliably detected.

In this section, we have already demonstrated that a MOF by itself can be directly used as a fiber refractometer. As a matter of fact, the function of a refractometer can also be implemented by MOFs utilizing fiber Bragg gratings [155-158], long period gratings [159-168], SPR effects [169-171], fiber interferometric techniques [173-183], and fiber non-linear effects [172]. All these techniques, which are summarized in Table 1.1, significantly enrich the sensing scenarios of MOF-based refractometers, and make MOFs very promising for the development of the new generation of fiber refractometers.

Table 1. 1   Refractometers based on MOFs using gratings, SPR effects, interferometric techniques and fiber non-linear effects.

MOF-based sensors	Sensing mechanism	Wavelength	Sensitivity	Ref.
MOF sensors with FBGs	Detection of spectral shifts of the FBG resonant wavelength	1530-1554 nm	~1300 nm/RIU @ n~1.45	[155, 156]
		1500-1550 nm	~1600 nm/RIU @ n~1.41	[157]
		1525-1550 nm	45 nm/RIU@n~1.41	[158]
MOF sensors with LPGs	Detection of spectral shifts of the LPG resonant wavelength	1300-1500 nm	~250 nm/RIU	[159, 160]
		600-1100 nm	1500 nm/RIU	[161]
		1500-1625 nm	2262 nm/RIU	[162]
		1100-1700 nm	~70 nm/RIU	[163]
		1200-1625 nm	517 nm/RIU	[164]
		700-1100 nm	1.4 nm/nm (surface sensing)	[165]
		1530-1620 nm	~98 nm/RIU	[166]
		1250-1500 nm	338.3 nm/RIU	[167]
		1000-1200 nm	1790 nm/RIU	[168]
MOF sensors based on SPR	Detection of spectral shifts of the SPR resonant wavelength	200-900 nm	~2700 nm/RIU	[169]
		400-800 nm	~2000 nm/RIU	[170]
		500-1700 nm	-	[171]
MOF sensors using nonlinear-optical effects	Detection of spectral shifts of the transmission peaks arising from four-wave mixing	600-1200 nm	~8800 nm/RIU	[172]
MOF sensors based on in-fiber interferometers	Detection of spectral shifts of the transmission peaks (or dips) arising from multimode interference	1520-1600 nm	252 nm/RIU	[173]
		1150-1350 nm	-	[174]
		1470-1570 nm	171.96 nm/RIU	[175]
		1275-1310 nm	-	[176]
		1520-1600 nm	24.67 nm/RIU	[177]
		1520-1570 nm	805 nm/RIU@ n~1.00026	[178]
		1525-1600 nm	500 nm/RIU	[179]
		1540-1600 nm	-	[180]
		1450-1650 nm	1851.3 nm/RIU	[181]
		1530-1620 nm	1629 nm/RIU	[182]
		1260-1600 nm	-	[183]
	Detection of changes in the visibility of the interference pattern	1520-1570 nm	~4.59 /RIU	[184]

1.4   Review of optical spectrometers

As mentioned in the introduction, spectroscopic instruments play a key role in refractometers based on a spectral-based detection modality. In this section, we provide a brief review of several typical spectrometers and perform an analysis of their advantages and limitations when integrated with fiber-based sensors.

1.4.1   Spectrometers based on prisms

In the late seventeenth century, Newton discovered that prisms are capable to disperse visible light, and ever since then prisms have been used as dispersive elements in spectrometers [185]. Fig.1.13 demonstrates the operating principle of a prism-based spectrometer. The test light passing through the entrance slit is collimated by the first lens, and then dispersed by the prism into different wavelength components. The dispersed light is then focused onto the plane of the exit slit. Only the light with the desired wavelength could pass through the narrow exit slit, and is then measured by a photodetector. The complete spectrum could be measured by adjusting the prism angle or the position of the exit slit. The resolution of a prism-based spectrometer is generally limited by the width of the (entrance and exit) slits, the length of the optical path inside the spectrometer, as well as the dispersion power of the prism. The selection of materials for producing a prism is important to prism-based spectrometers. Firstly, the prism material should be transparent to the light of interest; otherwise, no light reaches the detector. For quartz [186], including both the crystalline and fused form, the transparent wavelength range spans from the ultraviolet (as low as 180 nm) to the infrared (2.5 micron). Glass could transmit visible and infrared light, and the transparent wavelength range spans from 400 nm to 3.5 micron [186]. In addition, the derivative of the refractive index of the prism to wavelength, $dn/d\lambda$, should be properly chosen along with the incident angle of the light, the geometry of the prism, and the focal length of the lens after the prism, in order to meet the resolution requirements of the spectroscopic measurements.
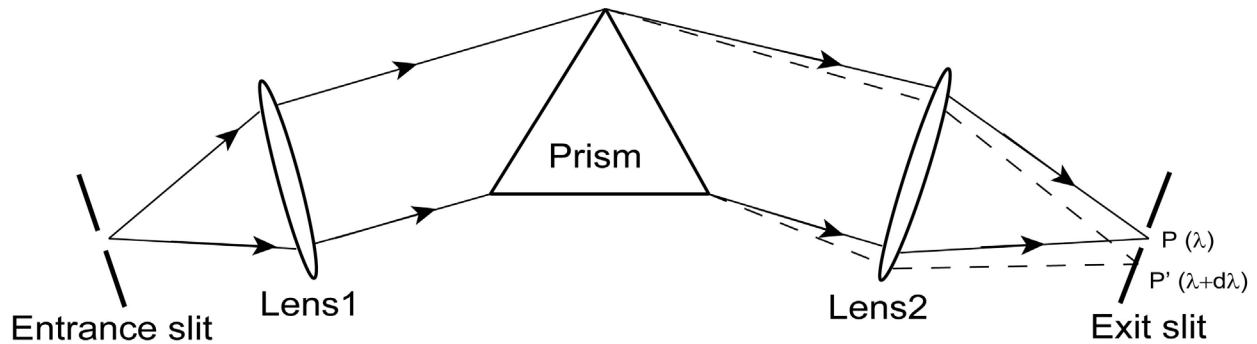
Figure 1.13   Schematic of a prism-based spectrometer [186].

The advantages of prism-based spectrometers include simple structure, low cost and ease of operation. Compared to grating spectrometers, prism-based spectrometers have less optical losses in the quartz ultra-violet region. Besides, Prism-based spectrometers could measure spectra without ambiguity caused the overlapping of the light in different diffractive orders. A disadvantage of prism-based spectrometers is its low resolving power, as compared to grating-based spectrometers and interferometer-based spectrometers. Moreover, some particular prisms [186] made from hygroscopic materials (e.g. rock salt) can only be used in a moisture-free environment, thus leading to the limitation for their applications. Nowadays, prism-based spectrometers are gradually replaced by grating-based spectrometers.

1.4.2 Spectrometers based on gratings

A diffraction grating is fabricated by ruling many equally-spaced paralleled grooves on a plane or concave substrate. The theory of diffraction gratings was developed by Rowland in 1893 [185]. The fundamental principle [186, 187] of a diffraction grating is illustrated in Fig.1.14 (a). A collimated beam is projected on a diffraction grating at an angle θ_i relative to the grating normal. Each groove in the grating diffracts the incident beam. The angle, θ_r, of the diffracted beam is determined by the condition that the diffracted components from the different grooves add up in phase with each other [186]. This would occur when the optical path difference between the adjacent diffracted components is an integral multiple of the operating wavelength. The grating equation is given as: $d(\sin\theta_i + \sin\theta_r) = m\lambda$, where d is the period of the grating; m is the diffraction order (an integer); λ is the wavelength of the diffracted light.
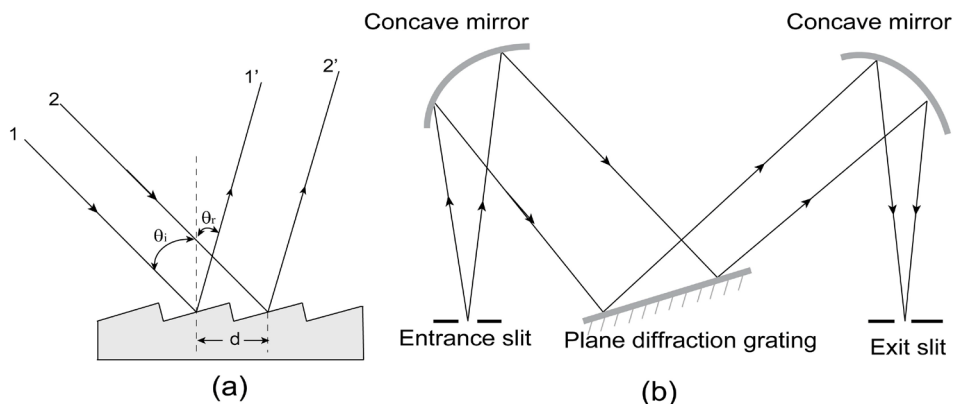
Figure 1.14 (a) Schematic of a diffraction grating, and (b) schematic of a grating-based spectrometer using the Czerny-Turner design [186].

During the last 100 years, various designs of grating-based spectrometers have been proposed. In this thesis, we take the grating spectrometer using the Czerny-Turner (C-T) design (see Fig.1.14 (b)) as an example to demonstrate the operating principle of grating-based spectrometers. In the C-T design, the test light passes through the entrance slit, and is reflected by the first concave mirror to the diffraction grating. The grating in turn diffracts the light to the second concave mirror, which then focuses the light to the plane of the exit slit. Only the light with desired wavelength could pass through the narrow exit slit and then is measured by a photodetector. By adjusting the angle of the grating, the wavelength of the light can be varied at the exit slit. The resolution of the spectrometer depends on the width of the (entrance and exit) slits, the line density of the grating, and the length of the optical path inside the spectrometer. To improve the resolution, some grating-based spectrometers use two gratings or direct light to diffract twice on the same grating, so that the overlapping of light in different diffraction orders would be eliminated [185, 186]. The typical resolution of the high-end grating-based spectrometers can be ~10-100 pm. Nowadays, grating-based spectrometers become the mainstream spectroscopic devices for both scientific and industrial applications, though they still have limitations. We note that spectrometers based on movable gratings require a relatively long time for the acquisition of broad-band spectra, which is unfavorable for sensing of rapid chemical or biological processes. Besides, the measuring range of a grating-based spectrometer is also limited due to overlapping of different diffraction orders [186]. Finally, the resolution of a spectrometer generally scales as the optical path length inside a spectrometer, which makes grating-based spectrometers difficult to miniaturize without the loss of its resolution. Therefore, most of the

grating-based spectrometers are mainly used in laboratory applications due to high costs and relatively large size of such systems.

1.4.3 Fourier transform spectrometers

The interferogram for an interferometer records the superimposed light signals of all the different wavelengths projected on a detector. The spectrum of the test light could be recovered from the Fourier transform of the interferogram. This gives the interferometry the multiplex advantage when it is used in spectroscopy. P. B. Fellgett first pointed this out in 1952 [188]; however, Fourier transform spectrometers did not receive much attention until the late 1960s, thanks to the development of more powerful digital electronic computers and the discovery of the so-called Fast Fourier Transform (FFT) algorithm [185].

In Fig.1.15, we show the schematic of a Fourier transform spectrometer based on a Michelson interferometer [190]. The test light is split by a beam splitter and reflected by two mirrors. The position of one mirror is fixed, and the other mirror is mechanically moved along the normal direction of the mirror to achieve the scan. Thus, a time-varying interferogram is produced, and is detected by a photodetector. The spectrum of the test light can be then reconstructed by applying a Fourier transform algorithm to the interferogram. In contrast to the grating-based spectrometer which uses a narrow slit to confine its spectral resolution, Fourier transform spectrometers can accept all the radiant energy of the incoming light without much losses, thus resulting in a higher etendue (so-called *etendue advantage*) [186]. Moreover, grating-based spectrometers divide the whole measuring range into many small "spectral bins" and measure each spectral bin separately. Therefore, the measurement time for each bin can be calculated by dividing the total measurement time by the number of the bins. On the other hand, Fourier transform spectrometers simultaneously acquire all the spectral components using a multiplex encoding technique. Therefore, if a Fourier transform spectrometer spends the same time in spectral acquisitions as a grating-based spectrometer does, the signal-to-noise ratio of the former would be higher than that of the latter (so-called *multiplex advantage*) [186]. On the negative side, Fourier transform spectrometers do not measure a spectrum directly, but have to compute the spectrum from the interferograms using a Fourier transform algorithm. Besides, for some Fourier transform spectrometers, additional algorithms (e.g. apodization algorithms) have to be used [189, 190], which makes the computation even more complicated. Moreover, the

Fourier transform spectrometers are usually quite bulky and complicated in structure, and they are unsuitable for integration with the small-sized fiber devices.
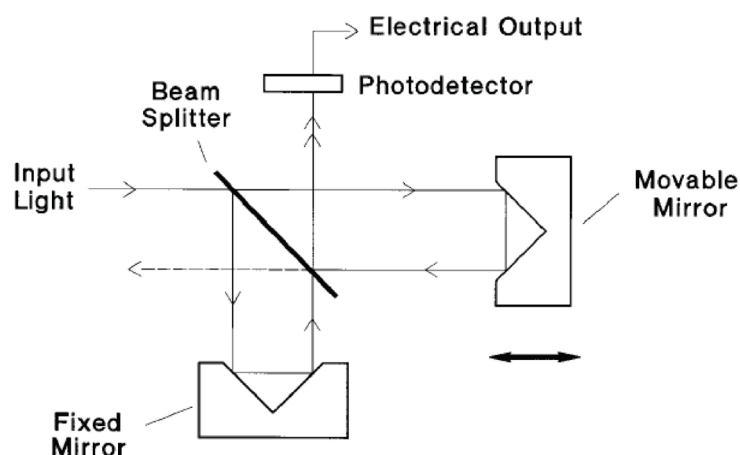
Figure 1.15   Schematic of a Fourier transform spectrometer [185].

1.4.4 Optical fiber spectrometers

Optical fibers are usually used in spectrometers as detection probes that are responsible for transferring light signals to the dispersive components (e.g. gratings or prisms) [24, 25]. The use of a fiber probe enables remote sensing of the spectrometer. Besides, a fiber probe facilitates the coupling between the spectrometer and other fiber-based transducers. We note that some special fibers (e.g. fibers with gratings or photonic crystal fibers) can provide optical dispersion, which potentially enables these fibers to realize the function of a spectrometer within the fibers. In 1985, P. St. J. Russell *et al.* [27] proposed a spectrometer based on a "grating-fiber coupler" which is fabricated by inscribing the grating on a photosensitive layer coated on top of a side-polished single-mode fiber. The grating is fabricated in the immediate vicinity of the fiber core, so that the grating interacts directly with the evanescent field of the fiber core-guided light. Along the grating, the guided optical power is gradually diffracted out of the fiber. The light with different wavelengths is diffracted at different angles, and is thus focused, by a lens, to different spatial positions on the focal plane of the lens. A linear array of photodiodes, fixed on the lens focal plane, is used to detect the spatially dispersed light. The resolution of this spectrometer was found to be ~ 1nm. In 2004, S. Wielandy and S. C. Dunn [191] demonstrated a fiber spectrometer based on a tilted fiber grating. The titled fiber grating would diffract light out of the fiber core

and produce an interference fringe pattern in near the field of the grating. Thus, the test spectrum can be reconstructed by applying a Fourier transform algorithm to this near-field interferogram. The resolution of this fiber spectrometer was on the order of sub-nanometers.

Moreover, the function of a spectrometer can also be implemented within a single piece of high-dispersion fiber. In 2006, Y. Wang *et al.* [192, 193] demonstrated this technique in which the test light is modulated by a series of narrow pulses with fixed pulse width and repetition rate to form many samples of the test light. These samples are then launched to a several-kilometer-long high-dispersion fiber to enable time-domain dispersion, and each dispersed sample provides a spectral profile similar to the spectrum of the incoming light. Finally, an optical-to-electric converter converts the light signal to the electric signal, and a high-speed data acquisition device samples and digitizes the signal and then sends the data to a computer for spectrum reconstruction. A moderate resolution of ~15 nm was experimentally demonstrated. H. Imani *et al.* [194] theoretically proposed that resolution of the spectrometer based on this technique can be improved to the picometer scale, when a low-loss high-dispersion photonic crystal fiber is used. Note that the fiber spectrometer based on this technique usually requires a several-kilometer-long high-dispersion fiber to provide sufficient time-domain dispersion.

In 2010, we proposed and experimentally demonstrated a fiber spectrometer based a solid-core photonic bandgap Bragg fiber bundle [26], which is also the project that we will demonstrate in this thesis. The fiber bundle spectrometer consists of ~100 solid-core Bragg fibers and a monochrome CCD camera. This spectrometer operates by launching the test light into the Bragg fiber bundle, and then recording the intensity image at the fiber bundle output facet using the CCD camera. The test spectrum can be reconstructed by interrogating the intensities of the individual Bragg fibers, and then by applying a deconvolution algorithm to these intensities with a "transmission matrix" method. Though only a medium resolution of the spectrometer is found (~30 nm), we believe that this spectrometer can find its niche applications due to the advantages of simple structure, the lack of moving parts, parallel acquisition of all spectral components, and the ease of integration with other fiber-optic devices. In 2012, a research group in Yale University [29] used this "transmission matrix algorithm" to develop another fiber spectrometer using a conventional 1 m long multimode fiber. By interrogating the intensity distribution (so-called speckle pattern in Ref. [29]) on the output facet of the multimode fiber, the test spectrum can be reconstructed using the transmission matrix method. The resolution of this fiber

spectrometer is 0.15 nm over a 25 nm measuring range. Based on the discussion above, we note that fiber-based spectrometers potentially can be made into low-cost, compact, fast spectroscopic devices which are promising to integrate with other fiber transducers in order to realize all-fiber optical sensors.

CHAPTER 2   METHODOLOGY

In this chapter, we summarize the two popular sensing modalities used by the fiber-based sensors, which are the amplitude-based detection modality and the spectral based detection modality. Presentation of this chapter follows closely the contents of the review paper [4] of Prof. Maksim Skorobogatiy. In the amplitude-based detection modality, one operates at a fixed wavelength λ and records changes in the amplitude of a signal, which are then re-interpreted in terms of changes in the analyte refractive index. To characterize sensitivity of a fiber-based sensor of length L, one employs an amplitude sensitivity function $S_a(\lambda, L)$, which is defined as a relative change in the intensity $P(\delta, \lambda, L)$ of a transmitted light for small changes in the measurand δ. Note that δ can be any parameter that influences transmission properties of a fiber sensor. This includes concentration of absorbing particles in the analyte, thickness of a bio-layer that can change due to capture of specific biomolecules, as well as real or imaginary parts of the analyte refractive index. Amplitude sensitivity is then defined as

$$S_a(\lambda, L) = \lim_{\delta \to 0} \frac{P(\delta, \lambda, L) - P(0, \lambda, L)}{\delta \cdot P(0, \lambda, L)} = \frac{\partial P(\delta, \lambda, L)/\partial \delta \big|_{\delta=0}}{P(0, \lambda, L)}. \qquad (2.1)$$

Denoting, $\alpha(\delta, \lambda)$ to be the fiber propagation loss at a fixed value δ of a measurand, light intensity at the fiber output can be written as

$$P(\delta, \lambda, L) = P_{in}(\lambda) \exp(-\alpha(\delta, \lambda) L), \qquad (2.2)$$

where $P_{in}(\lambda)$ is the light intensity launched into a fiber. Substituting Eq. (2.2) into Eq. (2.1), amplitude sensitivity function can be then expressed as

$$S_a(\lambda, L) = -\partial \alpha(\delta, \lambda)/\partial \delta \big|_{\delta=0} \cdot L. \qquad (2.3)$$

As follows from Eq. (2.3), sensor sensitivity is proportional to the sensor length L. In turn, as follows from Eq. (2.2), the maximal sensor length is limited by the absorption loss of a fiber. Defining $P_{det}(\lambda)$ to be the lower power detection limit at which changes in the light intensity can still be detected reliably, the maximal sensor length allowed by the power detection limit can be calculated from Eq. (2.2) as

$$L = \frac{\log(P_{in}(\lambda)/P_{det}(\lambda))}{\alpha(0,\lambda)}. \tag{2.4}$$

Defining $\eta_{det}(\lambda) = \log(P_{in}(\lambda)/P_{det}(\lambda))$, maximal sensitivity allowed by the power detection limit can be written using Eq. (2.3) as

$$S_a(\lambda) = -\eta_{det}(\lambda)\frac{\partial\alpha(\delta,\lambda)/\partial\delta|_{\delta=0}}{\alpha(0,\lambda)}. \tag{2.5}$$

In all the simulations that follow, we assume that $\eta_{det}(\lambda) = 1$, which allows us to characterize an inherent sensitivity of a sensor system, while separating it from the issue of a power budget that might bring additional sensitivity enhancement. Finally, given sensor amplitude sensitivity, to estimate sensor resolution of a measurand, δ, one can use Eq. (2.1). Assuming that the minimal detectable relative change in the signal amplitude is $(\Delta P/P)_{min}$ (which is typically on the order of 1% if no advanced electronics such as lock-in amplifiers is used), then the minimum value of a measurand that can be detected by such a sensor is

$$\delta_{min} = \frac{(\Delta P/P)_{min}}{S_a(\lambda)}. \tag{2.6}$$

Another popular sensing modality is spectral-based. It uses detection of displacements of spectral peaks in the presence of a measurand with respect to their positions for a zero level of a measurand. This sensing approach is particularly effective in the resonant sensor configurations that feature sharp transmission or absorption peaks in their spectra. Variations in a measurand could be characterized from changes in positions of the transmission or absorption peaks. Defining $\lambda_p(\delta)$ to be the position of a peak in a sensor transmission spectrum as a function of a measurand value δ, spectral sensitivity function can be defined as

$$S_\lambda = \partial\lambda(\delta)/\partial\delta|_{\delta=0}. \tag{2.7}$$

Given sensor spectral sensitivity, to estimate sensor resolution of a measurand δ, one can use Eq. (2.7). Thus, assuming that the minimal detectable spectral shift in the peak position is $(\Delta\lambda_p)_{min}$ ($(\Delta\lambda_p)_{min}$ is typically on the order of 0.1 nm, which is the typical resolution of a high-

end grating spectrometer), then the minimum value of a measurand that can be detected by such a sensor is

$$\delta_{min} = \frac{\left(\Delta\lambda_p\right)_{min}}{S_\lambda}.$$ (2.8)

For the liquid-core Bragg fiber refractometer demonstrated in this thesis, both of the sensing modalities can be utilized. However, when this Bragg fiber refractometer operates in the amplitude-based detection modality, its signal is negatively affected by many factors such as intensity fluctuations of the light source, changes in mechanical alignment due to analyte loading or removal, bending of the fiber, micro-particles or air bubbles suspended inside the liquid analytes. All these factors would degrade the detection accuracy and repeatability of the fiber refractometer. In contrast, the spectral based detection modality is virtually immune to the influence of these factors, since in this case the measurand is a spectral position of the transmission peak that corresponds to the bandgap of the Bragg fiber, as this measurand is mostly determined by the value of the refractive index of the Bragg fiber core.
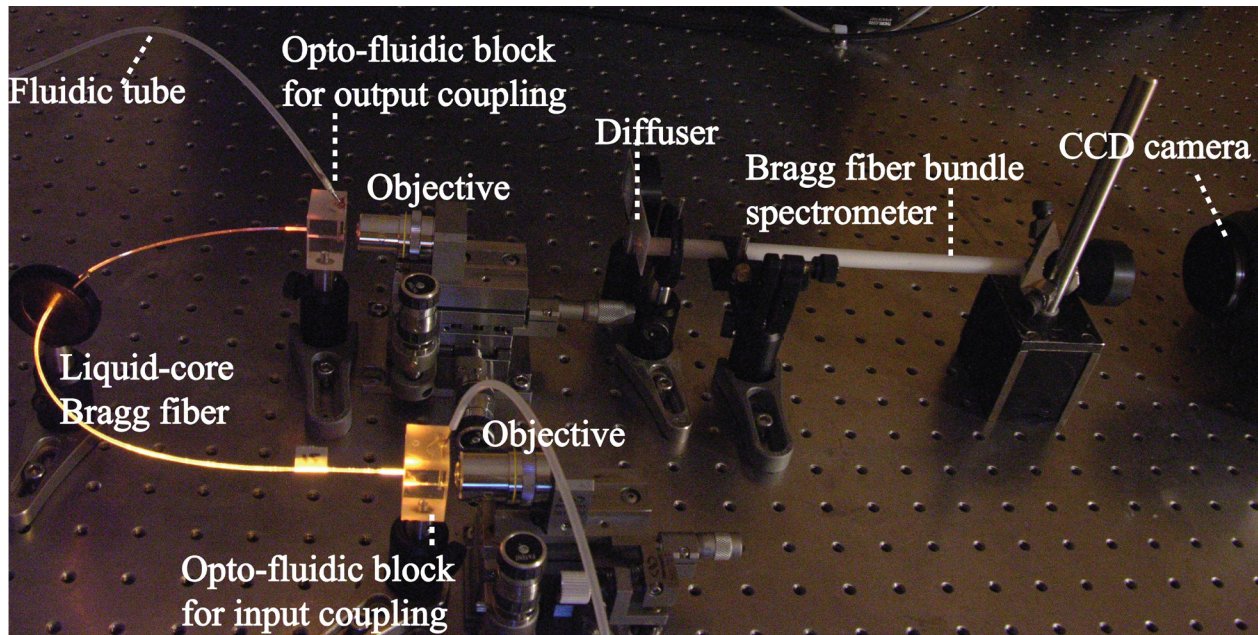
Figure 2.1   Experimental setup of the liquid-core Bragg fiber refractometer demonstrated in this thesis

In Fig.2.1, we show the experimental setup of the Bragg fiber refractometer system demonstrated in this thesis. The system can be sub-divided into two parts: the hollow-core Bragg

fiber for holding and probing liquid analytes filling the fiber core (detailed in Chapter 3), and the solid-core Bragg fiber bundle spectrometer for spectral acquisition (detailed in Chapter 4). The methodology and experimental details for the integration of the two parts are detailed in Chapter 5.

The following presentation is largely based on the content of several articles that I have published during my doctorate studies. Additionally, I will discuss many of the experimental challenges and experimental details, which were not covered in the original papers.

CHAPTER 3   ARTICLE 1: LIQUID-CORE LOW-REFRACTIVE-INDEX-CONTRAST BRAGG FIBER SENSOR

3.1   Introduction

In this chapter we propose and demonstrate a fiber refractometer based on a special type of the MOF, i.e., hollow-core low-refractive-index-contrast photonic bandgap Bragg fiber (Fig.3.1). The sensor operates on a resonant sensing principle, in which variations in the "bulk" refractive index of a liquid analyte filling the Bragg fiber core modify the resonant guidance of the Bragg fiber, thus leading to both intensity changes and spectral shifts in the fiber transmission [153]. Both theoretical simulations and experimental characterizations are performed in order to characterize the proposed fiber sensor. The experimental sensitivity of this sensor is found to be ~1400 nm/RIU. The high "bulk" sensitivity of our sensor is due to two factors. One is an almost perfect overlap between the analyte and the optical modes of a Bragg fiber, while another one is a resonant nature of the photonic bandgap guidance mechanism. In what follows, we also detail many of the performance characteristics of the fiber refractometer, such as repeatability, measuring range, insertion loss, and the relationship between the fiber length and sensitivity. Additionally, we study "surface" sensing modality by detecting changes in the thickness of a thin layer deposited directly on the inner surface of the fiber hollow core. Because of the low overlap between the analyte layer and the optical field guided in the fiber, only a modest sensitivity (~0.9 nm/μm) is obtained with this sensing modality.

3.2   Principle of operation of liquid-core Bragg fiber sensor

The all-polymer hollow-core low-refractive-index-contrast Bragg fibers used in our sensors were fabricated in-house using the fiber drawing technique. The Bragg fibers feature a large air core (diameter: 0.4-1 mm) surrounded by an alternating polymethyl methacrylate (PMMA)/polystyrene (PS) Bragg reflector (refractive index: 1.487/1.581 @ 589 nm) followed by a PMMA cladding (Fig.3.1 (b)). The large core of a Bragg fiber facilitates filling it with aqueous solutions, which might contain biological or chemical reagents. Such a large core also leads to a short response time of a sensor, since the flow resistance of the core decreases polynomially with

increasing core radius [22]. Experimentally, the response time of a 40 cm long sensor is found to be ~1 s.
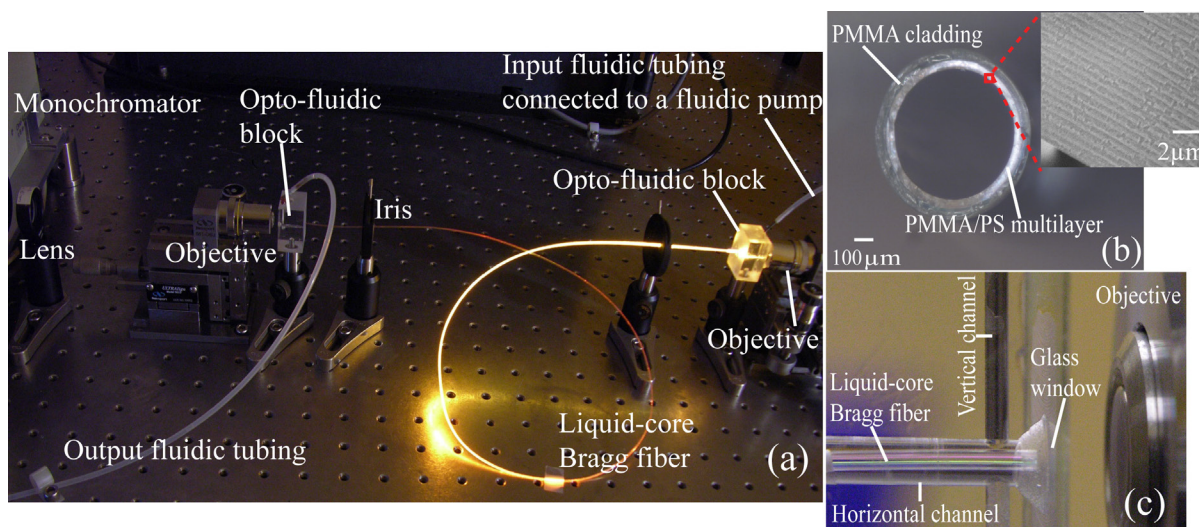
Figure 3.1   (a) Setup of the Bragg fiber sensor system. An ~80 cm long liquid-core Bragg fiber, coiled into a ~15 cm diameter circle, is integrated into a setup using two opto-fluidic coupling blocks. The beam from a supercontinuum source is coupled into the liquid-core Bragg fiber, and the transmission spectrum of a liquid-core Bragg fiber is then analyzed using a grating monochromator. (b) Cross section of a hollow-core Bragg fiber; the inset is the graph of the Bragg reflector taken by a scanning electron microscope (SEM). (c) Inner structure of the opto-fluidic block. A tip of a liquid-core Bragg fiber is sealed into the horizontal channel of the coupling block filled with the liquid analyte. The extremity of the horizontal channel is sealed by a glass window through which light is coupled into (or out of) the sensing system. In each coupling block there is also a vertical channel that connects to the horizontal channel to constitute the fluidic path for fluidic coupling of the Bragg fiber. The colorful appearance of the Bragg fiber is due to reflection of ambient light from the Bragg reflector.

The guiding and sensing properties of the low-refractive-index-contrast Bragg fiber can be elucidated from the Bragg reflector band diagram (frequency versus propagation constant). In Fig.3.2, we show the band diagram of the TE (transverse electric) and the TM (transverse magnetic) polarized modes propagating inside of an infinite planar Bragg reflector made from PMMA/PS multilayers. Due to the large diameter of the Bragg fiber, the band diagram of the Bragg reflector in a fiber could be considered analogous to that of the planar Bragg reflector. This band diagram is calculated by performing the Bloch wave analysis in the Bragg reflector with the

plane wave expansion method [195]. Note that the planar Bragg reflector has different band gaps for TE and TM polarizations, referring to fields purely parallel to the planar interface and fields with a normal component, respectively. To compute this band diagram, we use the values of the refractive indices of the PMMA and PS films measured by a VASE Ellipsometer (J. A. Woollam Co., Inc.). The average thicknesses of the individual PMMA and PS layers are 0.37 μm and 0.13 μm, respectively, estimated from the SEM graph (Fig.3.1 (b)). Grey regions in Fig.3.2 indicate states delocalized over the whole Bragg reflector. Such states are efficiently irradiated out of the fiber due to scattering on the imperfections in the reflector multilayer. Clear regions (bandgaps) define the parts of the phase space where light is unable to propagate inside of the Bragg reflector. The black thick curves represent the light line of the liquid analyte, i.e., distilled water. Modes guided in the hollow core will have effective refractive indices close to, while somewhat smaller than that of water (black thick curves in Fig. 3.2). Therefore, a mode confined in the liquid core will exist in the regions of a band diagram where light line of water intersects the reflector bandgap (horizontal green regions in Fig.3.2)

$d_l = 0.37\mu m$; $d_h = 0.13\mu m$; $n_l = n_{pmma}$; $n_h = n_{ps}$;
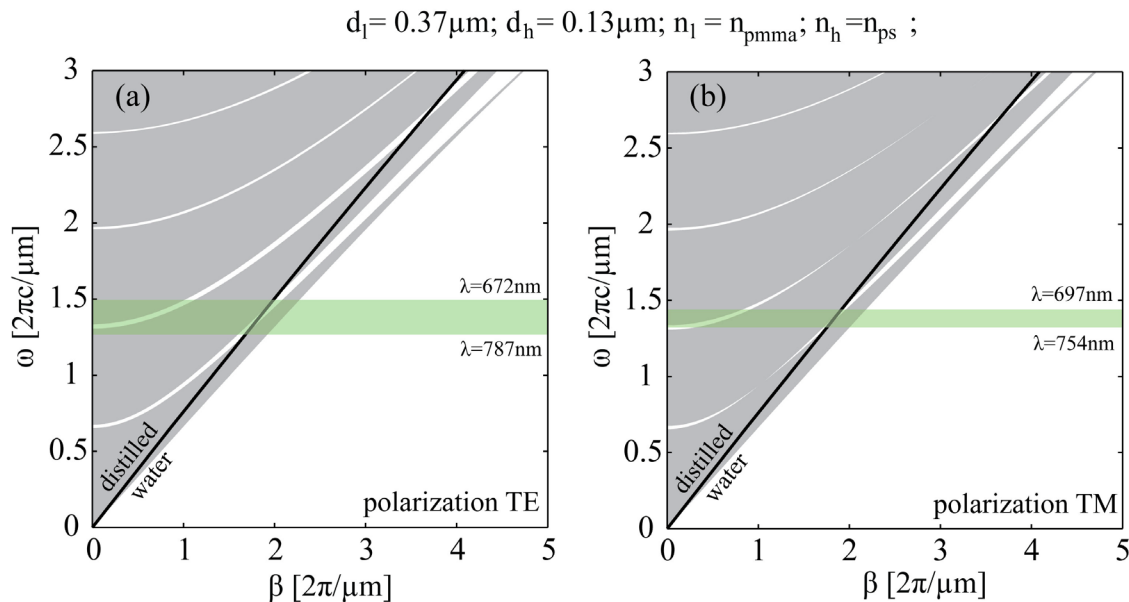
Figure 3.2   Band diagram of (a) the TE and (b) the TM polarized modes of a PMMA/PS Bragg reflector. The grey regions correspond to (β, ω) for which light can propagate within the Bragg reflector. The clear regions correspond to the parts of the phase space where light is unable to propagate in the Bragg reflector. Thick black curves represent the light line of distilled water.

Transmission bands (green) of the Bragg fiber can be estimated from the intersection of light line of water with the Bragg reflector bandgaps.

From the basic theory [4, 153] of low-refractive-index-contrast Bragg fibers, the center wavelength, λ_c, of the fundamental reflector bandgap can be approximately calculated as

$$\lambda_c/2 = d_h(n_h^2 - n_c^2)^{1/2} + d_l(n_l^2 - n_c^2)^{1/2}, \tag{3.1}$$

where d_l, d_h are the thicknesses of the low- and high- index layer in the Bragg reflector, respectively; n_l, n_h are the refractive indices of the corresponding layers; n_c is the refractive index of the core material. Variations in the refractive index of an analyte filling the fiber core could modify the resonant condition (Eq. (3.1)) of the Bragg fiber, thus resulting in spectral shifts of the resonant wavelength in the fiber transmission, which constitutes the main sensing principle of the Bragg fiber sensor.

We note that low-refractive-index-contrast Bragg fibers have certain advantages for liquid analyte sensing compared to their high-refractive-index-contrast counterparts. Previously, high-refractive-index-contrast Bragg fibers have been used for sensing of gas analytes ($n_{analyte}$ ~1) [196], as well as liquid analytes with high refractive indices ($n_{analyte}$ >1.40) [152]. However, for the high-refractive-index-contrast Bragg fibers used in these works, the TM bandgaps of the Bragg reflector tend to collapse near the light line of the aqueous material ($n_{analyte}$ ~1.33) due to the Brewster angle phenomenon, thus leading to high loss for the hybrid (HE/EH) modes propagating in the fiber liquid core. In contrast, low-refractive-index-contrast Bragg fibers show large TM bandgaps in the vicinity of the light line of water, thus resulting in good guidance of HE/EH modes (Fig.3.2). Moreover, we note that low-refractive-index-contrast Bragg fibers are more sensitive to changes in the refractive index of a liquid analyte filling the fiber core, as compared to their high-refractive-index-contrast counterparts. Particularly, from Eq. (3.1), we derive the sensitivity of the sensor, S, as

$$S = \frac{d\lambda_c}{dn_c} = 2[d_h(\frac{n_h^2}{n_c^2} - 1)^{-1/2} + d_l(\frac{n_l^2}{n_c^2} - 1)^{-1/2}]. \tag{3.2}$$

According to Eq. (3.2), the closer is the value of the core index to those of the individual layers of the Bragg reflector; the more sensitive the Bragg fiber sensor will be to variations in the

refractive index of the analyte-filled core, which is exactly the case for our low-refractive-index-contrast Bragg fiber sensor.

3.3 Theoretical and experimental characterization of the Bragg fiber sensor

To theoretically verify the resonant sensing mechanism, we simulate loss spectra of the fundamental HE_{11} mode of the liquid-core Bragg fiber based on the Transfer Matrix Method (TMM) [197]. The structural parameters of the hollow-core Bragg fiber are the same as those used in Section 3.2. For liquid analytes, we choose a set of NaCl solutions with the weight concentration ranging from 0 to 25% in 5% incremental steps. The corresponding refractive indices of NaCl solutions are shown in the inset of Fig.3.3 [198]. The bulk absorption of NaCl solutions in the spectral range of interest was shown to be virtually identical with that of pure water [199]. In our simulations, we compute the propagation loss of the HE_{11} mode taking into account absorption loss of water and dispersion of water and plastics in the Bragg reflector. The simulated loss spectra suggest that the transmission band of the liquid-core Bragg fiber shows a blue-shift as the refractive index of the liquid analyte increases (Fig.3.3 (a)).
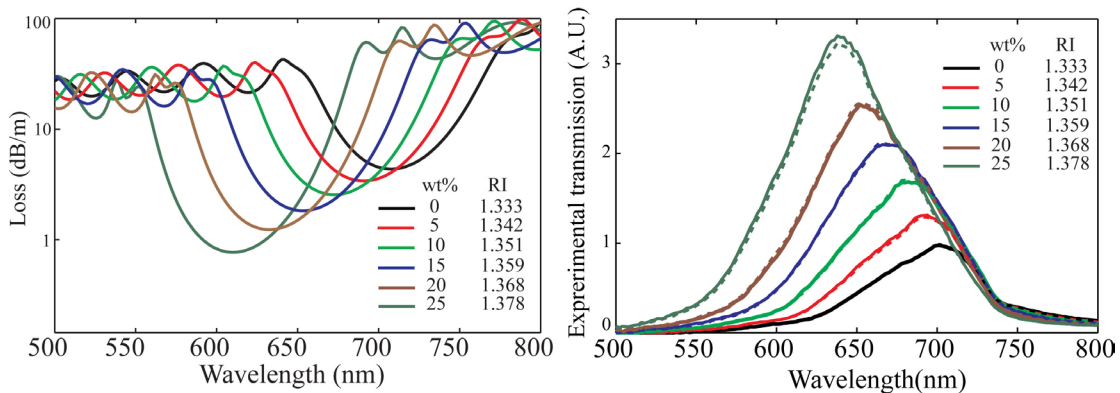
Figure 3.3   (a) Simulated loss of the fundamental mode (HE_{11} mode) of the Bragg fiber filled with different NaCl solutions. (b) Experimental transmission spectra of a ~40 cm long Bragg fiber filled with NaCl solutions (solid curves). The dotted curves indicate a repeat of the first experiment after several hours, which demonstrate a good repeatability of the measurement. The weight concentrations (wt%) and corresponding refractive indices of the NaCl solutions are listed in both figures as insets.

In our experiments, we employ two opto-fluidic blocks designed to simultaneously enable optical and fluidic coupling of the hollow-core Bragg fiber (Fig.3.1 (c)). A ~40 cm long Bragg

fiber, coiled into a 10 cm diameter circle, is integrated into the sensing system. On each side, the hollow-core Bragg fiber tip is inserted hermetically into the analyte-filled horizontal channel that has a thin glass window attached at the one of its extremities for optical coupling of the Bragg fiber (Fig.3.1 (c)). In each block there is also a vertical channel which connects to the horizontal channel to constitute the fluidic path for fluidic coupling of the Bragg fiber. This design avoids formation of air bubbles in the sensing system, which would strongly suppress fiber transmission. After pumping a liquid analyte into the fiber, we couple the beam from a supercontinuum source into the fiber using a 10× objective, and the transmission spectrum of the liquid-core Bragg fiber is then analyzed by the Oriel grating monochromator (Newport Inc.). To verify the repeatability of the sensor, we repeat the same experiment after 3 h by first purging the setup with distilled water. Fig.3.3 (b) shows the results of two consecutive experiments. The solid curve represents the transmission spectra of the first measurement, and it compares well with the results of the second measurement shown as the dotted curve. In the two measurements, we observe no more than 2.51% fluctuation in the detected intensity, while the center position of the transmission peak stays at the same position up to the resolution limit (~1 nm) of our spectrometer. As seen in Fig.3.3 (b), the experimental transmission spectrum also shows a blue-shift, as the refractive index of the fiber core increases. Moreover, the spectral shifts of the transmission peak have a linear dependence on the increasing refractive index of the fiber core (see Fig.3.4).
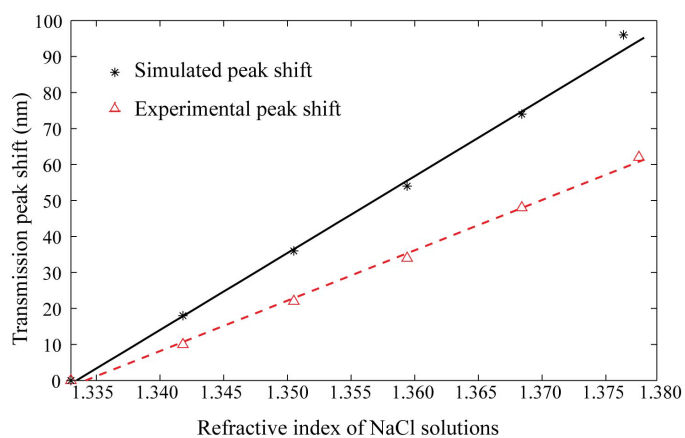
Figure 3.4   Spectral shifts of the fiber transmission peak obtained from the TMM simulation (black solid line) and the experimental measurements (red dash line)

We note that the experimental spectral shifts of the fiber transmission peak are somewhat smaller than the simulated ones. This is likely due to the fact that, in our simulation, we only

calculate the spectral shifts of the fundamental HE_{11} mode with its effective refractive index virtually identical to that of the liquid analyte filling the core. Nevertheless, most of higher-order core modes have effective refractive indices (n_{eff}) lower than that of the HE_{11} mode. Therefore, by substitution of n_c by n_{eff} in Eq. (3.2), we arrive to the conclusion that the spectral shifts of the transmission peaks of higher-order modes are smaller than those of the HE_{11} mode. Due to the large diameter of the Bragg fiber core used in the experiments, many higher-order modes are excited. As these high-order modes are less sensitive than the HE_{11} mode, the experimental spectral shifts are, therefore, smaller than those of the HE_{11} mode. Finally, from Fig.3.4 we conclude that the experimental sensitivity of the liquid-core Bragg fiber sensor is ~1400 nm/RIU. Assuming that a spectral shift of 0.1 nm can be reliably detected, this sensitivity is equivalent to a sensor resolution of ~7×10^{-5} RIU. Such a sensitivity is comparable to those of the MOF-based sensors [147-149, 155-157, 161, 162], but is an order smaller than that of the dual-core MOF sensor with a sensitivity of ~30000 nm/RIU [150]. However, we note that the dual-core MOF sensor is limited to sensing of liquid analytes with $n_{analyte}>n_{silica}$. In addition, compared to other MOF-based sensors, our Bragg fiber sensor is advantageous in terms of its short response time (~1 s) due to the large core of the Bragg fiber.

3. 4 Discussion of factors influencing sensor performance

3.4.1 Dynamic range of the sensor

The operating frequency range of this sensor is mainly determined by the position of the Bragg reflector bandgap. Currently, we routinely produce Bragg fibers with primary bandgaps located in the 500-800 nm spectral range; therefore, all our experiments are conducted in this range. Sensitivity of the sensor is so high that by varying the liquid-core refractive index from 1.333 to 1.378, the fiber bandgap already spans this whole operational window (see Fig.3.3). From the band diagram in Fig.3.2, it follows that the largest wavelength of operation is $\lambda \sim 1300$ nm. That is the region where sensing of low-refractive-index analytes with $n_{eff} \sim 0$ can be achieved. In application to aqueous analytes, the bulk absorption is generally larger than 50 dB/m at the wavelength above 1 μm, thus limiting the operation range of the sensor in the near-infrared range. Finally, for the high-refractive-index analytes, the fiber bandgap will shift into the blue spectral

region; however, there is no fundamental limit for the use of these sensors for high-refractive-index analytes.

3.4.2 Insertion and coupling loss

Due to the large diameter of the Bragg fiber core (over 0.5 mm), coupling efficiency of the fiber is superb (above 90%), which is one of the well-known advantages of such fibers. Main coupling loss of the sensor comes from the reflection between the air and the glass window covering the fluidic channel (Fig.3.1 (c)). The total coupling and out-coupling loss is estimated to be ~10%.

3.4.3 Dependence of sensitivity on fiber length

To study the dependence of the sensitivity on the length of a Bragg fiber, we first measure the spectral shifts of a 50 cm long Bragg fiber filled with NaCl solutions with different concentrations. Then, we cut the fiber into 30 cm and 20 cm, and for each length we repeat the experiment to measure the spectral shifts in response to variations in the refractive index of the liquid core of the Bragg fiber. In Fig.3.5, we plot fiber transmission spectra of the liquid-core Bragg fiber with different lengths.

The transmission spectra of the 50 cm long Bragg fiber show clear spectral shifts caused by variations in the refractive index of the fiber core (Fig.3.5 (a)). The sensitivity of the 50 cm long fiber sensor is ~1300 nm/RIU, which is estimated from the spectral shifts of the specific transmission peak marked by white arrows. In the transmission spectra of the 30 cm long Bragg fiber, we still observe the spectral shifts of the transmission peak (Fig.3.5 (b)); however, the transmission spectra become broader due to reduced fiber attenuation at the bandgap edges because of a shorter fiber length. The experimental sensitivity of the 30 cm long Bragg fiber sensor is ~1270 nm/RIU (Fig.3.5 (d)). Further reduction of the Bragg fiber length to 20 cm leads to even smaller propagation losses at all frequencies. However, the reduced fiber loss causes the difficulty in differentiating specific resonant features in the fiber transmission spectra, and as a result it becomes difficult to detect spectral shifts.

Therefore, we conclude that the liquid-core Bragg fiber should have a minimal (threshold) length to ensure sufficient attenuation at the wavelengths in the vicinity of bandgap edges in order to allow the formation of spectral features (such as transmission peaks) in the fiber transmission. We experimentally find the threshold length to be ~10 cm for most Bragg fibers

used in our experiments. Once the fiber length is longer than the threshold value, the sensitivity of a Bragg fiber sensor does not strongly depends on the fiber length, which is consistent with the prediction in Ref. [4]. A longer fiber also leads to a stronger attenuation of the higher-order modes, thus acting as a high-order mode striper, which is also beneficial for sensing. At the same time, signal strength in longer fibers decreases due to increased material absorption and radiation losses, eventually leading to signal-to-noise degradation, which is disadvantageous for sensing. It is the trade-off between the two above-mentioned factors that determines the optimal fiber length. Note that the optimization of the sensing length is not strictly required for sensing applications. Experimentally, we find the maximal sensing length of a Bragg fiber to be ~1 m. With the sensing length smaller than ~1 m, one can always measure the transmission spectrum of a Bragg fiber without much signal-to-noise degradation. Therefore, when sensing a specific liquid analyte, one, in practice, could choose a Bragg fiber with any length between the threshold value (~10 cm) and the maximal length (~1 m).
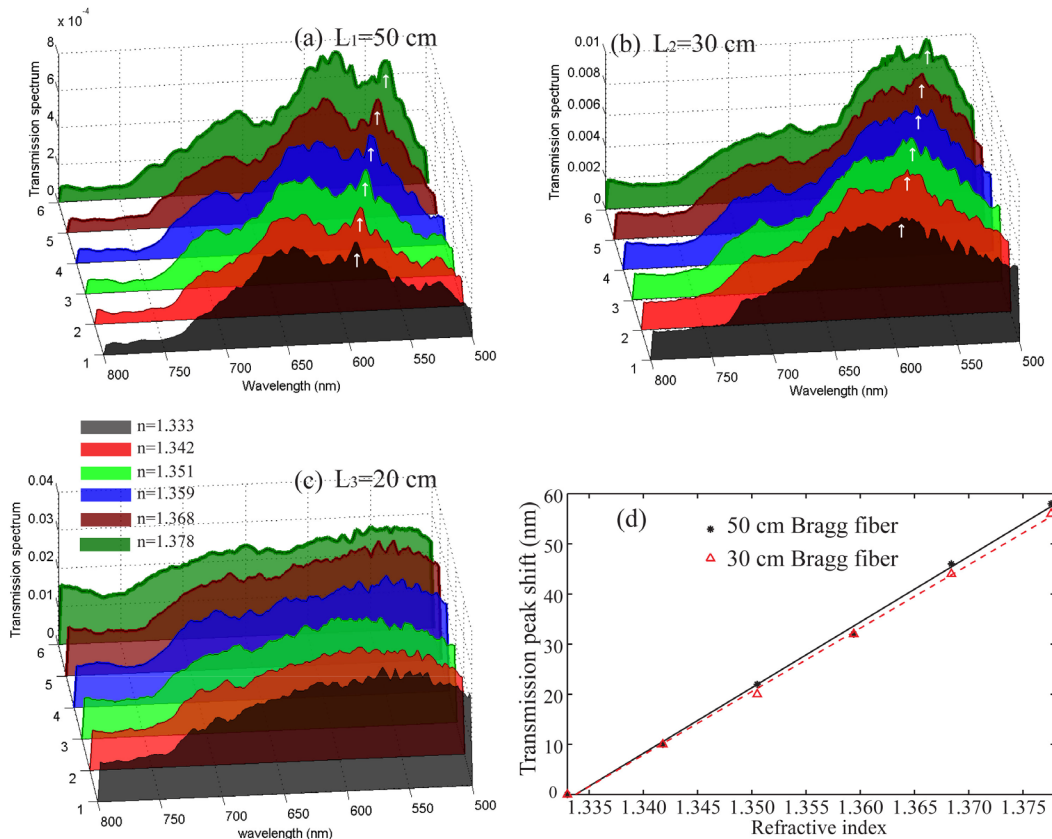
Figure 3.5   Transmission spectra of the liquid-core Bragg fiber with different lengths: (a) 50 cm; (b) 30 cm; (c) 20 cm. The refractive indices of the analytes filling the fiber core are listed in

as inset of (c). The white arrows in (a) and (b) mark the resonant peak positions, which we use to measure the spectral shifts. A linear dependence of the spectral shifts on changes in the refractive index of the fiber core is shown in (d). The black solid line represents the spectral shifts of a 50 cm long Bragg fiber and the red dashed line represents the spectral shifts of a 30 cm long Bragg fiber.

3.5 Bragg fiber sensor operating in the surface sensing modality

Another application of this Bragg fiber sensor operating on the resonant sensing modality is to detect changes in the thickness of a thin layer deposited directly on the inner surface of the fiber core. By coating a thin layer, the localized refractive index in the vicinity of the fiber inner surface would change substantially, which then modifies the resonant guidance of the Bragg fiber and leads to a spectral shift of the resonant wavelength in the fiber transmission. We take the thickness of the coated layer, d_a, as the measurand. Therefore, according to Eq. (2.7), we could define the sensitivity of the Bragg fiber sensor to changes in the thickness of the coated layer as $S = \partial \lambda_c / \partial d_a$. We note that due to the large core of the Bragg fiber, only a small fraction of core-guided modes can be found in the vicinity of the fiber inner surface, thus leading to a poor modal overlap with the analyte layer. Consequently, we expect the sensitivity in the surface sensing modality to be quite moderate.

(a)   (b)
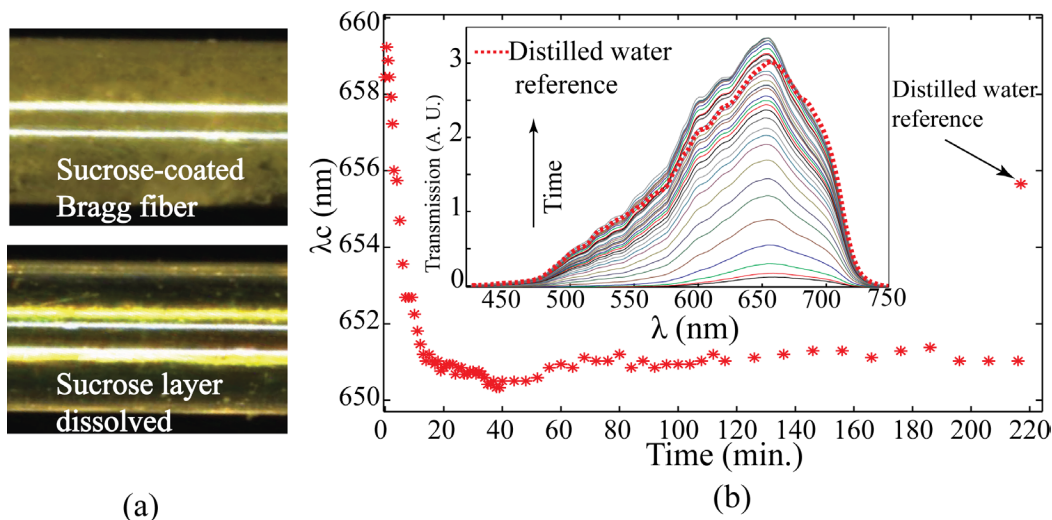
Figure 3.6   (a) Top: appearance of the Bragg fiber coated with a sucrose layer; Bottom: appearance of the Bragg fiber with the coated layer dissolved in the liquid core. (b) Time-dependent spectral changes in the fiber transmission during the dissolution of the thin sucrose

layer coated on the inner surface of the fiber core. At t=0, the fiber core is dry; the sucrose layer is 3.8 μm thick. Then, distilled water is quickly introduced. In the first 20 minutes, rapid changes in the transmission intensity and peak position are detected. After several hours, the reference is measured by purging the fiber with distilled water.

To study the surface sensing modality of a Bragg fiber sensor, we first coat a ~3.8 μm thick sucrose layer on the inner surface of a 15 cm long Bragg fiber (from the same preform with the fiber used above). Particularly, a 60 wt% sucrose solution is filled into the Bragg fiber core. Then the fiber is placed in an oven for 6 h in order to make the sucrose solution more viscous. Subsequently, an air pump is used to blow off most of the sucrose syrup in the fiber core while leaving a thin sucrose layer behind (Fig.3.6 (a)). The fiber is then dried again.

For the optical measurements, we first insert the dry sucrose-coated Bragg fiber into the sensing setup and then quickly (~1 s) fill the fiber with distilled water. As the sucrose layer gradually dissolves in water, the bulk refractive index of the fiber core gradually increases. The transmission spectra (Fig.3.6 (b)) of the fiber are acquired throughout the dissolution process. Fig.3.6 shows that the transmission spectrum shifts ~8.2 nm towards shorter wavelengths in the first 20 minutes after filling the fiber with distilled water. During this period, the spectral shift is mostly due to the increase of the bulk refractive index of the fiber core caused by the dissolution of the sucrose layer. No significant spectral shift appears after 20 minutes, which indicates that most of the sucrose layer is dissolved. In contrast, the transmitted intensity still keeps slowly increasing during the several hours that follow. Visual inspection of the fiber under a microscope indicates that increase of the signal amplitude is probably due to reduction of the scattering losses incurred by the fiber mode on small chunks of the undissolved sucrose. Finally, when fiber transmission spectrum stops changing (complete dissolution of the sucrose layer), we refill the fiber with distilled water. Consequently, the peak of the transmission spectrum shifts to 655.7 nm. Comparison with the initial peak position, which is measured almost instantaneously after filling the sucrose-coated fiber with water, allows us to conclude that the presence of a 3.8 μm thick sucrose layer leads to a 3.5 nm red-shift of the transmission spectrum of a water-filled fiber, compared to that of a water-filled fiber without a sucrose layer. The corresponding surface sensitivity of our sensor to changes in the sucrose layer thickness is then estimated to be ~0.9 nm/μm. Note that the sensitivity for the surface sensing, in principle, is also strongly independent

on the length of the fiber; however, the maximal sensing length is experimentally found to be ~20 cm due to the large scattering loss caused by the sucrose layer.

3.6 Conclusions

In this chapter, we have proposed and experimentally demonstrated a liquid-core low-refractive-index-contrast Bragg fiber sensor which can be used for detection of changes in the "bulk" refractive index of liquid analytes filling the fiber core. This Bragg fiber sensor operates on a resonant sensing mechanism, according to which the transmission peak of the Bragg fiber shifts as a function of the refractive index of a liquid analyte filling the fiber core. Both numerical simulations and experiments are carried out to verify the operating principle of the proposed sensor. Besides, we also comprehensively study the factors that affect the performance of the sensor. We experimentally find that the sensitivity of the sensor is as high as ~1400 nm/RIU, which is comparable to other MOF refractometers. The proposed liquid-core Bragg fiber sensor constitutes a one-fiber solution for refractive-index sensing with the advantages of simplicity in sensing mechanism, large core, short response time, ease of fabrication, and high sensitivity. Moreover, we demonstrate the operation of the Bragg fiber sensor in a surface sensing modality to detect changes in the thickness of an analyte layer deposited on the inner surface of a Bragg fiber. Only a moderate surface sensitivity of ~0.9 nm/µm is found due to the poor overlap of core guided modes to the deposited thin layer.

CHAPTER 4   ARTICLE 2: PHOTONIC BANDGAP FIBER BUNDLE SPECTROMETER

4.1 Introduction

In this chapter, we propose and experimentally demonstrate an all-fiber spectrometer that consists of a solid-core Bragg fiber bundle and a monochrome CCD camera. ~100 solid-core Bragg fibers which have complementary and overlapping bandgaps are chosen to compose the fiber bundle. The test light filtered by the Bragg fiber bundle is converted into a single intensity image which is then registered by the CCD camera. To reconstruct the test spectrum from the CCD image, we develop an algorithm based on pseudoinversion of the spectrometer transmission matrix obtained from a calibration measurement. We demonstrate that the center wavelength of a spectral peak can always be reconstructed within several percent of its true value regardless of the peak width or position, and that although the widths of the individual Bragg fiber bandgaps are quite large (60-180 nm), the spectroscopic system has a resolution limit of ~30 nm. Moreover, we conclude that by minimizing system errors, the resolution can be further improved down to several nm in width. Finally, we report fabrication of Bragg fiber bundles containing hundreds of fibers using a two-step drawing technique. This method constitutes a very promising approach towards an industrial-strength fabrication of all-Bragg-fiber spectrometers.

4.2 Characteristics of the subcomponents: solid-core Bragg fibers, fiber bundle and a CCD camera

4.2.1 Solid-core photonic bandgap Bragg fibers

PBG Bragg fiber is a key element of our spectroscopic system. The solid-core Bragg fibers used in research are fabricated in-house, and they have been reported previously in [200]. An individual solid-core Bragg fiber features a large 300-700 μm diameter core made of a polymethyl methacrylate (PMMA) plastic. The core region is surrounded with a periodic multilayer reflector featuring ~100 submicrometer-thick layers of low- and high- refractive index PMMA/Polystyrene (PS) plastics (refractive index: 1.49/1.58@589nm). This multilayer (Bragg reflector) design is responsible for the appearance of a spectrally narrow transmission band (reflector bandgap) within which the light is strongly confined inside the fiber core. For the

wavelengths outside of the reflector bandgap, the light penetrates deeply into the multilayer region, exhibiting strong propagation loss due to scattering on the imperfections inside the multilayer region. A typical fiber loss within the reflector bandgap region is ~10 dB/m, and is mostly determined by the bulk absorption loss of a low-purity PMMA plastic. Outside of the bandgap region scattering loss (on the imperfections in the multilayer structure) dominates, resulting in >60 dB/m propagation loss. In our experiments we used 30 cm long fibers, so that the loss of guided light was below 3 dB, while the loss of non-guided light was >20 dB. The numerical aperture of all the Bragg fibers was in the range of 0.17-0.22.

To construct a fiber bundle spectrometer, we chose 100 solid-core Bragg fibers with complementary and partially overlapping bandgaps, as shown in Fig.4.1 (a). All the fibers in a bundle were drawn from the same preform with the only difference among them being the final diameter. The smaller diameter fibers feature bandgaps shifted toward the blue part of a spectrum. This is easy to rationalize from the basic theory of Bragg fibers which predicts that the bandgap center wavelength is proportional to the thickness of the multilayer in the Bragg reflector [190].
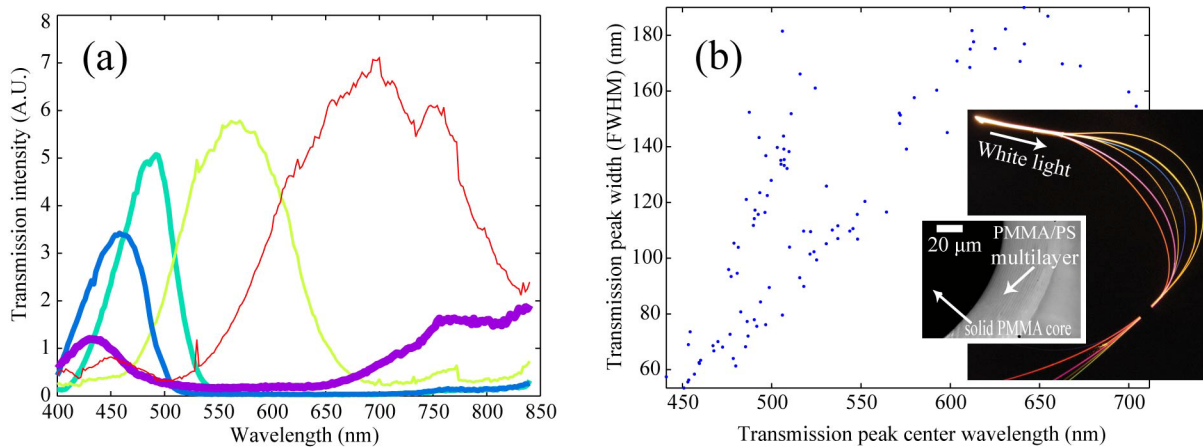
Figure 4.1   (a) Transmission spectra of 5 typical Bragg fibers used in the fiber bundle. (b) Distribution of the fiber transmission bandwidth as a function of the fiber bandgap center wavelength for all the Bragg fibers in a bundle. In the inset: photo of a Bragg fiber cross section showing a solid core surrounded by a periodic multilayer reflector.

Fig.4.1 (b) also shows the distribution of the fiber transmission bandwidth as a function of the fiber transmission central wavelength. We note that the fiber transmission bandwidth increases with its center frequency [202]. Thus, in the blue part of a spectrum, the fiber bandgap width is ~60 nm, while increasing to ~180 nm in the red part of a spectrum. There are two factors

that contribute to this phenomenon. First, from the basic theory of Bragg fibers [202] it follows that the relative width of a PBG (ratio of the bandgap size to the bandgap center frequency) is mostly a function of the refractive index contrast in the Bragg fiber reflector. As all the fibers used in this project are fabricated from the same preform, it means that the relative bandwidth is approximately constant for all the fibers; hence the absolute bandgap width should increase with the bandgap center frequency. Second, as we have mentioned in the previous paragraph, fibers featuring bandgaps at longer wavelengths have larger core size. In Bragg fibers, modal losses due to radiation and scattering on the reflector imperfections scale as $1/R^3$ with the core size [197, 202]. Therefore, larger core fibers exhibit smaller loss than smaller core fibers. Note that in Fig.4.1, we show the transmission intensities and not the actual losses. Clearly, for the fibers of the same length, smaller core fibers will exhibit spectrally narrower transmission, as wavelengths near the bandgap edge will be attenuated much more strongly than those in the larger core fibers.

4.2.2 Photonic bandgap Bragg fiber bundle

The fiber bundle used in our experiments features a 5.6 mm inner diameter plastic tube that hosted ~100 pieces of 30 cm long Bragg fibers. The fibers at the input end of a bundle are rigidly attached with epoxy to each other and to the confining tube, and the whole assembly is then polished using optical films of various granularity. On the other end of a bundle, 100 fibers are inserted into a custom-made block featuring holes of diameter 0.8 mm placed in a periodic 10×10 square array (see Fig.4.2). The block, the tube, and all the fibers are bonded together with epoxy, and the output end is then polished.
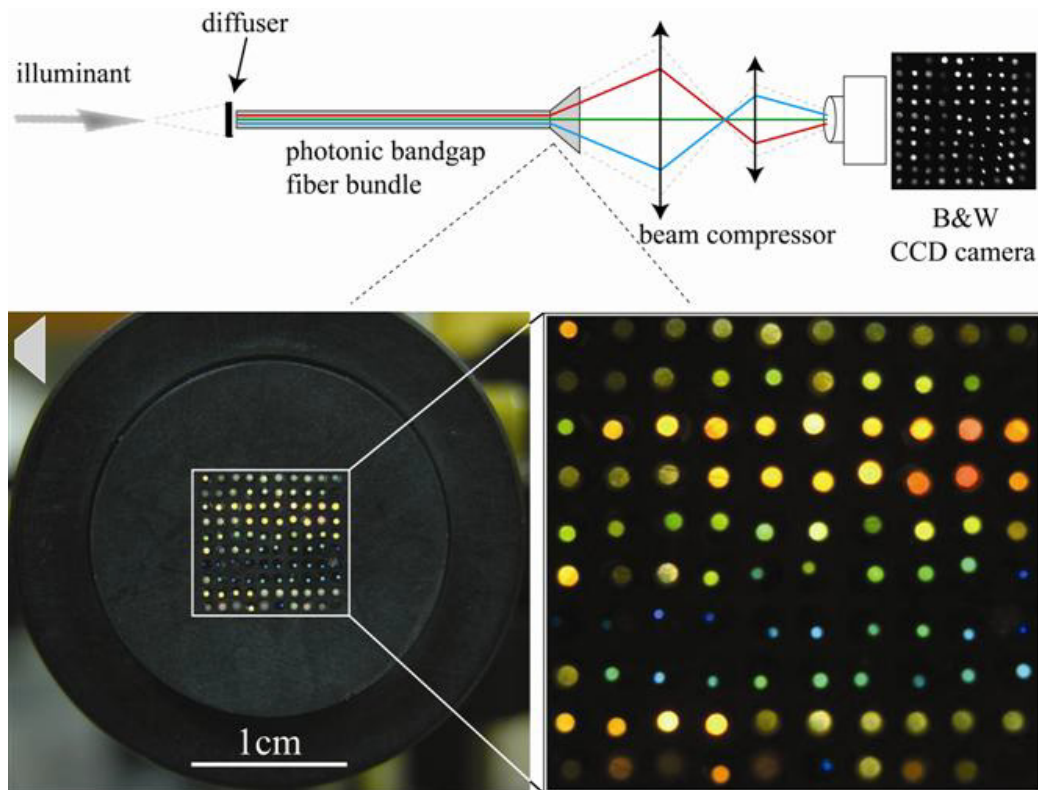
Figure 4.2   Fiber bundle spectrometer. Top part: schematic of the spectrometer. Light from the illuminant is launched into the fiber bundle; the image is taken by the monochrome CCD. Lower part: when the broadband light is launched into the fiber bundle, the output is a mosaic of colors selected by the individual Bragg fibers.

The principle of operation of a Bragg fiber bundle spectrometer can be clearly understood from Fig.4.1 and Fig.4.2. In principle, if all the fiber bandgaps were to be spectrally narrow and non-overlapping, then, at the end of a fiber bundle, the relative intensities of light coming out of the individual fibers would be unambiguously related to the corresponding spectral components of an incoming light. In practice, individual fiber bandgaps are always overlapping, and in our particular implementation, the bandgaps are quite broad. Therefore, to reconstruct the intensity of an incoming light from the intensities of light coming out of the individual fibers, we have to use a certain deconvolution algorithm. Note that spectrometer resolution is not directly limited by the width of fiber bandgaps. We study the resolution by testing a set of spectral peaks with bandwidth from 5 nm to 40 nm. As we will demonstrate in Section 4.5, even with all the individual bandgaps as wide as 60 nm, one could, in principle, reconstruct the peaks as narrow as 5-10 nm. However, to achieve such a high resolution, it is necessary to minimize the

experimental errors and noise contributions. The experimental noises present in the Bragg fiber bundle spectrometer system are briefly introduced in Section 4.5.

Another important comment is about the intensity throughput of our spectrometer and its relation to the spectrometer resolution. First of all, if all the fibers used in the spectrometer were to have strictly complementary and spectrally non-overlapping bandgaps of width $\delta\lambda$, then, to enable a certain spectrometer range $\Delta\lambda=(\lambda_{max}-\lambda_{min})$, one would need to use $N=\Delta\lambda/\delta\lambda$ fibers. Assuming a broadband light with a unit integral power in the spectral range $\Delta\lambda$, we conclude that the intensity throughput through such a spectrometer would be $\sim 1/N^2$. Indeed, the light beam first has to be physically divided into N parts to be launched into the individual fibers of a bundle; then, an individual fiber would cut out a spectrally narrow ($\sim 1/N$) part of the broadband light.

It is important to realize, that our implementation uses N Bragg fibers with relatively large and strongly overlapping bandgaps of spectral width $\delta\lambda >> \Delta\lambda/N$. Spectral resolution of such a spectrometer can be still as small as $\Delta\lambda/N$, while the intensity throughput would be much higher and proportional to $1/N$, rather than $1/N^2$. Such intensity throughput is comparable to the throughput of a grating based spectrometer with resolution of $\Delta\lambda/N$. Indeed, as we will see in what follows, because of the use of a pseudoinversion algorithm, the resolution of a fiber-based spectrometer is fundamentally limited only by the number of the spectroscopic elements, such as individual Bragg fibers, regardless of whether they feature overlapping or strictly complementary bandgaps. On the other hand, the throughput of an individual Bragg fiber with a relatively wide bandgap is $\delta\lambda/\Delta\lambda >> 1/N$. The overall $1/N$ scaling of the throughput intensity, therefore, mostly comes from the necessity of subdivision of a test beam into N individual fibers, each of which individually transmits as much as 30%-50% of the in-coupled intensity. In practice, achieving $\Delta\lambda/N$ resolution with N fibers featuring overlapping bandgaps is somewhat challenging, as a pseudoinverse algorithm used in the spectrum reconstruction is sensitive to the experimental errors.

4.2.3 Sensitivity and linear response of a CCD camera

The output of the fiber bundle is a 10×10 matrix of colored fibers, which is then projected with a beam compressor onto a monochrome CCD array (see Fig.4.2). The sensitivity of a CCD sensor would directly affect the measuring range, the signal-to-noise ratio, and the algorithm that we use

to reconstruct the spectrum of an illuminant. The CCD sensor in our experiment is an Opteon Depict 1, E and S Series B1A 652×494 black and white CCD. The normalized sensitivity for different wavelengths is displayed in Fig.4.3 (a), from which it is clear that the sensor covers well all the visible and a part of a near-infrared spectral range. The sensitivity curve, however, is a highly variable function of wavelength, which must be taken into account in the reconstruction algorithm. Fig.4.3 (a) was obtained by launching the light form a supercontinuum source into a monochromator whose output would produce a 2 nm wide (FWHM) peak at a desired center wavelength. Light from such a tunable source would then be launched into a commercial multimode fiber of ~1 mm diameter. The output power from such a fiber would then be measured by both the CCD array and a calibrated powermeter; the sensitivity curve is then achieved by dividing one by the other.
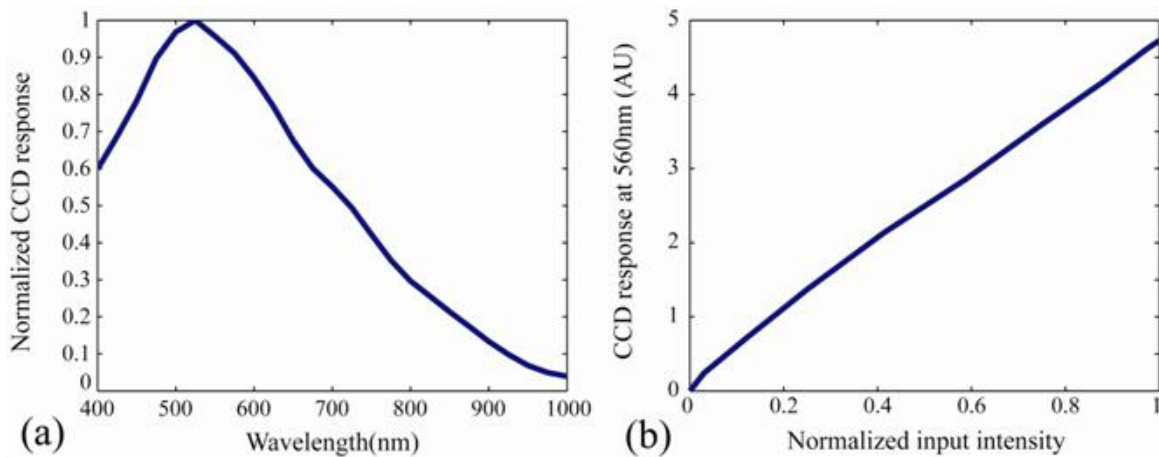
Figure 4.3   (a) Normalized spectral response of a CCD array. (b) A typical monochromatic near-linear response of a CCD array (at λ=560 nm).

As we will see in Section 4.3.1, one of the key requirements of a CCD array is linearity of its monochromatic response as a function of the intensity of incident light. The near-linear response of a CCD sensor was confirmed at several wavelengths of interest; a typical CCD response (at λ =560 nm) is presented in Fig.4.3 (b). To obtain Fig.4.3 (b), two polarizers were placed between a CCD array and the output of a commercial fiber in a setup described in the previous paragraph. By varying the angle between the two polarizers, we also varied the intensity of light coming onto a CCD array. A reference measurement is performed with a calibrated powermeter for the same angles between polarizers; the results are compared to establish a near-linear sensor response.

4.3 Calibration of the fiber bundle spectrometer and spectrum reconstruction algorithm

In its operation mode, the fiber bundle spectrometer is illuminated with a test light, which is then spectrally and spatially decomposed by the fiber bundle (see Fig.4.4). The test spectra used in our experiments were either broadband (halogen lamp source), or narrowband (tunable monochromator source). The image of the fiber bundle output end was then projected onto a monochrome CCD array using a 2:1 beam compressor. Note that a CCD array does not have to be a 2D camera; instead, one can use an economical linear array with the number of pixels matching the number of Bragg fibers in a bundle. The output of each fiber carries information about the intensity of a certain fraction of an illuminant spectrum as filtered by the individual Bragg fibers. It is reasonable to assume, then, that if the Bragg fibers of a bundle feature complementary while possibly overlapping bandgaps that together cover the spectral range of interest, then the spectrum of an illuminant could be reconstructed.

4.3.1 Transmission matrix method

To interpret monochrome CCD image, we use a so-called luminance adaptation model of the fiber spectrometer. Particularly, for a fixed exposure time of a CCD array, total intensity C_n registered by an assigned region of a CCD sensor from the output of the nth fiber can be presented as

$$C_n = \int_{\lambda_{\min}}^{\lambda_{\max}} I(\lambda) A_n F_n(\lambda) S(\lambda) O_n(\lambda) d\lambda , \qquad (4.\,1)$$

where $I(\lambda)$ is the illuminant spectral flux density at the fiber-bundle input end, A_n is the area of the nth fiber input cross section, $F_n(\lambda)$ is the transmission function of the nth fiber, $S(\lambda)$ is the spectral sensitivity of a CCD array, $O_n(\lambda)$ is a fiber-position dependent transmission function of various optics (diffuser, beam compressor, and a CCD objective), λ_{min} and λ_{max} define the spectral range of operation. Measuring such transmission functions individually is a daunting task. Instead, we use a calibration procedure that measures a compounded transmission function of our spectrometer, defined as $T_n(\lambda) = A_n F_n(\lambda) S(\lambda) O_n(\lambda)$. Experimentally, the test spectrum can be divided into N equidistant spectral "bins" with the size of each bin to be $\Delta\lambda = (\lambda_{\max} - \lambda_{\min}) / N$.

Correspondingly, the transmission function T_n for nth Bragg fiber can be discretized into a vector with N elements. The model in Eq. (4.1) could then be rewritten as

$$C_n = \int_{\lambda_{\min}}^{\lambda_{\max}} I(\lambda)T_n(\lambda)d\lambda = \sum_{i=0}^{N=(\lambda_{\max}-\lambda_{\min})/\Delta\lambda} T_n^i(\lambda_i)\int_{\lambda_i=\lambda_{\min}+i\lambda}^{\lambda_i+\Delta\lambda} I_i(\lambda)d\lambda = \sum_{i=0}^{N} I_i \cdot T_n^i \qquad (4.2)$$

When we take all the Bragg fibers in the bundle into account, Eq. (4.2) presented in the matrix form becomes

$$\begin{bmatrix} C_1 \\ C_2 \\ .. \\ .. \\ C_{100} \end{bmatrix} = \begin{bmatrix} T_{1,1} & T_{1,2} & \cdots & T_{1,N} \\ T_{2,1} & T_{2,2} & \cdots & T_{2,N} \\ .. & & & \\ .. & & & \\ T_{100,1} & T_{100,2} & \cdots & T_{100,N} \end{bmatrix} \begin{bmatrix} I_1 \\ I_2 \\ .. \\ .. \\ I_N \end{bmatrix} \qquad (4.3)$$

where vector $(C)_{100\times1}$ represents the intensities of light coming out of the individual fibers as measured by the CCD sensor, $(T)_{100\times N}$ is a spectrometer transmission matrix, and $(I)_{N\times1}$ is a discretized spectrum of the illuminant. From Eq. (4.3), it follows that a discretized spectrum of the illuminant can be reconstructed from the corresponding CCD image (C vector) by inverting the transmission matrix of a spectrometer.

4.3.2 Calibration measurement, building a transmission matrix

To construct transmission matrix experimentally, we note that, if the illuminant spectrum is monochromatic ($I_i = 0$, $\forall i \neq i_\lambda$ in Eq. (4.3)), then the measured C^{i_λ} vector is proportional to the i_λ column of the transmission matrix:

$$C_{(100\times1)}^{i_\lambda} = T_{(100\times1)}^{i_\lambda} \cdot I_{i_\lambda} \qquad (4.4)$$

Experimentally, we use a tunable monochromator-based narrowband (2 nm FWHM) source to generate "monochromatic" spectra (see Fig.4.4). Particularly, we vary the source center wavelength in 2 nm increments, thus effectively subdividing the 400-840 nm spectral interval under consideration into $N = 221$ equivalent 2 nm wide bins. For every new position of the source center wavelength, we acquire a C vector using a CCD array and consider it as the next column of the spectrometer transmission matrix. Finally, to finish the calibration we measure the

wavelength-dependent intensities I_i of a tunable source by placing a calibrated powermeter directly at the output of a monochromator. By dividing every C vector by the corresponding I_i value, the transmission matrix is constructed.
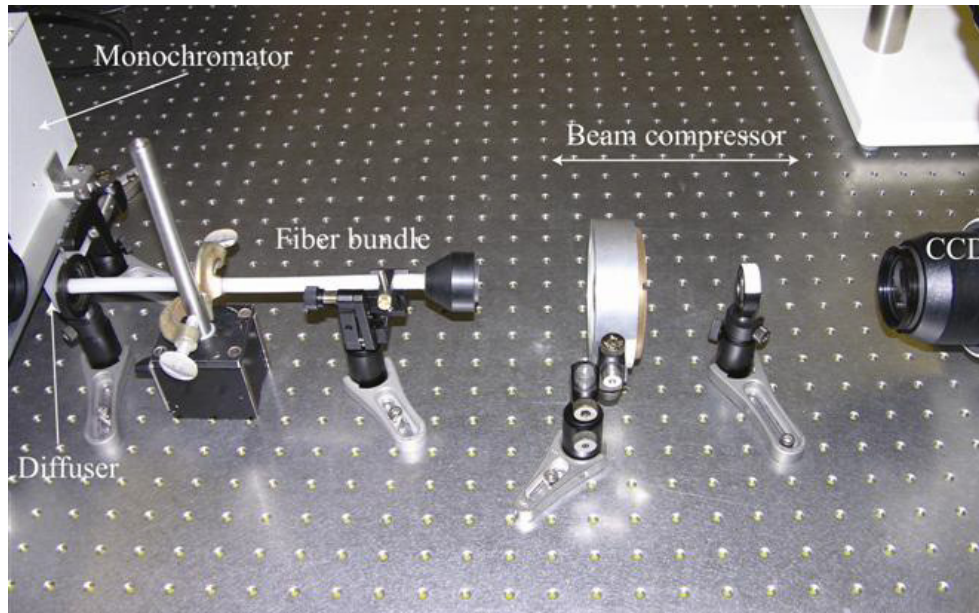
Figure 4.4   Setup for the spectrometer calibration measurement.

In our experiments, an S&Y halogen lamp source was used with a Newport Oriel 1/8 m monochromator to build a narrowband tunable source of 2 nm FWHM (see Fig.4.4). The light beam from the source was then directed onto a diffuser placed right before the fiber bundle to guarantee a uniform illumination of its input end. At the output end of a fiber bundle, a 2:1 beam compressor was used to image the fiber bundle output facet onto the 8-bit monochrome CCD sensor array. Individual images were then interpreted using a singular value decomposition (SVD) pseudoinversion algorithm to construct the corresponding C vectors. The wavelength-dependent intensity of a tunable source was measured using a calibrated Newport 841-PE powermeter.

4.3.3 Spectral reconstruction algorithm

As it was noted in Section 4.3.1, a discretized spectrum of the illuminant can be reconstructed from the corresponding CCD image (C vector) by inverting the transmission matrix of a spectrometer in Eq. (4.3). However, an immediate problem that one encounters when trying to invert the transmission matrix is that the matrix is non-square. Even if the number of spectral bins is chosen to match the number of fibers in the bundle, thus resulting in a square transmission

matrix, one finds that such a matrix is ill-conditioned. One, therefore, has to resort to an approximate inverse of a transmission matrix. To find a pseudoinverse of a transmission matrix in Eq. (4.3) we employ a SVD algorithm. Particularly, from linear algebra, we know that any (*100×N*) matrix (suppose that *N>100*) can be presented in the form

$$\left(T\right)_{100\times N} = \left(U\right)_{100\times 100}\left(S\right)_{100\times N}\left(V^T\right)_{N\times N}$$
$$U^T U = 1 \; ; \; V^T V = 1 \; ; \; S = diag(\sigma_1, \sigma_2, \sigma_3, ...\sigma_{100})$$
$$\sigma_1 > \sigma_2 > \sigma_3 > ... > \sigma_{100} > 0$$

(4. 5)

where matrixes *U* and *V* are unitary, and matrix *S* is a diagonal matrix of the real positive singular values. For the ill-conditioned matrices, most of the singular values are small and can be taken as zero. By limiting the number of nonzero singular values to N_σ, Eq. (4.5) can be rewritten as

$$\left(T\right)_{100\times N} = \left(U\right)_{100\times N_\sigma}\left(S\right)_{N_\sigma\times N_\sigma}\left(V^T\right)_{N_\sigma\times N}$$
$$\sigma_1, \sigma_2, ..., \sigma_{N_\sigma} \neq 0$$

(4. 6)

and a corresponding pseudoinverse of the transmission matrix is then found as

$$\left(T\right)^{-1}_{N\times 100} = \left(V\right)_{N\times N_\sigma}\left(S\right)^{-1}_{N_\sigma\times N_\sigma}\left(U^T\right)_{N_\sigma\times 100}$$

(4. 7)

4.4   Spectral reconstruction experiments

To test our fiber bundle spectrometer, we perform reconstruction of several test spectra. In one set of experiments, the test spectra is a set of the 25 nm wide peaks centered at 450, 500, 550, 600, and 700 nm. Such peaks were created using the same monochromator-based tunable source as used for the spectrometer calibration; however, it was adjusted to have a 25 nm bandwidth in the outgoing light. In the second set of experiments, we measure the spectra of four 40 nm wide bell shaped curves centered at 450, 500, 550, and 600 nm created using four commercial bandpass filters. In Fig.4.5 we demonstrate, with dashed curves, the test spectra of light beams at the input of a fiber bundle (as resolved by another Oriel monochromator), while with solid curves, we show the corresponding reconstructed spectra using the transmission matrix inversion algorithm. In the figures, we also indicate the optimal number of nonzero singular values used in the matrix inversion procedure (Eq. (4.7)). The choice of the number of nonzero singular values used in the

spectrum reconstruction algorithm strongly affects the quality of the reconstructed spectrum. Note, in particular, that although the spectral intensity function should be strictly non-negative, the reconstructed spectral intensity can take negative values. Therefore, spectrum reconstruction error can be defined as the ratio of the most negative value in the reconstructed spectral intensity to its most positive value:

$$Error(N_\sigma) = -\min_\lambda(I_{N_\sigma}^{reconstr.}) / \max_\lambda(I_{N_\sigma}^{reconstr.}) , \tag{4.8}$$

and the optimal N_σ to be used in Eq. (4.7) is the one that minimizes the error in Eq. (4.8).

(a)

(b)
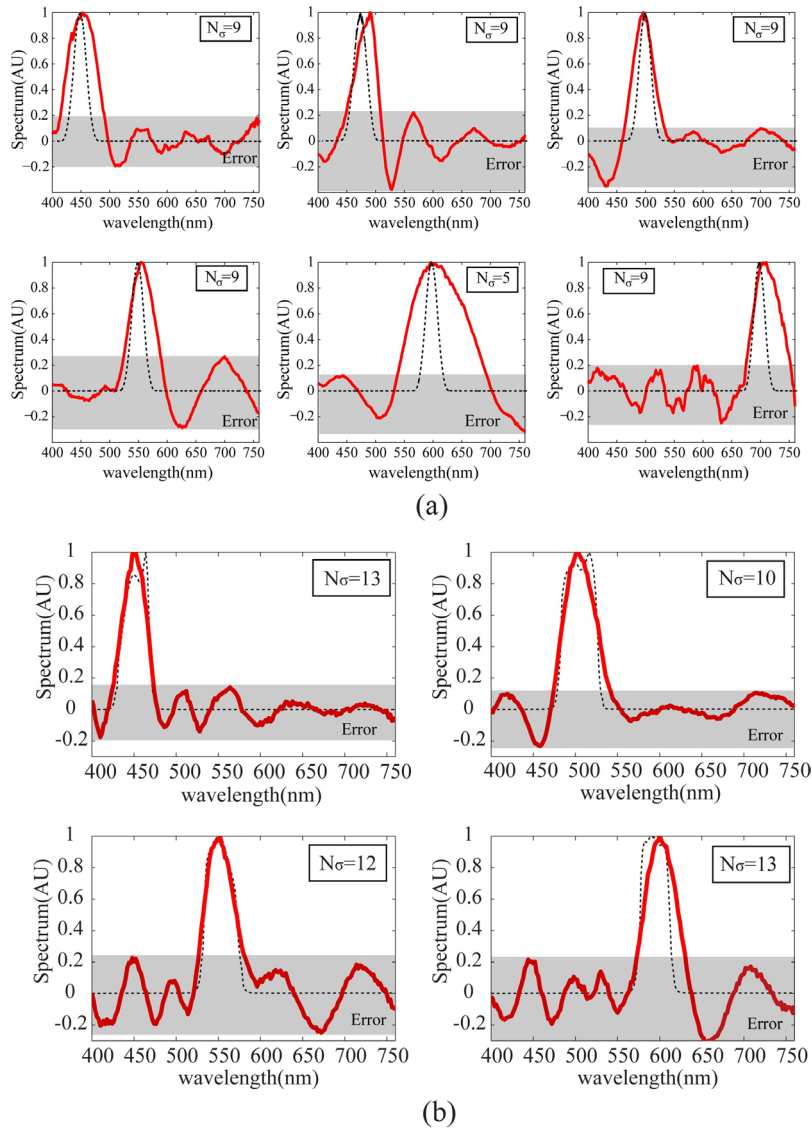
Figure 4.5   Spectra reconstruction using photonic bandgap fiber bundle-based spectrometer. The top part (a) shows the reconstructed spectra of six 25 nm wide peaks; the bottom part (b)

shows the reconstructed spectra of four 40 nm wide bell-shaped spectra. The black dash lines are the test spectra resolved by another monochromator; the red thick lines are the spectra reconstructed by the fiber bundle spectrometer. The gray area indicates error level.

From Fig.4.5 we conclude that the test peak position (the value of the peak center wavelength) can be reconstructed within several percent of its true value in the whole spectral range covered by the spectrometer. Moreover, we note that although the widths of the individual Bragg fiber bandgaps are quite large (> 60 nm), the fiber bundle-based spectroscopic system can resolve peaks of much smaller spectral width. Indeed, in Fig.4.5 (a), the widths of the reconstructed spectra are in the 30-50 nm range, with the exception of a peak centered at 600 nm. We mention in passing that we have also conducted measurements using 5, 10, 15, and 20 nm wide peaks. In all the experiments, we saw that the center wavelength of even the narrowest peak can be reconstructed with high precision; however the reconstructed peak width always stayed around 30 nm. Finally, 40 nm wide test peaks could be well reconstructed, in terms of their spectral position and width (see Fig.4.5 (b)).

4.5 Spectral resolution limit for the Bragg fiber bundle spectrometer

To understand the resolution limit of our spectrometer, we first study the effect of the choice of the number of nonzero singular values N_σ used in the inversion algorithm of Eq. (4.7). Initially we assume that there is no noise in the system. As a test spectrum $I(\lambda)$, we consider a 20 nm wide peak centered at the wavelength of 520 nm (dashed curve in Fig.4.6 (a)).
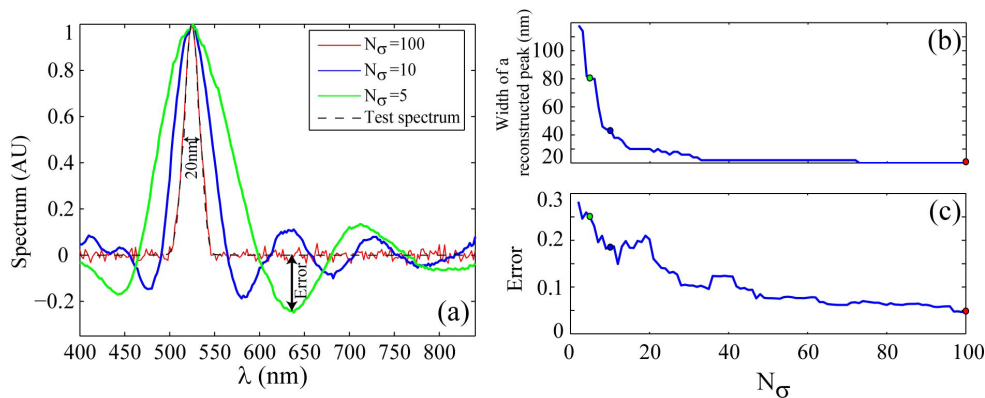
Figure 4.6   Properties of the reconstructed spectra as a function of the number of singular values used in the inversion algorithm. No noise is present in the system. (a) Dependence of the

spectral shape of a reconstructed peak on N_σ. (b) Width of a reconstructed peak as a function of N_σ. (c) Reconstruction error as a function of N_σ

We multiply the discretized test spectrum by the transmission matrix of our spectrometer (measured experimentally), and then reconstruct the test spectrum using a transmission matrix pseudoinverse with N_σ singular values:

$$(C)_{100\times1} = (T)_{100\times N}(I)_{N\times1}$$
$$\left(I_{N_\sigma}^{reconstr.}\right)_{N\times1} = (V)_{N\times N_\sigma}(S)_{N_\sigma\times N_\sigma}^{-1}\left(U^T\right)_{N_\sigma\times100}(C)_{100\times1} \tag{4.9}$$

Thus, the reconstructed spectrum is then compared to the original test spectrum. In Fig.4.6 (a), we present several reconstructed spectra for the different numbers of singular values used in the inversion algorithm. If all of the 100 singular values are used (red thin curve in Fig.4.6 (a)), then the 20 nm wide peak is very well reconstructed, featuring a less than 5% intensity difference from the reconstructed spectrum. The error manifests itself as ripples at the peak tails. When a smaller number of singular values are used (for example, $N_\sigma = 10$, blue solid curve in Fig.4.6 (a)), the center wavelength of the reconstructed peak still coincides very well with that of a test peak; however, the reconstructed peak width is larger than that of a narrow test peak. This result is easy to understand by remembering that the expansion basis set used in the reconstruction algorithm is formed by the relatively broad (> 60 nm, see Fig.4.1) transmission spectra of the Bragg fibers; therefore, one needs a large number of such basis functions (singular values) to reconstruct a narrow spectral feature. In Fig.4.6 (b), the FWHM of the reconstructed peak is shown as a function of the number of singular values used in the matrix inversion. Note that more than 40 singular values have to be used to achieve a width of a reconstructed peak to be close to 20 nm. When only 10 singular values are used, the width of a reconstructed peak increases to 40 nm. Additionally, the peak reconstruction error, as defined by Eq. (4.8), increases to 20% when a small number of singular values ($N_\sigma < 20$) are used. From this we conclude that, with no noise present in the system, the peak reconstruction error and the quality of a reconstructed spectrum improves when a larger number of singular values are used.

We now study the effect of experimental noise on the quality of a reconstructed spectrum. There are several sources of noise in our spectrometer. One is the discrete intensity resolution of a CCD array; with the 8 bit encoding, the fundamental noise is ~0.1%. The ambient light in the

experimental environment also contributes to noise on a CCD sensor. Moreover, because of the relatively large size of a fiber bundle (~6 mm), it is difficult to ensure the same illumination conditions of the bundle input facet for all the sources used in the experiments.

To model experimental noise numerically, we first multiply the test spectrum by the transmission matrix of our spectrometer, then add a uniformly-distributed random noise of the relative intensity δ to the C vector (monochrome image), and finally, reconstruct the test spectrum by using a transmission matrix pseudoinverse with N_σ singular values:

$$(C)_{100\times1} = (T)_{100\times N}(I)_{N\times1}$$
$$\left(C^{noise}\right)_{100\times1} = (C)_{100\times1}\cdot\left(1+\delta\cdot(\eta)_{100\times1}\right) \; ; \; \eta-random \subset [-0.5,0.5] \tag{4.10}$$
$$\left(I_{N_\sigma}^{reconstr.}\right)_{N\times1} = (V)_{N\times N_\sigma}(S)_{N_\sigma\times N_\sigma}^{-1}\left(U^T\right)_{N_\sigma\times100}\left(C^{noise}\right)_{100\times1}$$

With these definitions, we first revisit the case when all the 100 singular values are used for spectrum reconstruction. As noted above, in the absence of noise ($\delta=0$ in Fig.4.7 (i)), the 20 nm peak can be well reconstructed with only ~5% error. However, the addition of even a small amount of noise ($\delta=0.005$ in Fig.4.7 (ii)) results in an extremely noisy reconstructed image, with errors as large as 50%. Note that, by using a smaller number of singular values $N_\sigma \subset [20,40]$ (see the error plot in the top part of Fig.4.7), the peak reconstruction error can be greatly reduced down to 10%, while still allowing a fair estimate of the peak width ~30 nm. When the noise level is increased further, to avoid large reconstruction errors, one has to use a relatively small number of singular values $N_\sigma < 20$ (see Figs.4.7 (iii, iv)). Notably, reconstruction error saturates at 20% even for large noise levels; however, the reconstructed peak width always stays larger than 30 nm due to a small number of singular values used.
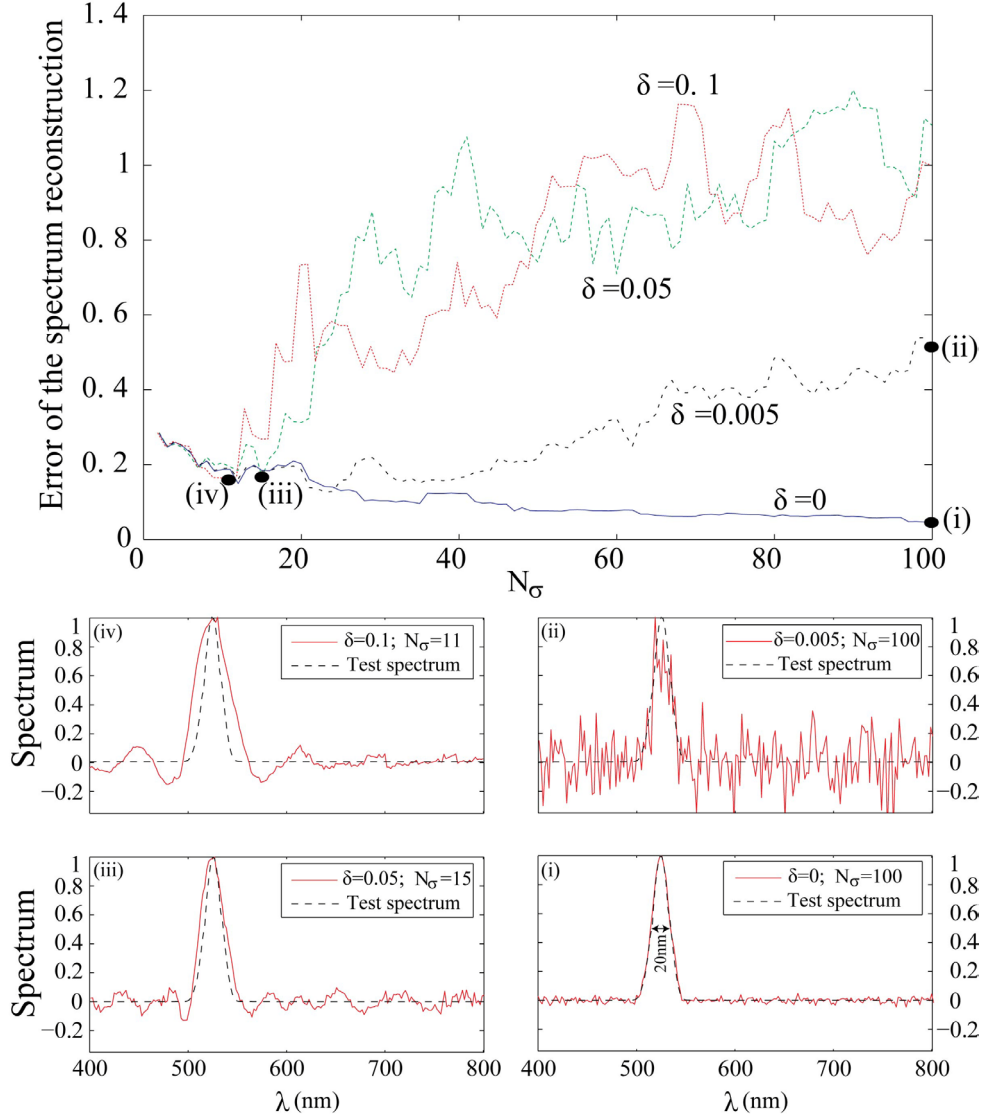
Figure 4.7   Effect of noise on the quality of reconstruction. Examples of the reconstructed spectra for several particular realizations of noise with amplitudes: (i) $\delta = 0$, (ii) $\delta = 0.005$, (iii) $\delta = 0.05$, (iv) $\delta = 0.1$.

To put the noise value of $\delta = 0.005$ into perspective, we note that this corresponds to 0.5% of total experimental error in the amplitude measurement of the C vector components. The noises present in measuring a C vector include the quantization noise of the CCD sensor, the ambient light contribution from the experimental environment, the measurement-to-measurement variation in the illumination conditions on the input facet of the fiber bundle, etc. As noted before, the contribution of quantization noise is $\sim 0.1\%$. We have verified that the ambient light noise is below 1 unit in the 8 bit coding, while the CCD sensor was configured so that the maximum of

the fiber output is close to (but smaller than) 256 units per pixel. Thus, the ambient light noise is limited to 1/256=0.39%. Thus, $\delta = 0.005$ is based on the assumption that only ambient light noise and quantization noise exist in the measurement of C vector, while for other higher δ, the other types of noise gradually become dominant. We find that the biggest contribution to noise is caused by the difficulty in the reproducing the same illumination conditions of the fiber bundle facet when constructing the transmission matrix, and when characterizing the test spectra. The main reason for this is that, to construct the spectrometer transmission matrix, we use a monochromator-based source, while to characterize the test spectra, we use a halogen lamp source. Because of the relatively large size of a fiber bundle, it is then difficult to guarantee consistent illumination of the fiber bundle surface, even when using a diffuser in front of the fiber bundle. An obvious remedy to this problem is to reduce the size of the fiber bundle and to use a better diffuser, or mode scrambler, at the input. To address the first problem, we report in Section 4.6 a new fabrication technique where a smaller size fiber bundle is fabricated by direct drawing. Additionally, a several-meter-long large-core multimode fiber can be used to first scramble and equalize polarization and incident angle distributions of the input light, and then lunch the scrambled light into the fiber bundle.
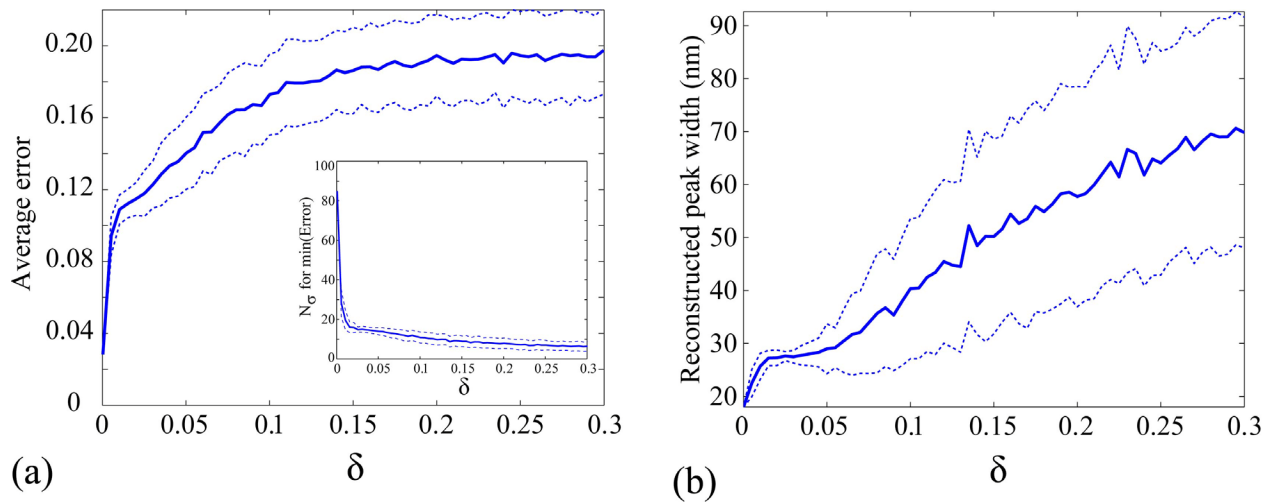
Figure 4.8 Effect of noise on the reconstruction algorithm. (a) Average reconstruction error and its statistical deviation as a function of the noise amplitude. Inset: optimal number of singular values needed to minimize the reconstruction error. (b) Average width of a reconstructed peak and its statistical deviation as a function of the noise level.

Finally, Fig.4.8 presents statistical averages of various parameters (thick solid curves), as

well as their statistical deviation from the average (thin dashed curves) as a function of the noise level. To construct these curves, for every value of the noise amplitude δ, we first generate 200 realizations of noise. Then, for every realization of noise, we plot the error of peak reconstruction as a function of the number of singular values (similar to Fig.4.7). Last, the smallest error, the corresponding N_σ, and the width of a reconstructed peak are recorded and statistical averages are computed. In Fig.4.8 (a) we present the average peak reconstruction error as a function of the noise amplitude. Note that, although the error grows with the noise amplitude, it, nevertheless, saturates at ~20%, even for large noise levels. In the inset of Fig.4.8 (a), we see that, at very small noise levels ($\delta < 0.02$), to obtain the smallest reconstruction error one can use almost all 100 singular values, while at higher noise levels, fewer than 20 singular values should be used. As a consequence, for larger noise amplitudes, the width of a reconstructed peak could become considerably larger than that of a test peak (20 nm).

4.6   Novel technique for drawing PBG fiber bundles
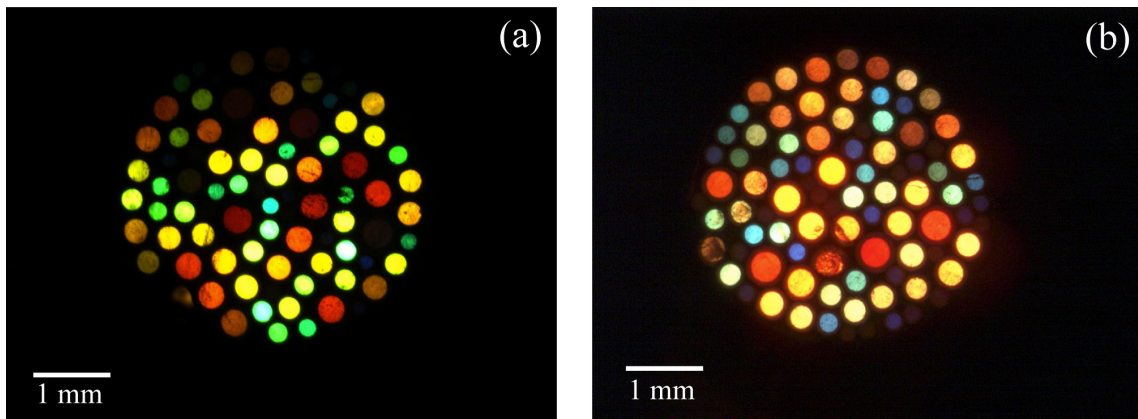
Figure 4.9   Cross sections of the PBG fiber bundles fabricated using the two-stage drawing technique. The bundle is illuminated with a broadband halogen lamp. At the output of fiber bundle, a mosaic of colors is visible as the white light is filtered by each fiber insider the bundle.

Finally, we report a two-stage drawing technique for the direct fabrication of the PBG fiber bundles. This technique constitutes an industrial-strength alternative to the manual bundling of the individual fibers, as it was presented in Section 4.2. The proposed technique comprises "two stages". First, we produce a Bragg fiber preform by a co-rolling technique [203] and draw it into intermediate preforms with relatively large and variable diameters (1-1.5 mm). Second, we bundle these intermediate preforms, place them into a thin supercladding tube, and, finally, draw

this structure into a PBG fiber bundle. Cross sections of the PBG fiber bundles are presented in Fig.4.9. Each PBG fiber bundle is illuminated by light from a broadband source (halogen lamp), and the light is then split by the individual fibers into the respective spectral components, as seen in Fig.4.9. We are currently working on the perfection of this fiber bundle fabrication technique to include more fibers, and to reduce the bundle outer diameter in order to demonstrate compact and high resolution spectrometers that are also resistant to experimental noise.

4.7 Conclusions

We have demonstrated experimentally a novel all-fiber spectrometer comprising a PBG Bragg fiber bundle and a monochrome CCD camera. One hundred solid-core Bragg fibers with complementary bandgaps covering a 400-840 nm spectral range are placed together to make a ~6 mm diameter, 30 cm long fiber bundle. The spectrometer operates by launching the light into a fiber bundle and then recording the color-separated image at the fiber bundle output facet using a CCD camera. An inversion algorithm is developed to reconstruct the test spectrum using black and white intensity images. Among the clear advantages of our spectrometer are the lack of moving parts, a near instantaneous and parallel acquisition of all the spectral components, compactness, a high degree of integration and simplicity of operation.

The Bragg fiber bundle spectrometer is demonstrated experimentally to resolve relatively narrow spectral peaks (5-40 nm) with high precision in determining the position of the peak center wavelength. Even when the peak width is much narrower than the bandwidth of individual Bragg fibers making up the fiber bundle, the peak width could still be resolved correctly, however, the reconstruction algorithm is found to be sensitive to experimental noise. The experimental resolution limit of the fiber bundle spectrometer presented in this thesis is found to be ~30 nm. Theoretical analysis predicts that resolution limit of the existing setup could be greatly improved by (1) minimizing the experimental errors related to repeatability of light injection into the bundle, (2) optical isolation of the bundle from the environment, and (3) minimizing discretization errors introduced by the camera. We estimate that the resolution of the Bragg fiber bundle spectrometer can be improved to several nm in width by minimizing the experimental noises. Finally, we demonstrate a two-stage industrial-strength drawing technique suitable for mass production of the PBG Bragg fiber bundles.

CHAPTER 5   ARTICLE 3: ALL PHOTONIC BANDGAP FIBER SPECTROSCOPIC SYSTEM FOR DETECTION OF REFRACTIVE INDEX CHANGES IN AQUEOUS ANALYTES

5.1   Introduction

In the two preceding chapters, we have detailed a liquid-core Bragg fiber refractometer and a solid-core Bragg fiber spectrometer. In this chapter, we describe integration of the two fiber devices into a complete all-fiber spectroscopic system for liquid refractometry.

5.1   Integration of the liquid-core Bragg fiber refractometer and the solid-core Bragg fiber bundle spectrometer

We start this section by briefly reminding the reader of the operating principles behind the liquid-core Bragg fiber sensor and the solid-core Bragg fiber spectrometer. The liquid-core Bragg fiber sensor operates using resonant sensing modality, in which changes in the refractive index of a liquid analyte filling the fiber core modify the resonant guidance of the fiber, thus shifting the spectral position of the fiber transmission peek (see Section 3.2). The Bragg fiber spectrometer uses a transmission matrix algorithm (see Section 4.3.1), in which the unknown spectrum is retrieved from the CCD-registered intensity image of the fibers in the cross section of a spectroscopic bundle. We believe that a highly-sensitive all-fiber refractometric system could be realized by integration of the liquid-core Bragg fiber with the solid-core Bragg fiber bundle spectrometer.

5.1.1   Calibration measurement of the all-Bragg-fiber refractometer system

We start the integration from a calibration measurement to calculate the transmission matrix (Eq. (4.3)) of the Bragg fiber bundle spectrometer. We firstly couple the beam from a supercontinuum source into a tunable monochromator (2 nm FWHM) to constitute a tunable light source. The output of the monochromator is then coupled into a 40 cm long Bragg fiber filled with distilled water. Since the light from the monochromator-based source is relatively weak, the water-filled Bragg fiber is kept straight during the calibration measurement in order to reduce the propagation loss. The transmitted light from the liquid-core Bragg fiber is coupled into the Bragg fiber bundle

spectrometer using another 10× objective, and a monochrome CCD camera is used to record the intensity image of the Bragg fiber bundle. We then vary the source center wavelength in 2 nm increments, thus effectively subdividing a 560-740 nm spectral interval of interest into 91 bins with equivalent 2 nm widths. At each wavelength, the intensity of the monochromator-based source, I_i, is measured by a calibrated powermeter. Besides, at each wavelength, we also acquire a $C_{100 \times 1}$ vector using the CCD camera (see Eq. (4.3), a $C_{100 \times 1}$ vector represents the intensities of light coming out of the individual fibers as measured by the CCD sensor). According to Eq. (4.3), a column of the transmission matrix T can be calculated by dividing a $C_{100 \times 1}$ vector by the corresponding I_i value. Thus, the complete T matrix can be obtained by repeating the same measurement at every interested wavelength in the 560-740 nm spectral range. Once we have the complete T matrix, a test spectrum (i.e., transmission spectrum of the liquid-core Bragg fiber) can be reconstructed using a pseudoinverse of the T matrix according to Eq. (4.7). Finally, we remove the monochromator from the calibration setup and couple the supercontinuum beam directly into the liquid-core Bragg fiber with a 10× objective. The transmission spectra of the liquid-core Bragg fiber can then be analyzed using the Bragg fiber bundle spectrometer.

5.1.2 Experimental characterization of the all-Bragg-fiber refractometer system

We use NaCl solutions with different concentrations as liquid analytes to experimentally characterize the all-Bragg-fiber refractometric system. The transmission spectra of the liquid-core Bragg fiber measured by the Bragg fiber bundle spectrometer is shown in Fig.5.1 (a). As a reference, we also measure the transmission spectrum of the liquid-core Bragg fiber by directly coupling it to a conventional grating monochromator (Fig.5.1 (b)). For ease of comparison, the spectra measured both by the Bragg fiber bundle spectrometer and by the grating monochromator are normalized to 1. Since the spectra reconstructed by the fiber bundle spectrometer and measured by the grating monochromator are relatively wide, we, therefore, calculate the center position of a transmission peak by averaging the corresponding wavelengths where the normalized intensities are above 0.95.
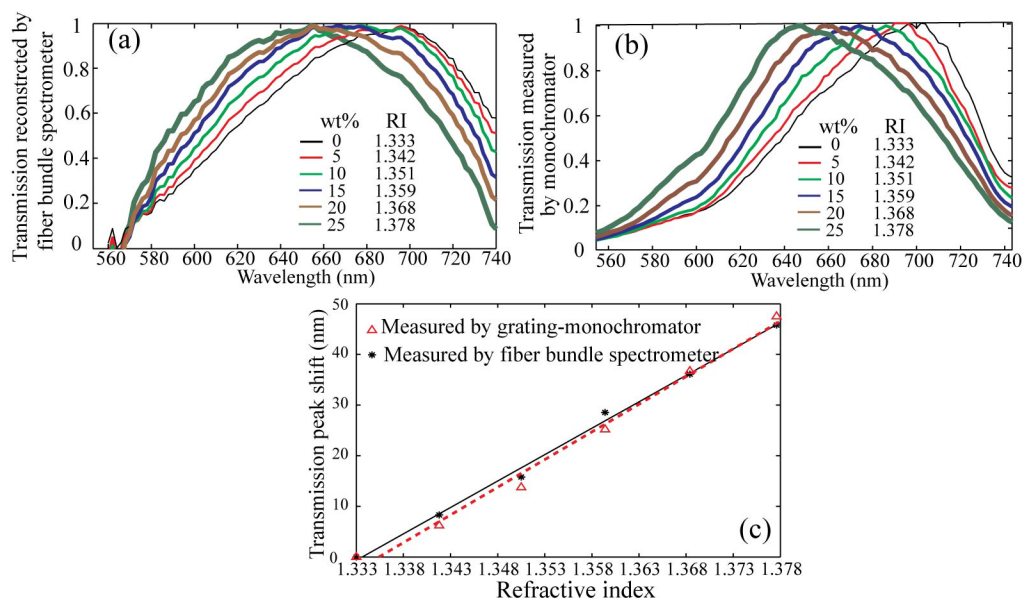
Figure 5.1   Transmission spectra of a ~40 cm long liquid-core Bragg fiber measured by (a) the Bragg fiber bundle spectrometer and (b) a conventional grating monochromator. The concentrations and corresponding refractive indices of the NaCl solutions are listed as the inset. (c) Spectral shifts of the transmission peak measured by the grating monochromator (dashed red line) and by the Bragg fiber bundle spectrometer (solid black line).

In Fig.5.1 (c), we compare the spectral shifts of the transmission peak measured by both the Bragg fiber bundle spectrometer and the grating monochromator. We note that the spectral shifts of the transmission peak feature a linear dependence with respect to variations in the refractive index of the liquid core of the Bragg fiber. The experimental sensitivity of the liquid-core Bragg fiber sensor is ~1100 nm/RIU measured by the grating monochromator, and is ~1050 nm/RIU measured by the Bragg fiber spectrometer. Note that in both measurements presented in Fig.5.1, the spectral shifts (see Fig.5.1 (c)) are marginally smaller than those shown in Fig.3.4. This is likely due to the fact that in the measurements (including the calibration measurements) for Fig.5.1, the liquid-core Bragg fiber is kept straight in order to reduce the propagation loss of the fiber. Therefore, many high-order modes, which are less sensitive to variations in the refractive index of the fiber core, can propagate through the fiber, thus resulting in smaller spectral shifts. However, in the measurements for Fig.3.3 and Fig.3.4, signal-to-noise degradation is not a critical issue, since we use a more sensitive single-pixel detector for spectral interrogation as compared to the CCD detector used in the Bragg fiber spectrometer. Consequently, we coil the

Bragg fiber piece in a 10 cm diameter circle in order to strip out high-order modes, thus leading to stronger spectral shifts.

5.3 Conclusions

In this chapter, we demonstrate the integration of the liquid-core Bragg fiber transducer with the solid-core Bragg fiber bundle spectrometer to create an all-Bragg-fiber refractometer system. The liquid-core Bragg fiber is used to hold and probe liquid analytes filling the fiber core, and the solid-core Bragg fiber is used to analyze the transmission spectrum. The methodology for integration and characterization of the all-Bragg-fiber refractometer system is demonstrated in detail in this chapter. The sensitivity of the all-Bragg-fiber refractometer system is found to be ~1100 nm/RIU.

CHAPTER 6   GENERAL DISCUSSION, CONCLUSIONS AND PERSPECTIVES

In the previous chapters, we propose and experimentally demonstrate a liquid-core Bragg fiber refractometer and a solid-core Bragg fiber spectrometer. Moreover, we demonstrate integration of the above-mentioned devices into a single all-fiber spectroscopic system for the high sensitivity detection of changes in the bulk refractive index of liquid analytes. Both theoretical analyses and experiments are performed to characterize the proposed devices. In this chapter, we would like to reiterate the distinctive features of the proposed systems, discuss their potential applications as well as indicate the future research direction for this project.

6.1   Liquid-core Bragg fiber refractometer

The liquid-core Bragg fiber transducer detailed in Chapter 3 constitutes a simple, compact and cost-effective solution for the detection of small changes in the refractive index of liquid analytes. The hollow-core Bragg fiber drawn using a commercial fiber-drawing tower can be directly integrated into the fluidic setup without any special fiber pre-treatments such as chemical etching or grating inscription, which simplifies greatly fabrication of a complete sensor system. The sensing mechanism is based on interpretation of the shift in the position of a fiber transmission in response to changes in the bulk refractive index of a liquid analyte filling the fiber core. The sensitivity of the proposed fiber sensor can achieve ~1400 nm/RIU. This defines a sensor resolution of ~7×10^{-5} RIU, assuming that 0.1 nm spectral shift of the transmission peak can be reliably detected. We note the sensitivity of our simple Bragg fiber sensor is comparable to that of the much more complex fiber-optic SPR sensors [98-100]. We also note that the sensitivity of the Bragg fiber sensor presented in this work does not strongly depend on the fiber length due to the resonant sensing mechanism. Therefore, a compact sensor can be constructed using a several-centimeter-long Bragg fiber.

6.1.1   Response time of the liquid-core Bragg-fiber refractometer

One of the principal advantages of our Bragg fiber sensor compared to other MOF-based sensors is its short response time (~1 s for a 40-cm-long fiber) due to the large core size of the fiber. This makes the hollow-core Bragg fiber sensors suitable for monitoring of the time-dependent

chemical or biological processes. In micro-fluidic capillaries [22], the fluidic resistance increases polynomially when decreasing the capillary radius. This explains the long response time (~10 minutes for a 20 cm long fiber [22, 23]) of many standard MOF sensors that feature micron-size holes. We note, however, that the quick response time of our Bragg fiber sensor comes at the cost of a larger analyte volume. While a typical analyte volume of ~200 μL is required for the liquid-core Bragg fiber sensor, less than 1 μL liquid analyte is sufficient for many liquid-core MOF sensors [22].

6.1.2   Bulk sensing modality and surface sensing modality

It is important to note that hollow-core Bragg fiber sensors are mostly sensitive to the "bulk" changes of the analyte refractive index, while other MOF-based sensors can be also very sensitive to changes in the analyte refractive index in the vicinity of the functionalized surfaces. We have experimentally characterized the "surface" sensitivity of our Brag fiber sensors and found very modest sensitivities of ~1μm/nm to variations in the layer thickness of an analyte layer deposited on the inner surface of a hollow core. This sensitivity is two orders of magnitude smaller than those of the liquid-core MOF sensors (see Ref. [204], for example). We note that this modest surface sensitivity is due to a poor overlap between the guided light and the analyte layer. Potentially, higher surface sensitivities can be achieved by reducing the core size of a Bragg fiber so that the modal overlap with the analyte layer is enhanced. However, this would also result in longer sensor response times. Alternatively, one can introduce a porous network of thin bridges that can be biologically or chemically functionalized. This will increase the modal overlap with the analyte layers; however, fabrication of such fibers could be challenging.

6.1.3   Air bubbles in the experimental setup

One technical challenge associated with operation of the liquid-core fiber sensors is the infiltration of air bubbles into the fiber core during sample-filling process. These air bubbles not only bring strong optical scattering (small air bubbles), but can also lead to the formation of air cavities (large air bubbles), thus modifying the fiber transmission spectrum. Therefore, a proper design of the opto-fluidic system is required for the liquid-core fiber sensors in order to avoid the presence of air bubbles in the sensing system. In our experimental setup, we employ two opto-fluidic blocks in order to realize an opto-fluidic coupling into the Bragg fibers (see Fig.3.1 (c)).

Particularly, the fiber tip is sealed hermetically in the horizontal channel of a block that has a thin glass window attached at one of its extremities. Each block also features a vertical channel, which is connected to the horizontal channel, thus realizing a continuous fluidic path for injection of the analyte into the Bragg fiber. A pump (or a syringe) can be used to pump analytes into the core of a Bragg fiber for sensing applications. In our experience this simple opto-fluidic design effectively avoids introduction of air bubbles into the sensing system.

6.1.4 Spectral shifts of low-order modes and high-order modes

In Chapter 3, we perform simulations and experiments to characterize spectral shifts of the Bragg fiber sensor in response to changes in the refractive index of the fiber core. We find that the spectral shifts obtained from the TMM simulations are larger than the ones measured experimentally. The possible reason for this is explained as follows. In our simulations, we only calculate the spectral shifts of the fundamental HE_{11} mode. However, in our experiments, many high-order modes can be excited due to the large diameter of the Bragg fiber core. These high-order modes generally have a smaller fraction of power overlapping with test analytes, as compared to the fundamental mode, thus being less sensitive to refractive index variations. To further confirm this, we now carry out a TMM simulation to calculate loss spectra of a high-order mode ($HE_{1, 48}$ mode) of the Bragg fiber filled with NaCl solutions. In this simulation, the structural parameters of the Bragg fiber are the same as those used in Section 3.3.
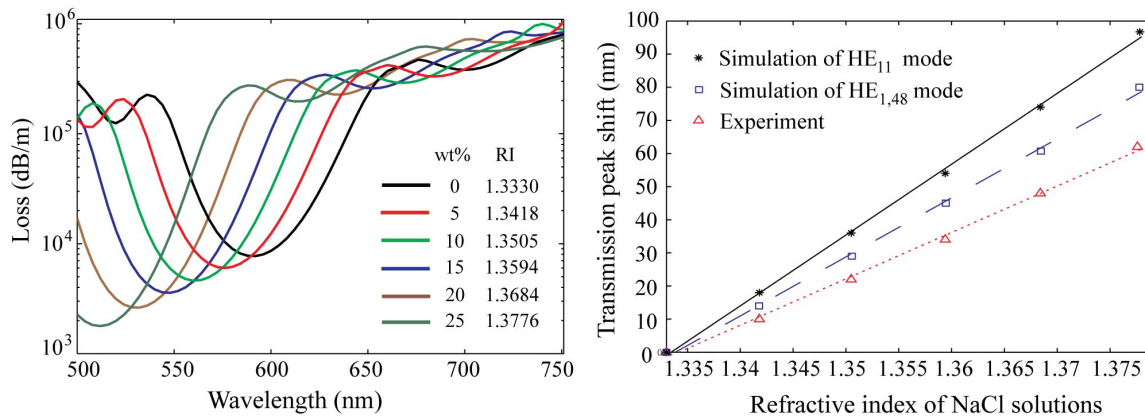
Figure 6. 1   (a) Simulated loss spectra of the $HE_{1, 48}$ mode of the Bragg fiber filled with different NaCl solutions. The refractive indices and concentrations of NaCl solutions are listed as the inset. (b) Spectral shifts of the fiber transmission peak obtained from the TMM simulations

(HE$_{11}$ and HE$_{1,48}$ mode) and the experimental measurements. The spectral shifts of the HE$_{11}$ mode and the experimental spectral shifts are calculated in Section 3.3.

In Fig.6.1 (a), we show the loss spectra of the HE$_{1,48}$ mode of the Bragg fiber filled with different NaCl solutions. A transmission band corresponding to a high-order bandgap of the Bragg fiber can be found in each spectrum. We note that these transmission spectra shift towards smaller wavelengths with increasing refractive index of the fiber core. In Fig.6.1 (b), we show linear fitting of the spectral shifts for the HE$_{11}$ mode (black solid line) and HE$_{1,48}$ mode (blue dash line), respectively. Besides, we also plot the spectral shifts (red dot line) of the experimental spectrum measured in Section 3.3. Apparently, the high-order HE$_{1,48}$ mode has smaller spectral shifts than those of the fundamental mode. In our experiment, the Bragg fiber with a large core may have hundreds of high-order modes excited. Therefore, we expect that the spectral shifts measured experimentally should be smaller than the ones of the simulated fundamental mode.

6.1.5 Temperature stability of the Bragg fiber refractometer

We now discuss how temperature variations would affect the performance of a Bragg fiber refractometer. We first note that an increase in temperature leads to both thermal expansion and refractive index changes of the fiber materials, thus shifting the transmission peak of the Bragg fiber. Therefore, temperature variations would bring an experimental noise to the Bragg fiber sensor and thus limit its resolution. In one of our previous papers [209], we have performed a TMM simulation to calculate the transmission spectra of a Bragg fiber at different temperatures. The Bragg fiber in this simulation has very similar structural parameters to those used in Chapter 3, except that its core material is PMMA rather than water. However, we note that the thermal-optic coefficients of water and PMMA are quite similar (κ_{H_2O}: -1.0×10^{-4} RIU/℃, κ_{PMMA}: -1.1×10^{-4} RIU/℃) [209]. Therefore, the simulation results (Fig.6.2) could be used as a proper reference to analogize the thermal properties of a water-filled Bragg fiber. From Fig.6.2, the transmission spectrum of a Bragg fiber shows a linear red-shift with increasing temperature. Besides, we find that 1 ℃ increment in temperature would shift the bandgap position by ~20 pm. To put this number into a perspective, the sensor temperature stability range is estimated to be 5 ℃, which would guarantee the bandgap shift caused thermal variations less than 0.1 nm.
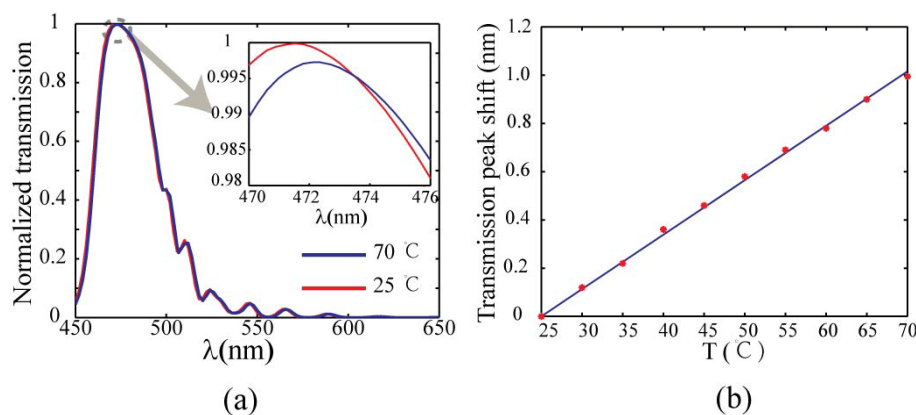
Figure 6. 2   (a) Simulated tranmission spectra of a solid-core Bragg fiber at 25 ℃ and 70 ℃. (b) Spectral positions of the transmission peak at various temperatures [209].

6.1.6   Influence of analyte absorption to the spectral-based detection strategy

The operating spectral range of the Bragg fiber refractometer is mainly determined by the bandgap position of a Bragg fiber. Currently, we routinely produce Bragg fibers with primary bandgaps covering the whole visible range. In this range, the liquid analytes (NaCl solutions) measured in Chapter 3 have relatively weak absorption that barely affects the transmission spectrum of the Bragg fiber. However, if a liquid sample with a strong absorption band (e.g. the olive oil [210] with absorption >800 dB/m at ~680 nm) is measured, the sensing properties of a Bragg fiber refractometer would be considerably changed. In what follows, we will discuss how absorption of an analyte would affect the refractive index sensing of a Bragg fiber refractometer with the following two assumptions:

1) If an analyte has a strong absorption band within the bandgap of a Bragg fiber, the transmitted intensity and transmission spectrum of the Bragg fiber could be considerably changed due to the analyte absorption. From Chapter 3, we note that Bragg fibers guide by bandgap effect. The light within the bandgap of a Bragg reflector is confined within the fiber core, and its loss is affected by radiation loss of the fiber and absorption of the liquid analyte filling the fiber. Therefore, if we use an analyte (such as the olive oil reported in Ref. [210]) with a strong absorption band in the bandgap, the transmission peak position could be changed due to the analyte absorption. In this case, additional simulations should be carried out to characterize the guiding and sensing properties of the Bragg fiber refractometer.

2) If the absorption band of an analyte is outside of or at the edges of the bandgap of a Bragg fiber, the analyte absorption would not affect the sensing properties of the Bragg fiber refractometer. In this case, the transmission band of the Bragg fiber is hardly affected by the absorption of an analyte, so we can still detect variations in refractive index of the fiber core by sensing spectral shifts of the fiber transmission peak. Besides, we note the Bragg fiber refractometer may also be used to measure the strength of the analyte absorption as a function of the analyte concentration, which potentially enables the Bragg fiber refractometer for simultaneous sensing of both real part and imaginary part (absorption) of the analyte refractive index.

6.1.7   Spectral-based detection strategy and amplitude-based detection strategy
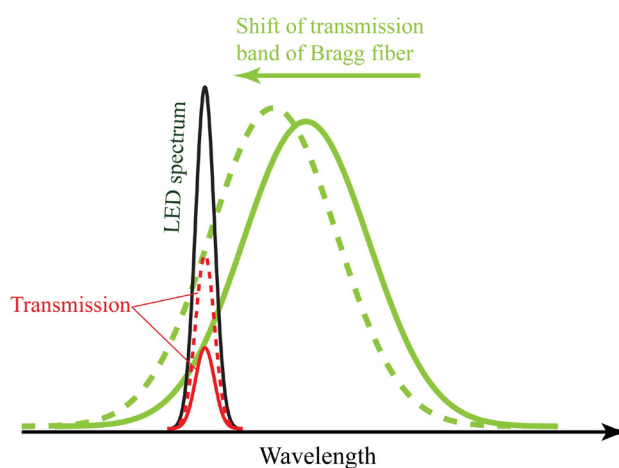
Figure 6. 3   Converting spectral shifts in the bandgap position into intensity variations in the fiber transmission spectrum [205]

We now discuss two potential experimental configurations that integrate liquid-core Bragg fibers into a practical product that is suitable for scientific and industrial sensing applications. In the first configuration, we integrate a coiled liquid-core Bragg fiber, the opto-fluidic blocks, a broadband (white) LED and a miniature spectrometer (e.g. the Bragg fiber spectrometer with a CCD or a Maya2000 from OCEAN-OPTICS [208]) together into a compact sensing system. Both the LED and spectrometer can be simply butt-coupled to the Bragg fiber. This relatively complex system operates using spectral-based detection modality and offers highest resolution and stability. In the second configuration, we adopt the amplitude-based detection modality that was proposed in [205]. Particularly, as a light source we use a LED with emission spectrum that is

much narrower than the bandgap of a liquid core Bragg fiber. As a detector we use a single photodiode. Changes in the analyte refractive index result in spectral shifts of the fiber bandgap, and consequently lead to changes in the detected transmission intensities as demonstrated in Fig.6.3. This configuration, though more prone to noise (e.g., intensity fluctuations in a light source), is, nevertheless, attractive due to its simplicity.

6.1.8   Potential applications of the Bragg fiber refractometer

We now propose several potential applications of the liquid-core Bragg fiber sensors. Firstly, these sensors can be used to monitor analyte concentrations in solutions. For example, glucose solutions (syrup) that are commonly used in food production and medical products have refractive indices monotonically dependent on the glucose concentration. Considering the resolution of the Bragg fiber sensor to be 7×10^{-5} RIU, we conclude that this sensor is able to measure variations in the concentration of glucose down to 0.05% by weight. Secondly, magneto-optic properties of magnetic fluids can be monitored using our Bragg fiber sensor. A well-known effect in magnetic fluids (e.g. Fe_3O_4-nanoparticle fluid) is the dependence of their refractive index on the external magnetic field. A Bragg fiber filled with the Fe_3O_4-nanoparticle fluid can be used to precisely monitor the fluid refractive index, and, as a consequence, to monitor the strength of the local magnetic field. According to Ref. [206], applying a magnetic intensity of ~1.7 kOe to a Fe_3O_4-based solution (weight concentration: 1.2mg/L) results in a refractive index variation of 0.023 RIU. Thus, ferrofluid-core Bragg fiber can be used as magnetic field sensors with a sensitivity of ~20 nm/kOe, which is comparable to the sensitivity of other magneto-optical sensors based on MOFs and fiber interferometers [207]. The main advantage of using our liquid-filled Bragg fibers in magnetic field sensors is the fact that the resolution of such sensors is virtually independent of the fiber length. This is important as Fe_3O_4-based fluid (translucent fluid) features relative high scattering loss, thus limiting sensor length to several centimeters. Thirdly, liquid-core Bragg fiber sensors can be used to monitor capillary electrophoresis dynamics. Capillary electrophoresis is a technique that is frequently used in biological research and pharmaceutical industry where separation of ionic species in electrolytic solutions is required. During capillary electrophoresis, analyte local refractive index and absorption become time dependent, which can be monitored optically when using Bragg-fibers as capillaries. Finally, Bragg fiber sensors can be simply used as absorption-based sensors for bio- and chemical

detection. Compared to other absorption-based sensors that use "leaky modes" of capillaries, the Bragg fibers offer much lower propagation losses, thus enabling longer sensing lengths and, hence, higher sensitivities.

6.2 Solid-core Bragg fiber bundle spectrometer

The solid-core Bragg fiber bundle spectrometer, presented in Chapter 4, features a simple structure that uses a bundle of 100 fibers and a monochrome CCD camera. The test spectrum filtered by the Bragg fiber bundle is then converted into an intensity image that is registered by the monochrome CCD camera. A transmission matrix algorithm is then used to associate the CCD intensity image to the test spectrum via pseudoinversion of a transmission matrix obtained experimentally from the calibration measurement. Experimental results show that Bragg fiber bundle spectrometer can efficiently reconstruct the center position of a test spectrum within several percent of its true value regardless of the peak position and width. Moreover, although the bandgap size of the individual Bragg fibers in the bundle is typically larger than 60 nm, the resolution of the fiber spectrometer is ~20-30 nm. Finally, a two-step drawing technique can be used to fabricate an all-fiber spectrometer. Overall, the main advantages of the Bragg fiber bundle spectrometer include low cost, the lack of moving parts, simultaneous acquisition of all the spectral components, high degree of integration, and simplicity of operation.

6.2.1 All-fiber Bragg fiber spectrometer system

The Bragg fiber bundle spectrometer potentially can be developed into an all-fiber spectrometer system that has the advantages such as small footprint, simple structure and the ease of integration with other fiber-based devices. Although the experimental setup demonstrated in Fig. 4.2 used several lenses to compress the image of the fiber bundle in order to make it match the size of the CCD sensor, we note these lenses could be removed from the setup. For example, we can taper the fiber bundle, so that the output end of the fiber bundle can be butt-coupled to the CCD sensor. Besides, in Chapter 5, we integrate the liquid-core Bragg fiber sensor to the solid-core Bragg fiber spectrometer to constitute a fiber-based spectroscopic system. In the setup of this system, we used two objectives for input- and output- coupling of the liquid-core Bragg fiber. We also note that these objectives can be removed from the setup. For example, a light source with a fiber tail can be used to directly butt-couple light into the liquid-core Bragg fiber, and then

the transmitted light of liquid-core Bragg fiber can be directly launched to the fiber bundle spectrometer via free-space coupling. In this case, a real "all-fiber" refractometer system could be developed. We expect that in the near future one could potentially develop an all-fiber sensor system by directly splicing different fiber-based components such as the light deliver fiber, the fiber refractometer and the fiber-based spectrometers, which would be a very interesting proposition.

6.2.2   Throughput of the Bragg fiber bundle

Among disadvantages of the Bragg fiber bundle spectrometer we note its relatively small light throughput. This is because the test light is physically divided into N parts that are then guided by the individual Bragg fibers. Almost 50% of light is currently lost by scattering from the interstitial regions between the Bragg fibers. Moreover, individual Bragg fibers transmit at most 30-50% of light as out-of-the bandgap spectral components are lost to radiation in the first several centimeters of propagation along the fibers. As a result, the overall throughput of a fiber bundle is estimated to be ~10-25% depending on the spectral content of the test signal.

6.2.3   Analysis of the experimental noises in the fiber spectrometer system

As shown in Chapter 4, the resolution of the Bragg fiber bundle spectrometer is strongly affected by the experimental noises present in the fiber spectrometer system. These experimental noises may come from several sources. Firstly, the background light in the experimental environment and intensity fluctuations of the light sources would bring noises. Particularly, we experimentally measured the background light noise to be smaller than 1 unit in the 8-bit coding (noise level: $1/256 = 0.39\%$). Note that this noise could be further suppressed by providing an optical isolation of the fiber bundle from the experimental environment. Besides, the light sources (halogen lamp and supercontinuum) used in the calibration measurements and the spectral reconstruction measurements have ~2% fluctuation in their output intensity, which also constitutes an experimental noise. Note that this noise can be minimized by averaging multiple frames of the test image taken by the CCD sensor. In our experiment, we used an Opteon monochrome CCD sensor that inherently integrates a "multi-frame" function in its operation software. Thus, we believe that the noise from the light source intensity fluctuations is greatly minimized.

Moreover, the experimental noises may also come from the monochrome CCD sensor. These noises include photon noise (shot noise) and quantization noise (analogy-to-digital conversion noise) of the CCD sensor. Photon noise results from the inherent statistical variations in the arrival rate of photons incident to each pixel of the CCD [211]. For a single pixel in the CCD, the number of incident photons during a fixed exposure time generally follows a Poisson statistics; therefore, the amplitude of photon noise on each pixel is considered as the square-root of the intensity (grey-scale level) registered by the pixel. Note that the photon noise can be also greatly reduced by averaging multiple frames of a test image. Besides, as mentioned in Section 4.5, the contribution of quantization noise is 0.1%, and this noise can be further reduced by using a CCD with a higher bit depth (e.g. 12-bit or 16-bit CCD).

We find that the biggest contribution to the experimental noise is caused by the changing illumination condition on the fiber bundle input facet. For example, in the calibration measurement, the incoming light comes from a monochromator-based source, and is shaped by the exit slit of the monochromator (Section 4.3.2); however, in the spectral reconstruction measurement, the incoming test light comes from a halogen lamp, and is then spatially shaped by the aperture of the optical filters (Section 4.4). In these two measurements, the illumination condition on the fiber bundle (especially fiber bundle with a large diameter) would be different due to the different spatial intensity distributions of the incoming light. This would bring noise to the spectrometer by introducing errors into the transmission matrix algorithm. It is difficult to directly measure the strength of this noise. However, from the noise analysis results shown in Fig.4.7 and considering the contributions from all other noises, we estimate that the changing illumination condition on the fiber bundle facet may contribute to an experimental noise with the amplitude of 8-10% of the test signal. An obvious remedy to reduce this noise is to reduce the diameter of the fiber bundle. We, therefore, proposed a two-step drawing method (in Section 4.6), that allows to fabricate a Bragg fiber bundle with a small diameter and a large number of Bragg fibers. As the future work of this project, we will focus on the perfection of this two-step drawing technique. Ideally, we expect to draw a fiber bundle that has a small diameter (e.g., <1 mm) and includes many Bragg fibers with complementary bandgaps. This allows more repeatable coupling conditions that would translate directly into precision of spectral reconstructions. We expect that by minimizing the experimental noises present in the spectrometer system, the resolution of this Bragg fiber spectrometer could be significantly improved.

6.2.4   SVD method for spectral reconstruction

To reconstruct a test spectrum, we need to calculate a pseudoinverse of the transmission matrix (matrix T) obtained from the calibration measurement. We note that matrix T is highly ill-conditioned (almost degenerate) due to the similarity of the transmission spectra of the Bragg fibers in the fiber bundle. For such an ill-conditioned system, even a small amount of experimental noise would introduce considerably large errors to the reconstructed spectra, if we use full-rank T in the spectral reconstruction algorithm (See Section 4.5). Therefore, we have to resort to a low-rank approximation of T in order to reduce the degree of ill-conditioning of T. As demonstrated in Section 4.3.3, we employ a SVD algorithm to calculate the low-rank approximation of T and the corresponding low-rank pseudoinverse. By minimizing the number of singular values used in the SVD algorithm, the error in the spectral reconstruction of a test spectrum could be considerably reduced, which is confirmed by our experimental results as well as the noise analysis shown in Section 4.5. Finally, we note that the SVD algorithm is not the only option for calculating the low-rank pseudoinverse of a matrix. Alternative methods such as the QR decomposition method [212] (also called QR factorization) could also be used. In this thesis, we only used the SVD algorithm due to its simplicity.

6.2.5   Potential applications of the Bragg fiber bundle spectrometer

Due to the advantages of the fiber bundle spectrometers such as low cost, short response time, simple structure, and the possibility of mass production, the Bragg fiber spectrometers may find their niche markets in a variety of scientific and industrial applications where rapid, low-resolution detection is required. Firstly, we note that the Bragg fiber bundle spectrometer can be naturally integrated into various fiber-based bio- and chemical sensors in order to replace traditional grating-based spectrometers and to enhance overall system integration and reliability. As a practical example, in this thesis we presented an all-fiber sensor operating on the spectral-based detection modality for monitoring of the salt concentration in aqueous solutions. Besides, the Bragg fiber bundle spectrometer could be potentially integrated into a machine vision system. For example, in Fig.6.4, we show two machine vision systems; one is used for color recognition [213], and the other is used to detect the "under-filled" bottles in a beverage production line [214]. It is possible to use the Bragg fiber bundle spectrometer to replace the delicate colorful CCD cameras in these systems. Note that the Bragg fiber spectrometer could adopt a low-cost webcam

for optical detection, which would lower significantly the cost of a machine vision system using this fiber spectrometer.

(a)   (b)

Figure 6. 4   Machine vision system for (a) color recognition [213] and (b) detection of "under-filled" bottles in a beverage production line [214].

REFERENCES

1. Carl Zeiss AG 1989 Abbe Refraktometer B (Oberkochen, Germany).

2. D. A. Krohn, Fiber Optic Sensors: Fundamentals and Applications, 3rd Edition, Instrument Society of America, North Carolina, USA, 1992.

3. E. Udd, and W. B. Spillman Jr, Fiber Optic Sensors: An introduction for Engineers and Scientist, 2nd Edition, John Wiley & Sons Inc, Hoboken, New Jersey, 2011.

4. M. Skorobogatiy, "Resonant bio- chemical sensors based on Photonic Bandgap waveguides and fibers" in Optical Guided-wave Chemical and Biosensors II, Springer Series on Chemical Sensors and Biosensors 8, edited by A. Lakhtakia and Z. Mohammod, Springer-Verlag Berlin Heidelberg, 43-72, 2010.

5. http://www.forc-photonics.ru/en/fiber_optics_devices/fiber%20refractometers/1/116/

6. M. Sheeba, M. Rajesh, C. P. G. Vallabhan, V. P. N. Nampoori, and P. Radhakrishnan, "Fibre optic sensor for the detection of adulterant traces in coconut oil," Measurement Science and Technology, **16**, 2247-2250, 2005.

7. A. Mukherjee, D. Munsi, V. Saxena, R. Rajput, P. Tewari, V. Singh, A. K. Ghosh, J. John, H. Wannare, and P. Gupta-Bhaya, "Characterization of a fiber optic liquid refractive index sensor," Sensors and Actuators: B, **145**, 265-271, 2010.

8. A. Banerjee, S. Mukherjee, R. K. Verma, B. Jana, T. K. Khan, M. Chakroborty, R. Das, S. Biswas, A. Saxena, V. Singh, R. M. Hallen, R. S. Rajput, P. Tewai, V. Singh, A. K. Ghosh, J. John, H. Wannare, and P. Gupta-Bhaya, "Fiber optic sensing of liquid refractive index," Sensors and Actuators: B, **123**, 594-605, 2007.

9. J. Villiatoro, D. Monzoon-Hernadex, and D. Talavera, "High resolution refractive index sensing with cladded multimode tapered optical fiber," Electronic Letters, **40**, 106-107, 2004.

10. A. Kumar, T. V. B. Subrahmonium, A. D. Sharma, K. Thyagarajan, B. P. Pal, and I. C. Goyal, "Novel refractometer using a tapered optical fiber," Electronic letters, **20**, 534, 1984.

11. A. Leung, P. M. Shankar, and R. Mutharasan, "A review of fiber-optic biosensors," Sensors and Actuators: B, **125**, 688-703, 2007.

12. G. Raizada and B. P. Pal, "Refractometers and tunable components based on side-polished fibers with multimode overlay waveguides: role of the superstrate," **21**, 399-401, 1996.

13. K. Schroeder, W. Ecke, R. Mueller, R. Willsch, and A. Andreev, "A fibre Bragg grating refractometer," Measurement Science and Technology, **12**, 757-764, 2001.

14. X. Fang, C. R. Liao, and D. N. Wang, "Femtosecond laser fabricated fiber Bragg grating in microfiber for refractive index sensing," Optics Letters, **35**, 1007-1009, 2010.

15. W. Liang, Y. Huang, Y. Xu, R. K. Lee, and A. Yariv, "Highly sensitive fiber Bragg grating refractive index sensors," Applied Physics Letters, **86**, 151122, 2005.

16. Q. Wang, and G. Farrel, "All-fiber multimode-interference-based refractometer sensor: proposal and design," Optics Letters, **31**, 217-319, 2006.

17. Y. Jung, S. Kim, D. Lee, and K. Oh, "Compact three segmented multimode fibre modal interferometer for high sensitivity refractive-index measurement," Measurement Science and Technology, **17**, 1129-1133, 2006.

18. R. X. Gao, W. J. Wu, Y. Y. Wang, Q. Wang, F. Zhao, and S. L. Qu, "Design and fabrication of SMS fiber refractometer for liquid," Sensors and Actuators: A, **179**, 5-9, 2012.

19. Q. Wu, Y. Semenova, B. Yan, Y. Ma, P. Wang, C. Yu, and G. Farrel, "Fiber refractometer based on a fiber Bragg grating and single-mode-multimode- single-mode fiber structure," Optics Letters, **36**, 2197-2199, 2011.

20. K. Juan, X. Dong, C. Zhao, and Y. Zhao, "A Sagnac loop sensor for refractive index measurement", in Photonics and Optoelectronics (SOPO), **2011**, Symposium on, pp. 1-4, IEEE, 2011.

21. P. Lu, J. Harris, X. Wang, G. Lin, L. Chen, and X. Bao, "Tapered-fiber-based refractive index sensor at an air-solution interface," Applied Optics, **51**, 7368-7373, 2012.

22. L. Rindorf, P. E. Hoiby, J. B. Jensen, L. H. Pedersen, O. Bang, and O. Geschke, "Towards biochips using microstructured optical fiber sensors," Analytical and Bioanalytical Chemistry, **385**, 1370-1375, 2006.

23. J. Sun, and C. C. Chan, "Photonic bandgap fiber for refractive index measurement," Sensors and Acutuators: B, **128**, 46-50, 2007.

24. B. Lienert, J. Porter, and S. K. Sharma, "Simultaneous measurement of spectra at multiple ranges using a single spectrometer," Applied Optics, **48**, 4762-4766, 2009.

25. http://www.oceanoptics.com/Products/usb4000.asp

26. H. Qu, B .Ung, I. Syed, N. Guo, and M. Skorobogatiy, "Photonic bandgap fiber bundle spectrometer," Applied Opitcs, **49**, 4791-4798, 2010.

27. K. S. Feder, P. S. Westbrook, J. Ging, P. I. Reyes and G. E. Carver, "In-fiber spectrometer using tilted fiber grating," IEEE Photonic Technology Letters, **15**, 933-935, 2003.

28. P. St. J. Russell, and R. Ulrich, "Grating-fiber coupler as a high-resolution spectrometer," Optics Letters, **10**, 291, 1985.

29. B. Redding, and H. Cao, "Using a multimode fiber as a high-resolution low-loss spectrometer," Optics Letters, **37**, 3384-3386, 2012.

30. J. Rheims, J. Koser, and T. Wriedt, "Refractive-index measuments in the near-IR using an Abbe refractometer," Meas. Sci. Technol. **8**, 601, 1997.

31. P. P. Herrmann, "Determination of thickness, refractive index, and dispersion of waveguiding thin films with an Abbe refractometer," **19**, 3261, 1980.

32. http://www.bellinghamandstanley.com/general_pdfs/Abbe_Refractometers.pdf

33. C. T. Cotton, H. Falls, J. M. Sabin, T. E. R. Batavia, "Brake check handheld refractometer," United States Patent, 5969808, Oct, 19, 1999.

34. http://www.refractometer.pl/, accessible in Feb 26, 2013.

35. C. Pulfrich, *Zeitschrift für Instrumentenkunde.* **8**, 47, 1888.

36. C. Pulfrich (1890) *das Total reflectometer und das Refractometer für Chemiker etc.* W. Engelmann, Leipzig.

37. E. Moreels, C. de Greef, R. Finsy, "Laser light refractometer," Applied optics, **23**, 3010, 1984.

38. S. C. Zilio, "A simple method to measure critical angles for high-sensitivity differential refractometry," Optics express, **20**, 1862, 2012.

39. J. V. Hughes, "A new precision refractometer," Journal of Scientific Instruments. **18**, 234-237, 1941.

40. P. R. Cooper, "Refractive-index measurement of paraffin, a silicone elastomer, and an epoxy resin over the 500-1500-nm spectral range," Applied Optics, **21**, 3413-3415, 1982.

41. P. R. Cooper, "Refractive-index measurement of liquids used in conjunction with optical fibers," Applied Optics, **22**, 3070-3072, 1983.

42. I. D. Nikolov, and C. D. Ivanov, "Optical plastic refractive measurements in the visible and the near infrared regions," Applied Optics, **39**, 2067, 2000.

43. S. Nemoto, "Measurement of the refractive index of liquid using laser beam displacement," Applied Optics, **31**, 6690, 1992.

44. D. D. Jenkins, "Refractive indices of solution," Physics Education, **17**, 82-83, 1982.

45. J. M. Starnaud, J. Ge, J. Orbriot, T. K. Bose, and Ph. Marteau, "An accurate method for refractive index measurements of liquids using two Michelson laser interferometers," Review of Scientific Instruments, **62**, 1411, 1991.

46. P. N.Yi, and R. C. MacDonald, "Analytical applications of a recording interference refractometer," Analytical Chemistry, **51**, 163-165, 1979.

47. S. R. Kachiraju, and D. A. Gregory, "Determining the refractive index of liquids using a modified Michelson interferometer," Optics & Laser Technology, 44**,** 2361-2365, 2012.

48. K. D. Singer, M. S. Merlin, S. J. Lalama, and A. F. Garito, "Interferometric refractometer for measuring the relative refractive index of two liquids," Review of Scientific Instruments, **53**, 202, 1982.

49. M. S. Shumate, "Interferometric Measurement of large indices of refraction," Applied Optics, **5**, 327-331, 1966.

50. A. Lassila, P, Tallgren, K. Riski, and E. Ikonen, "Interferometric refractometer with a viariable-length vacuum cylinder," SPIE. **3477**, 54, 1998.

51. J. J. Fendley, "Measurement of refractive index using a Michelson interferometer," Physics Education, **17**, 209, 1982.

52. G. D. Gillen, and S. Guha, "Refractive index measurements of zinc germanium diphosphide at 300 and 77 K by use of a modified Michelson interferometer," Applied Optics, **43**, 2054-2058, 2004.

53. C. A. Proctor, "Index of refraction and dispersion with the interferometer," Physics Review, **24**, 195-201, 1907.

54. M. Musso, R. Aschauer, A. Asenbaum, C. Vasi, and E. Wilhelm, "Interferometric determination of the refractive index of liquid sulphur dioxide," Measurement Science and Technology, **11**, 1714-1720, 2000.

55. S. D. Woodruff, and E. S. Yeung, "Double-beam Fabry-perot Interferometry as a refractive index detector in liquid chromatography," Analytical Chemistry, **54**, 2124-2125, 1982

56. H. J. Choi, H. H. Lim, H. S. Moon, T. B. Eom, J. J. Ju, and M. Cha, "Measurement of refractive index and thickness of transparent plate by dual-wavelength interference," Optics Express, **18**, 9429, 2010.

57. G. Coppola, P. Ferraro, M. Iodice, and S. D. Nicola, "Method for measuring the refractive index and the thickness of transparent plates with a lateral-shear, wavelength-scanning interferometer," Applied Optics, **42**, 3882-3887, 2003.

58. H. Shao, W. Wang, S. E. Lana, and K. L. Lear, "Optofluidic intracavity spectroscopy of canine lymphoma and lymphocytes," IEEE Photonic Technology Letters, **20**, 493-495, 2008.

59. G. D. Gillen, and S. Guha, "Use of Michelson and Fabry-Perot interferometry for independent determination of the refractive index and physical thickness of wafers," Applied Optics, **44**, 344-347, 2005.

60. T. Schubert, N. Haase, H. Kuck, R. Gottfried-Gottfried, "Refractive index measurements using an integrated Mach-Zehnder Interferometer," Sensors and Acutuators A, **60**, 108-112, 1997.

61. K. Betzler, A. Grone, N. Schmidt, and P. Voigt, "Interferometer measurement of refractive indices," Review of Scientific Instruments, **59**, 652, 1988.

62. S. A. Maier, Plasmonics: Fundamentals and Applications, Springer-Verlag New York Inc, New York, 2007.

63. A. Hassani, M. Skorobogatiy, "Surface plasmon resonance-like integrated sensor at terahertz frequencies for gaseous analytes," Optics Express, 16, 20206, 2008.

64. B. D. Gupta and R. K. Verma, "Surface plasmon resonance-based fiber optic sensors: principle, probe design, and some applications," Journal of Sensors, **2009**, 979761, 2009.

65. J. Homola, S. S. Yee, G. Gauglitz, "Surface plasmon resonance sensors: review," Sensors and Actuators: B, **54**, 3-15, 1999.

66. R. V. Nair, and R. Vijaya, "Photonic crystal sensors: an overview," Progress in Quantum Electronics, **34**, 89-134, 2010.

67. D. F. Dorfner, T. Hurlimann, T. Zabel, L. H. Frandsen, and G. Abstreiter, "Silicon photonic crystal nanostructures for refractive index sensing," Applied Physics Letters, **93**, 181103, 2008.

68. C. Kang, C. T. Phare, Y. A. Vlasov, S. Assefa, and S. M. Weiss, "Photonic crystal slab sensor with enhanced surface area," Optics Express, **18**, 27930, 2010.

69. Y. Liu, and H. W. M. Salemink, "Photonic crystal based all optical on chip sensor," Optics Express, **20**, 19912, 2012.

70. E. C. I. Ryckebosch, M. A. Dundar, R. Notzel, F. Karouta, L. J. VanIJzendoorn, and R. W. van der Heijden, "Refractive index sensing with an InGaAsP photonic crystal membrane cavity by means of photoluminescence," Proceedings Symposium IEEE Photonics Benelux Chapter, **2009**, Bressels, 45-48, 2009.

71. A. D. Falco, L. O'Faolain, and T. F. Krauss, "Chemical sensing in slotted photonic crystal heterostructure cavities," Applied Physics Letters, **94**, 063503, 2009.

72. J. Jagerska, N. L. Thomas, H. Zhang, Z. Diao, and R. Houdre, "Refractive index gas sensing in a hollow photonic crystal cavity," Proceedings of Transparent Optical Networks (ICTON), 2012 12th International Conference, Munich, Tu. A2.2, 2010.

73. J. Jagerska, N. L. Thomas, H. Zhang, Z. Diao, and R. Houdre, "Refractive index sensing with an air-slot photonic crystal nanocavity," Optics Letters, **35**, 2523, 2010.

74. T. Lu, Y. Hsiao, W. Ho, and P. Lee, "Photonic crystal heteroslab-edge microcavity with high quality factor surface mode for index sensing," Applied Physics Letters, **94**, 141110, 2009.

75. J. Wu, D. Day, M. Gu, "A microfluidic refractive index sensor based on an integrated three dimentional photonic crystal," Applied Physics Letters, **92**, 071108, 2008.

76. N. Skivesen, A. Tetu, M. Kristensen, J. Kjems, L. H. Frandsen and P. I. Borel, "Photonic crystal waveguide biosensor," Optics Express, **15**, 3169, 2007.

77. F. Vollmer, and L. Yang, "Label-free detection with high-Q microcavities: a review of biosensing mechanisms for integrated devices," Nanophotonics, **1**, 267-291, 2012.

78. X. Fan, I. M. White, S. I. Shopova, and H. Zhu, "Sensitive optical biosensors for unlabeled targets: A review," Analytica Chimica Acta, **620**, 8-26, 2008.

79. C-Y. Chao, W. Fung, and L. J. Guo, "Polymer microring resonators for biochemical sensing applications," IEEE Journal of Selected Topics in Quantum Electronics, **12**, 134, 2006.

80. A. Yalcin, K. C. Popat, J. C. Aldridge, T. A. Desai, J. Hryniewicz, N. Chbouki, B. E. Little, O. King, V. Van, S. Chu, D. Gill, M. S. Mnlu, and B. B. Goldberg, "Optical sensing of biomolecules using microring resonators," IEEE Journal of Selected Topics in Quantum Electronics, **12**, 148, 2006.

81. E. Krioukov, D. J. W. Klunder, A. Driessen, J. Greve, and C. Otto, "Sensor based on an integrated optical microcavity," Optics Letters, **27**, 512-514, 2002.

82. G-D. Kim, G-S. Son, H-S. Lee, K-D. Kim, and S-S. Lee, "Refractometric sensor utilizing a vertically coupled polymeric microdisk resonator incorporating a high refractive index overlay," Optics Letters, **34**, 1048-1050, 2009.

83. M. L. Gorodetsky, A. A. Savchenkov, and V. S. Ilchenko, "Ultimate Q of Optical microsphere resonators," Optics Letters, **21**, 453-455, 1996.

84. N. M. Hanumegowda, I. M. White, C. J. Stica, B. C. Patel, H. Oveys, and X. Fan, "Development of label-free microsphere optical resonator bio/chemical sensors," Proc. of SPIE, **6004**, 600401, 2005.

85. N. M. Hanumegowda, I. M. White, C. J. Stica, B. C. Patel, H. Oveys, and X. Fan, "Refractometric sensors based on microsphere resonators," Applied Physics Letters, **87**, 201107, 2005.

86. I. Teraoka, and S. Arnold, "Enhancing the sensitivity of a whispering-gallery mode microsphere sensor by a high-refractive-index surface layer," Journal of Optical Society of America B, **23**, 1434, 2006.

87. O. Gaathon, J. C. Viskota, M. Mihnev, I. Teraoka, and S. Arnold, "Ehancing sensitivity of a whispering gallery mode biosensor by subwavelength confinement," Applied Physics Letters, **89**, 223901, 2006.

88. C. Kim, and C. B. Su, "Measurement of the refractive index of liquids at 1.3 and 1.5 micron using a fibre optic Fresnel ratio meter," Measurement Science and Technology, **15**, 1683-1686, 2004.

89. M. S. Meyer, and G. L. Eesley, "Optical fiber refractometer," Review of Scientific Instruments, **58**, 2047, 1987.

90. D. Monzon-Hernandez, J. Villatoro, D. Luna-moreno, "Miniature optical fiber refractometer using cladded multimode tapered fiber tips," Sensors and Actuators: B, **110**, 36-40, 2005.

91. P. Nath, "Non-intrusive refractometer sensor," Pramana-Journal of Physics, **74**, 661-668, 2010.

92. K. Cherif, S. Hleli, A. Abdelghani, N. Jaffrezic-Renault and V. Matejec, "Chemical detection in liquid media with a refractometric sensor based on a multimode optical fibre," Sensors, **2002**, 195, 204, 2002

93. C. Sui, P. Wu, G. Wei, "A fiber optic evanescent wave sensor for measuring refractive index change of liquids," Progress in Electromagnetics Research Symposium (PIERS) Proceedings, Cambridge, USA, 790, 2010.

94. A. Ladicicco, D. Paladino, S. Campopiano, W. J. Bock, A. Cutolo, and A. Cusano, "Evanescent wave sensor based on permanently bent single mode optical fiber," Sensors and Actuators: B, **155**, 903-908, 2011.

95. T. Takeo, and H. Hattori, "Skin hydration state estimation using a fiber-optic refractometer," Applied Optics, **33**, 4267-4272, 1994.

96. A. K. Sharma, R. Jha, and B. D. Gupta, "Fiber-optic sensors based on surface plasmon resonance: a comprehensive review," IEEE Sensors Journal, **7**, 1118, 2007.

97. A. Hassani and M. Skorobogatiy, "Design criteria for microstructured-optical-fiber-based surface-plasmon-resnoance sensors," Journal of the Optical Society of America B, **24**, 1423, 2007.

98. Y. Lin, "Characteritics of optical fiber refractive index sensor based on surface plasmon resonance," Microwave and Optical Technology Letters, **55**, 574, 2013.

99. N. Cennamo, D. Massarotti, L. Conte, and L. Zeni, "Low cost sensors based on SPR in a plastic optical fiber for biosensor implementation," Sensors, **11**, 11752-11760, 2011.

100. P. Bhatia, and B. D. Gupta, "Surface-plasmon-resonance-based fiber-optic refractive index sensor: sensitivity enhancement," Applied Optics, **50**, 2032, 2011.

101. J. H. Ahn, T. Y. Seong, W. M. Kim, T. S. Lee, I. Kim and K. Lee, "Fiber-optic waveguide coupled surface plasmon resonance sensor," Optics Express, **20**, 21729, 2012.

102. D. Monzon-Hernandez, and J. Villatoro, "High-resolution refractive index by means of a multiple-peak surface plasmon resonance optical fiber sensor," Sensors and Actuators: B, **115**, 227-231, 2006.

103. P. Englebienne, A. V. Hoonacker, and M. Verhas, "Surface plasmon resonance: principles, methods and applications in biomedical sciences," Spectroscopy, **17**, 255-273, 2003.

104. Y. Chen, R. Zheng, Y. Lu, P. Wang, and H. Ming, "Fiber-optic surface plasmon resonant sensor with low-index anti-oxidation coating," Chinese Optics Letters, **9**, 100605, 2011.

105. A. P. Zhang, S. Gao, G. Yan, and Y. Bai, "Advances in optical fiber Bragg grating sensor technology," Photonic Sensors, **2**, 1-13, 2012.

106. D. A. Pereira, O. Frazao, J. L. Santos, "Fiber Bragg grating sensing system for simultaneous measurement of salinity and temperature," Optical Engineering, **43**, 299, 2004.

107. A. Asseh, S. Sandgren, H. Ahlfeldt, B. Sahlgren, R. Stubbe, and G. Edwall, "Fiber optical Bragg grating refractometer," Fiber and Integrated Optics, **17**, 51-62, 1998.

108. A. N. Chryssis, S. M. Lee, S. B. Lee, S. S. Saini, and M. Dagenais, "High sensitivity evanescent field fiber Bragg grating sensor," IEEE Photonics Technology Letters, **17**, 1253, 2005.

109. A. Iadicicco, S. Campopiano, A. Cutolo, M. Giordano, and A. Cusano, "Nonuniform thinned fiber Bragg gratings for simultaneous refractive index and temperature measurements," IEEE Photonics Technology Letters, **17**, 1495, 2005.

110. A. Iadicicco, S. Campopiano, A. Cutolo, M. Giordano, and A. Cusano, "Refractive index sensor based on microstructured fiber Bragg grating," IEEE Photonics Technology Letters, **17**, 1250, 2005.

111. S. Lee, S. S. Saini, and M. Jeong, "Simultaneous measurement of refractive index, temperature, and strain using etched-core fiber Bragg grating sensors," IEEE Photonics Technology Letters, **22**, 1431, 2010.

112. Y. Ran, Y. Tan, L. Sun, S. Gao, J. Li, L. Jin, and B. Guan, "193nm Excimer laser inscribed Bragg gratings in microfibers for refractive index sensing," Optics Express, **19**, 18577, 2011.

113. Y. Zhang, B. Lin, S. C. Tjin, H. Zhang, G. H. Wang, P. Shum, and X. L. Zhang, "Refractive index sensing based on high-order mode reflection of a microfiber Bragg grating," Optics Express, **18**, 26345-26350, 2010.

114. C. F. Chan, C. Chen, A. Jafari, A. Laronche, D. J. Thomson, and J. Albert, "Optical fiber refractometer using narrowband cladding-mode resonance shifts," Applied Optics, **46**, 1142, 2007.

115. T. Guo, C. Chen, A. Laronche, and J. Albert, "Power-referenced and temperature-calibrated optical fiber refractometer," IEEE Photonics Technology Letters, **20**, 635, 2008.

116. T. Guo, H. Tam, P. A. Krug, and J. Albert, "Reflective tilted fiber Bragg grating refractometer based on strong cladding to core recoupling," Optics Express, **17**, 5736, 2009.

117. K. Zhou, Y. Lai, X. Chen, K. Sugden, L. Zhang, I. Bennion, "A refractometer based on a micro-slot in a fiber Bragg grating formed by chemically assisted femtosecond laser processing," Optics Express, **15**, 15848, 2007.

118. L. Rindorf, O. Bang, "Sensitivity of photonic crystal fiber grating sensors: biosensing, refractive index, strain, and temperature sensing," Journal of the Optical Society of America B, **25**, 310, 2008.

119. H. Tsuda, and K. Urabe, "Characterization of long-period grating refractive index sensors and their applications," Sensors, **9**, 4559-4571, 2009.

120. V. Bhatia, D. K. Compbell, T. D'Alberto, G. A. T. Eyck, D. Sherr, K .A. Murphy, R. O. Claus, "Standard optical fiber long-period gratings with reduced temperature sensitivity for strain and refractive index sensing," Proceedings of Optical Fiber Communication. OFC 97, FB1, 346-347, 1997.

121. V. Bhatia, T. D'Alberto, N. Zabaronick, and R. O. Claus, "Temperature- insensitive long-period gratings for strain and refractive index sensing," SPIE **3042,** 194, 1997.

122. Z. Yin, X. Zhang, Y. Liu, F. Pang, and T. Wang, "Refractive index sensitivity characteristics of fiber taper long-period grating," in Asia Communications and Photonics Conference, Guangzhou, China, AF4A, 2013.

123. A. Iadicicco, D. paladino, P. Pilla, S. Campopiano, A. Cutolo and A. Cusano, "Long period gratings in new generation optical fibers," Recent Progress in Optical Fiber Research, edited by M. Yasin, ISBN: 978-953-307-823-6, 2012.

124. G. Lin, P. Wu, E. Chang, Y. Wang, M. Fu, and W. F. Liu, "Liquid index sensor based on a multimode air-gap long period fiber grating," in 15th OptoElectronics and Communications Conference, Sapporo Convention Center, Japan, 9C4-6, 2010.

125. V. Bhatia, "Applications of long-period gratings to single and multi-parameter sensing," Optics Express, **4**, 457, 1999.

126. A. Kapoor, and E. K. Sharma, "Long period grating refractive-index sensor: Optical design for single wavelength interrogation," Applied Optics, **48**, G88, 2009.

127. J. Yang, L. Yang, C-Q. Xu, C. Xu, W. Huang, and Y. Li, "Long-period grating refractive index sensor with a modified cladding structure for large operational range and high sensitivity," Applied Optics, **45**, 6142, 2006.

128. S. Korposh, S. Lee, S. W. James and R. P. Tatam, "Refractive index sensitivity of fiber optic long period gratings with SiO_2 nanoparticle based mesoporous coating," in Proceedings of 21st International Conference on Optical Fiber Sensors, SPIE**7753**, 77539A-1, 2011.

129. S. M. Tripathi, E. Marin, A. Kumar, and J-P. Meunier, "Refractive index sensing characteristics of dual resonance long period gratings in bare and metal-coated D-shaped fibers," Applied Optics, **48**, G53, 2009.

130. B. H. Lee, Y. H. Kim, K. S. Park, J. B. Eom, M. J. Kim, B. S. Rho, and H. Y. Choi, "Interferometric fiber optic sensors," Sensors, **12**, 2467-2486, 2012.

131. J. L. Elster, M. E. Jones, M. K. Evans, S. M. Lenahan, and C. A. Boyce, "Optical fiber extrinsic Fabry-Perot interferometric (EFPI)-based biosensors," in Biomedical Diagnostic, Guidance and Surgical-Assist System II, Tuan Vo-Dinh, Warren S. Grndfest, SPIE **3911**, 105, 2000.

132. Y. Tian, W. Wang, N. Wu, X. Zou, C. Guthy, and X. Wang, "A miniature fiber optic refractive index sensor built in a MEMS-based microchannel," Sensors, **11**, 1078-1087, 2011.

133. Z. Ran, Y. Rao, J. Zhang, Z. Liu and B. Xu, "A miniature fiber optic refractive index sensor based on laser-machined Fabry-Perot interferometer tip," Journal of Lightwave Technology, **27**, 5426, 2009.

134. K. Zhou, Z. Yan, L. Zhang, and I. Bennion, "Refractometer based on fiber Bragg grating Fabry-Perot cavity embedded with a narrow microchannel," Optics Express, **19**, 11769, 2011.

135. T. Wei, Y. Han, Y. Li, H-L. Tsai, and H. Xiao, "Temperature-insensitive miniaturized fiber inline Fabry-Perot interferometer for highly sensitive refractive index measurement," Optics Express, **16**, 5764, 2008.

136. L. Mosquera, D. Saez-Rodriguez, J. L. Cruz, and M. V. Andres, "In-fiber Fabry-Perot refractometer assisted by a long-period grating," Optics Letters, **35**, 613, 2010.

137. C. Jesus, S. F. O. Silva, M. Castanheira, G. G. Aguilar, O. Frazao, P. A. S. Jorge and J. M. Baptista, "Interferometric fiber-optic sensor for acetic acid measurement," in proceedings of 20th International Conference on Optical Fiber Sensors, SPIE **7530**, 75031A, 2009.

138. D. J. J. Hu, Y. Wang, J. L. Lim, T. Zhang, K. B. Milenko, Z. Chen, M. Jiang, G. Wang, F. Luan, P. P. Shum, Q. Sun, H. Wei, W. Tong, and T. R. Wolinski, "Novel miniaturized Fabry-perot refractometer based on a simplified hollow-core fiber with a hollow-core silica sphere tip," IEEE Sensors Journal, **12**, 1239, 2012.

139. E. Cibula, and D. Donlagic, "In-line Fabry-Perot refractive index sensor," IEEE Photonics Technology Letters, **23**, 1609, 2011.

140. V. Zamora, A. Diez, M. V. Andres and B. Gimeno, "Refractometric sensor based on whispering gallery modes of thin capillaries," Optics Express, **15**, 12011, 2007.

141. X. D. Fan, I. M. White, H. Y. Zhu, J. D. Suter, H. Oveys, "Overview of novel integrated optical ring resonantor bio-chemical sensors," Proc. SPIE **6452**, 1-20, 2007.

142. I. M. White, H. Zhu, J. D. Suter, N. M. Hanumegowda, H. Oveys, M. Zourob, and X. Fan, "Refractometric sensors for lab-on-a-chip based on optical ring resonators, " IEEE Sensors Journal, **7**, 28, 2007.

143. I. M. White, H. Oveys, X. Fan, T. L. Smith, and J. Zhang, "Integrated multiplexed biosensors based on liquid core optical ring resonators and antiresonant reflecting optical waveguides," Applied Physics Letters, **89**, 191106, 2006.

144. I. M. White, H. Ovey, and X. Fan, "Liquid-core optical ring-resonator sensors," Optics Letters, **31**, 1319. 2006.

145. M. Sumetsky, R. S. Windeler, Y. Dulashko, and X. Fan, "Optical liquid ring resonator sensor," Optics Express, **15**, 14376, 2007.

146. T. Ling, and L. Guo, "A unique resonance mode observed in a prism-coupled micro-tube resonator sensor with superior index sensitivity," Optics Express, **15**, 17424, 2007.

147. N. M. Litchinitser, E. Poliakov, "Antiresonant guiding microstructured optical fibers for sensing applications," Applied Physic B, **81**, 347-351, 2005.

148. J. Sun, and C. C. Chan, "Refractive index measurement using a photonic crystal fiber," Optical Engineering **46**, 014402, 2007.

149. X. Yu, P. Shum, G. B. Ren, and N. Q. Ngo, "Photonic crystal fibers with high index infiltrations for refractive index sensing," Optics Communication, **281**, 4555-4559, 2008.

150. D. K. Wu, B. T. Kuhlmey, and B. J. Eggleton, "Ultrasensitive photonic crystal fiber refractive index sensor," Optics Letters, **34**, 322-324, 2009.

151. H. F. Xuan, W. Jin, J. Ju, H. L. Ho, M. Zhang, Y. B. Liao, "Low-contrast photonic bandgap fibers and their potential applications in liquid-base sensors," in 3rd European Workshop on Optical Fiber Sensors, Proc. SPIE **6619**, 661936, 2007.

152. K. J. Rowland, S. Afshar, A. Stolyarov, Y. Fink, and T. M. Monro, "Bragg waveguides with low-index liquid cores," Optics Express, **20**, 48, 2012.

153. H. Qu, and M. Skorobogatiy, "Liquid-core low-refractive-index-contrast Bragg fiber sensor," Applied Physics Letters, **98**, 201114, 2011.

154. H. Qu, B. Ung, M. Roze, and M. Skorobogatiy, "All photonic bandgap fiber spectroscopic system for detection of refractive index changes in aqueous analytes," Sensors and Acutators B, **161**, 235-243, 2012.

155. M. C. P. Huy, G. Laffont, Y. Frignac, V. Dewynter-Marty, P. Ferdinand, P. Roy, J. Blondy, D. Pagnoux, W. Blanc, and B. Dussardier, "Fiber Bragg grating photowrting in microstructured optical fibers for refractive index measurement, " Measurement Science and Technology, **17**, 992-997, 2006.

156. M. C. P. Huy, G. Laffont, V. Dewynter, P. Ferdinand, P. Roy, J. Auguste, D. Pagnoux, W. Blanc, and B. Dussardier, "Three-hole microstructured optical fiber for efficient fiber Bragg grating refractometer," Optics Letters, **32**, 2390, 2007.

157. M. C. P. Huy, G. Laffont, V. Dewynter, L. Labonte, P. Ferdinand, P. Roy, J. Auguste, D. Pagnoux, W. Blanc, and B. Dussardier, "Tilted fiber Bragg grating photowritten in microstructured optical fiber for improved refractive index measurement," Optics Express, **14**, 10359, 2006.

158. A. P. Zhang, G. Yan, S. Gao, S. He, B. Kim, J. Im, and Y. Chung, "Microfluidic refractive-index sensors based on small-hole microstructured optical fiber Bragg gratings," Applied Physics Letters, **98**, 221109, 2011.

159. X. Yu, P. Shum, and G. B. Ren, "Highly sensitive photonic crystal fiber-based refractive index sensing using mechanical long-period grating," IEEE Photonics Technology Letters, **20**, 1688, 2008.

160. X. Yu, Pshum, G. B. Ren, and Y. Zhang, "Refractive index sensing using mechanical long-period grating in photonic crystal fiber," in Conference of Photonics Global at Singapore, IPGC. 2008. 4781448, 2008.

161. L. Rindorf, and O. Bang, "Highly sensitive refractometer with a photonic-crystal fiber long-period grating," Optics Letters, 33, 563, 2008.

162. Z. He, Y. Zhu, and H. Du, "Long-period gratings inscribed in air- and water- filled photonic crystal fiber for refractometric sensing of aqueous solution," Applied Physics letters, **92**, 044105, 2008.

163. H. Dobb, K. Kalli, and D. J. Webb, "Measured sensitivity of arc-induced long-period grating sensors in photonic crystal fiber," Optics Communication, **260**, 184-191, 2006.

164. F. Tian, Z. He, and H. Du, "Numerical and experimental investigation of long-period gratings in photonic crystal fiber for refractive index sensing of gas media," Optics Letters, **37**, 380, 2012.

165. L. Rindorf. J. B. Jensen, M. Dufva, L. H. Pedersen, P. F. Hoiby, and O. Bang, "Photonic crystal fiber long-perod gratings for biochemical sensing," Optics Express, **14**, 8224, 2006.

166. M. Smietana, M. L. Korwin-Pawlowski, W. J. Bock, G. R. Pickrell, and J. Szmidt, "Refractive index sensing of fiber optic long-period grating structures coated with a plasma deposited diamond-like carbon thin film," Measurement Science and Technology, **19**, 085301, 2008.

167. H. J. Kim, O. J. Kwon, S. B. Lee, and Y. G. Han, "Polarization-dependent refractometer for discrimination of temperature and ambient refractive index," Optics Letters, **37**, 1802, 2012.

168. Q. Shi, B. Kuhlmey, and D. wu, "Refractive index sensor with acoustic grating in a low index contrast photonic bandgap fiber," Proc. of SPIE-OSA-IEEE Asia Communications and Photonics, SPIE **7630**, 763004, 2009.

169. J. Chen, D. Brabant, W. J. Bock, P. Mikulic and T. Eftimov, "Photonic crystal fiber refractive index sensor based on surface plasmon resonance," Proc. of SPIE, **7750**, 77502K-1, 2010.

170. A. Wang, A. Docherty, B. T. Kuhlmey, F. M. Cox, and M. C. Large, "Side hole fiber sensor based on surface plasmon resonance," Optics letters, **34**, 3890, 2009.

171. L. Ma, T. Katagiri and Y. Matsuura, "Surface-plasmon resonance sensor using silica-core Bragg fiber," Optics Letters, 34, 1069, 2009.

172. M. H. Frosz, A. Stefani, and O. Bang, "Highly sensitive and simple method for refractive index sensing of liquids in microstructured optical fibers using four-wave mixing," Optics Express, **19**, 10471, 2011.

173. J. L. Lim, D. J. J. Hu, P. P. Shum and Y. wang, "Cascaded photonic crystal fiber interferometers for refractive index sensing," IEEE Photonics Journal, **4**, 1163, 2012.

174. V. P. Minkovich, J. Villatoro, D. Monzon-Hernandez, S. Calixto, A. B. Sotsky, and L. I. Sotskaya, "Holy fiber tapers with resonance transmission for high-resolution refractive index sensing," Optics Express, **13**, 7609, 2005.

175. D. J. J. Hu, J. L. Lim, M. Jiang, Y. Wang, F. Luan, P. P. Shum, H. Wei, and W. Tong, "Long period grating cascaded to photonic crystal fiber modal interferometer for simultaneous measurement of temperature and refractive index," Optics Letters, **37**, 2283, 2012.

176. J. Villatoro, M. P. Kreuzer, R. Jha, V. P. Minkovich, V. Finazzi, G. Badenes, and V. Prunery, "Photonic crystal fiber interferometer for chemical vapour detection with high sensitivity," Optics Express, **17**, 1447, 2009.

177. W. Qian, C. C. Chan, C. Zhao, Y. Liu, T. Li, L. Hu, K. Ni, X. Dong, "Photonic crystal fiber refractive index sensor based on a fiber Bragg grating demodulation," Sensors and Actuators B, **166**, 761, 2012.

178. M. Deng, C-P. Tang, T. Zhu, Y-J. Rao, L-C. Xu, and M. Han, "Refractive index measurement using photonic crystal fiber based Fabry-Perot interferometer," Applied Optics, **49**, 1593, 2010.

179. Q. Li, and Q. Wang, "Refractive index sensor based on taperd PCF in-line interferometer," Chinese Optics Letters, **10**, 090601, 2012.

180. R. Jha, J. Villatoro, G. Badenes, and V. Pruneri, "Refractometry based on a photonic crystal fiber interferometer," Optics Letters, **34**, 617, 2009.

181. Y. Wang, D. N. Wang, C. R. Liao, T. Hu, J. Guo, and H. Wei, "Temperature-insensitive refractive index sensing by use of micro Fabry-Perot cavity based on simplified hollow-core photonic crystal fiber," Optics Letters, **38**, 209, 2013.

182. C. Li, S-J. Qiu, Y. Chen, F. Xu, and Y-Q Lu, "Ultra-sensitive refractive index sensor with slightly tapered photonic crystal fiber," IEEE Photonics Technology Letters, **24**, 1771, 2012.

183. R. Jha, J. Villatoro, and G. Badenes, "Ultrastable in reflection photonic crystal fiber modal interferometer for accurate refractive index sensing," Applied Physics Letters, **93**, 191106, 2008.

184. Y-J. Rao, M. Deng, D-W. Duan, and T. Zhu, "In-line fiber Fabry-Perot refractive-index tip sensor based on endlessly photonic crystal fiber," Sensors and Actuators A, **148**, 33-38, 2008.

185. J. M. Hollas, High Resolution Spectroscopy, 1st edition, Butterworths, London, 1982.

186. A. P. Thorne, Spetrophysics, Halsted Press (a Division of John Wiley & Sons, Inc), New York, 1974.

187. D. H. Martin, Spectroscopic Techniques, John Wiley & Sons, Inc, New York, 1967.

188. N. Sheppard, "The historical development of experimental techniques in vibrational spectroscopy," in Handbook of Vibrational Spectroscopy, Edited by J. M. Chalmers, Vol. **1**, John Wiley & Sons, 2002.

189. R. J. Bell, Introductory Fourier Transform Spectroscopy, Academic, pp 56–60, 1972.

190. V. Saptari, Fourier-transform spectroscopy instrumentation engineering, SPIE Press, Bellingham, WA, 2003.

191. S. Wielandy, and S. C. Dunn, "Tilted superstructure fiber grating used as a Fourier-transform spectrometer," Optics Letters, **29**, 1614, 2004.

192. Y. Wang, M. Han, and A. Wang, "High-speed fiber-optic spectrometer for signal demodulation of interferometric fiber-optic sensors," Optics Letters, **31**, 2408, 2006.

193. Y. Wang, M. Han, and A. Wang, "Analysis of a high-speed fiber-optic spectrometer for fiber-optic sensor signal proceesing," Applied Optics, **46**, 8149, 2007.

194. H. Imani, S. Golmohammadi, A. Rostami, and K. Abbasian, "Resolution improvement in high-speed fiber-optic spectrometers using photonic crystal fibers," in Proceedings of International Conference on Photonics, Langkawi, Kedah, ICP2010-35, 2010.

195. R. D. Meade, A. M. Rappe, K. D. Brommer, and J. D. Joannopoulos, "Accurate theoretical analysis of photonic band-gap materials," Physics Review B, **48**, 8434, 1993.

196. C. Charlton, B. Temelkuran, G. Dellemann, and B. Mizaikoff, "Mid-infrared sensors meet nanotechnology: trace gas sensing with quantum cascade lasers inside photonic band-gap hollow waveguides", Applied Physics Letters, **86** 194102, 2005.

197. S.G. Johnson, M. Ibanescu, M. Skorobogatiy, O. Weiseberg, T.D. Engeness, M. Soljacic, S.A. Jacobs, J.D. Joannopoulos, and Y. Fink, "Low-loss asymptotically singemode propagation in large core omniguide fibers," Optics Express, **9**, 748, 2001

198. W.M. Haynes, CRC Handbook of Chemistry and Physics, 91st ed., CRC Press, Boca Raton, FL, pp. 8–71, 2010.

199. J. M. Sullivan, M. S. Twardowski, J. R. V. Zaneveld, C. M. Moore, A. H. Barnard, P. L. Donaghay, and B. Rhoades, "Hyperspectral temperature and salt dependence of absorption by water and heavy water in the 400–750 nm spectral range," Applied Optics, **45** , 2006.

200. A. Dupuis, N. Guo, B. Gauvreau, A. Hassani, E. Pone, F. Boismenu, and M. Skorobogatiy, "Guiding in the visible with 'colorful' solid-core Bragg fibers," Optics Letters, **32**, 2882, 2007.

201. B. Gauvreau, N. Guo, K. Schicker, K. Stoeffler, F. Boismenu, A. Ajji, R. Wingfield, C. Dubois, and M. Skorobogatiy, "Color-changing and color-tunable photonic bandgap fiber textiles," Optics Expres, **16**, 15677, 2008.

202. M. Skorobogatiy, "Efficient anti-guiding of TE and TM polarizations in low index core waveguides without the need of omnidirectional reflector," Optics Letters, **30**, 2991, 2005.

203. Y. Gao, N. Guo, B. Gauvreau, M. Rajabian, O. Skorobogata, E. Pone, O. Zabeida, L. Martinu, C. Dubois, and M. Skorobogatiy, "Consecutive solvent evaporation and co-rolling technique for polymer multilayer hollow fiber preform fabrication," Journal of Material Research, **21**, 2246–2254, 2006.

204. D. Passaro, M. Foroni, F. Poli, A. Cucinotta, S. Selleri, J. Laegsgaard, and A. O. Bjarklev, "All-silica hollow-core microstructured Bragg fibers for biosensor application," IEEE Sensors Journal, **8**, 1280, 2008.

205. Y. Nazirizadeh, U. Bog, S. Sekula, T. Mappes, U. Lemmer, and M. Gerken, "Low-cost label-free biosensors using photonic crystals embedded between crossed polarizers," Optics Express, **18**, 19120, 2010.

206. T. Liu, X. Chen ,Z. Di, J. Zhang, X. Li, and J. Chen, "Measurement of the magnetic field-dependent refractive index of magnetic fluids in bulk," Chinese Optics Letters, **6**, 195, 2008.

207. Y. Zhao, R. Lv, Y. Ying, and Q. Wang, "Hollow-core photonic crystal fiber Fabry-Perot sensor for magnetic field measurement based on magnetic fluid," Optics & Laser Technology **44**, 899-902, 2012.

208. http://www.oceanoptics.com/Products/maya.asp

209. H. Qu, T. Brastaviceanu, F. Bergeron, J. Olesik, I. Pavlov, and M. Skorobogatiy, "Photonic bandgap Bragg fiber sensors for bending/displacement detection," Applied Optics, **52**, 6344-6349, 2013.

210. A. G. Mignani, P. B. Garcia-Allende, L. Ciaccheri, O. M. Conde, A. Cimato, C. Attilio, D. Tuna, "Comparative analysis of quality parameters of Italian extra virgin olive oils according to their region of origin," Proc. of SPIE, **7003**, 700326, 2008.

211. J. R. Janesick, Scientific Charge-Coupled Devices, SPIE Press, Bellingham, WA, 2001.

212. Y. P. Hong, and C-T Pan, "Rank-revealing QR factorizations and the Singular Value Decomposition," Mathematics of Computation, **58**, , 213-232, 1992.

213. http://www.basiccolor.de/x-rite-io-scanning-table/

214. http://www.automation.com/library/articles-white-papers/vision-sensors-systems/packagers-choose-machine-vision-quality-inspection-to-reduce-waste-and-boost-roi

APPENDIX: LIST OF PUBLICATIONS

Below is the full list of contributed publications and conference proceedings produced during the course of this doctoral thesis.

Peer-reviewed journal articles

1. **H. Qu**, T. Brastaviceanu, F. Bergeron, J. Olesik, I. Pavlov, and M. Skorobogatiy, "Photonic bandgap Bragg fiber sensors for bending/displacement detection," Applied Optics, Vol. 52, pp. 6344-6349, (2013)

2. **H. Qu**, and M. Skorobogatiy, "Resonant bio- and chemical sensors using low-refractive-index- contrast liquid-core Bragg fibers," Sensors and Actuators B: Chemical, Vol. 161, pp. 261-268, (2012)

3. **H. Qu**, B. Ung, M. Roze and M. Skorobogatiy, "All photonic bandgap fiber spectroscopic system for detection of refractive index changes in aqueous analytes," Sensors and Actuators B: Chemical, Vol. 161, pp. 235-243 (2012)

4. **H. Qu**, and M. Skorobogatiy, "Liquid-core low-refractive-index-contrast Bragg fiber sensor," Applied Physics Letters, Vol. 98, pp. 201114 (2011)

5. **H. Qu**, B. Ung, I. Syed, N. Guo and M. Skorobogatiy, "Photonic bandgap fiber bundle spectrometer," Applied Optics, Vol. 49, pp. 4791-4799 (2010)

6. **H. Qu,** G. F. Yan, and M. Skorobogatiy, "Interferometric fiber-optic bending/nano-displacement sensor using plastic dual-core fiber," to be submitted.

Conference Proceedings:

1. **H. Qu**, T. Brastaviceanu, F. Bergeron, I. Pavlov, J. Olesik, and M. Skorobogatiiy, "Micro-displacement sensors based on plastic photonic bandgap Bragg fibers," IEEE Photonics Conferences, Washington, (2013).

2. A. Markov, S. Gorgutsa, **H. Qu,** and M. Skorobogatiy, "Plasmonic Two Wire Terahertz Fibers with Highly Porous Dielectric Support," Conference on lasers and Electro Optics (CLEO), CTh1K.4, San Jose, USA, (2013).

3. **H. Qu**, T. Brastaviceanu, F. Bergeron, I. Pavlov, J. Olesik, and M. Skorobogatiiy, "Micro-displacement sensors based on plastic photonic bandgap Bragg fibers," Optical Sensors Topical Meeting, SM2D.5, Rio Grande, Puerto Rico, (2013).

4. **H. Qu**, J-P Bourgeois, J. Rolland, A. Vlad, J-F Gohy and M. Skorobogatiy, "Flexible fiber batteries for applications in smart textiles," 2012 Materials Research Society Fall Meeting, Section A: complient Energy Sources, Talk A4.01, Boston, USA, (2012).

5. **H. Qu**, and M. Skorobogatiy, "Liquid-core low-refractive-index-contrast Bragg fiber sensor," (BIO-SENS-6-20-3), Photonic North, Montreal, Canada, (2012).

6. **H. Qu**, and M. Skorobogatiy, "All-photonic-bandgap-fiber sensor for detection of liquid refractive index," (BIO-SENS-8-50-5,) Photonic North, Montreal, Canada, (2012).

7. **H. Qu**, B. Ung, and M. Skorobogatiy, "Photonic bandgap fiber bundle spectrometer," CM4B. 4, CLEO, San Jose, CA, USA, (2012).

8. **H. Qu**, and M. Skorobogatiy, "All-polymer photonic bandgap Bragg fibers for bio-chemical sensors and spectrometers," K-1, 17th Micro-optics Conference (MOC'11), Sendai, Japan, (2011).

9. **H. Qu**, B. Ung, and M. Skorobogatiy, "Liquid-filled hollow core photonic bangap fiber sensor," Optical Sensors, OSA Technical Digest (CD), Toronto, Canada, paper SWB6, (2011).

10. **H. Qu**, B. Ung, F. Boismumu, N. Guo, and M. Skorobogatiy, "Photonic bangap fiber bundle spectrometer," Optical Sensors, Germany, SThB5, (2010).